UNIVERSIDAD DE CHILE
FACULTAD DE CIENCIAS FÍSICAS Y MATEMÁTICAS
ESCUELA DE POSTGRADO Y EDUCACIÓN CONTINUA

JETS DE GAS SIMPLES Y GEMELOS, SUBEXPANDIDOS Y SUMERGIDOS EN LÍQUIDO, UTILIZANDO SIMULACIONES CFD URANS

TESIS PARA OPTAR AL GRADO DE DOCTOR EN
CIENCIAS DE LA INGENIERÍA MENCIÓN FLUIDODINÁMICA

MÁXIMO CRISTÓBAL LEÓN GANEM

PROFESOR GUÍA:
ALVARO VALENCIA MUSALEM

MIEMBROS DE LA COMISIÓN:
RODRIGO HERNANDEZ PELLICER
GONZALO MONTES ATENAS
MARCO ROSALES VERA
ROBERTO PARRA FIGUEROA

SANTIAGO DE CHILE
2022

RESUMEN DE LA TESIS PARA OPTAR
AL GRADO DE: DOCTOR EN CIENCIAS
DE LA INGENIERÍA MENCION FLUIDODINÁMICA
POR: MÁXIMO CRISTÓBAL LEÓN GANEM
FECHA: 2022
PROF. GUÍA: ALVARO VALENCIA MUSALEM

JETS DE GAS SIMPLES Y GEMELOS, SUBEXPANDIDOS Y SUMERGIDOS EN LÍQUIDO, UTILIZANDO SIMULACIONES CFD URANS

La inyección sumergida es un proceso donde un flujo de gas penetra un medio líquido, generando distintos patrones, dependiendo de las características tales como tipo de gas (aire, vapor), velocidad, presión y temperatura. Este proceso se ha estudiado durante unos 50 años mediante trabajos teóricos, experimentos y simulaciones numéricas. Las aplicaciones típicas se encuentran en diferentes sectores industriales: procesos metalúrgicos, centrales nucleares y propulsión de vehículos.

La bibliografía revisada sobre inyección sumergida está relacionada principalmente con el tipo simple, abarcando los regímenes de burbujeo hasta jet. Los jets gemelos subexpandidos se han estudiado principalmente para flujos monofásicos compresibles (e.g., aire-aire), donde se presta especial atención a la generación de sonido de estos. A pesar de todos los avances en la investigación sobre inyección sumergida, hasta la fecha de este documento, el autor no ha encontrado análisis, experimentales o numéricos, centrados en la inyección sumergida de jets gemelos. Por esto, es de gran interés y motivación contribuir a los estudios de jets degas inyectados en líquidos, con el objetivo principal de entregar el análisis de las interacciones y características de jets gemelos sumergidos y subexpandidos.

Esta tesis aborda el análisis y las características de los jets de aire sumergidos y subexpandidos inyectados en agua por medio de toberas (tubos rectos) simples y gemelas. Primero, se compara la simulación de Dinámica de Fluidos Computacional (CFD) de una tobera simple con los datos experimentales disponibles en la literatura. Al utilizar toberas gemelas, se varía el espaciado y se compara el flujo resultante con el obtenido con la configuración de una sola tobera, bajo condiciones experimentales similares. Cuando dos toberas gemelas están cera, y en comparación con una sola tobera que inyecta el mismo flujo másico, se encuentra un aumento en la longitud del núcleo de cada chorro, generando uno combinado, y con un aumento en los niveles de mezcla. Con una mayor separación de toberas, se encuentran núcleos individuales de menor extensión y un incremento significativo de niveles de mezcla. Con esta información, se presenta una guía general de selección de toberas para ayudar al diseño de procesos de inyección de gas en un líquido.

Para Estefanía y
Mariagracia.

Acknowledgments

This research began with a single question: "*is it possible to redesign submerged injection reactors, making use of tuyere modifications to obtain a smoother and longer operational times?*".

Several people in the engineering and mining industry were involved in the development of a large applied research project that gave birth to this thesis. Their names and background are now hidden, because of specific parts of the contract that prohibits distribution of information. However, this study and the acquired knowledge is still being used to aid other mining operations.

This research thesis work was brought as an original work, and until now, no other authors have covered it. Thanks to Prof. Alvaro Valencia, the project was carried out and, after a long publication process, our article saw the light on september 2021. Also, it is important to mention that this research was partially supported by the supercomputing infrastructure of the NLHPC (ECM-02).

All the knowledge and my path in science is now in the applied research and engineering, where I am happy to contribute with not only this small piece of work, but with other capabilities gained during the process of (self-) education that only the challenging PhD path can provide.

This path has ended. Now, I can finally rest, at least for a while, after 13 years of the best possible higher education in fluid dynamics I found in Chile (Universidad de Chile) and The Netherlands (Technische Universiteit Delft).

To all those colleagues in the engineering & research companies, universities, and mining industry I worked with, those departed in the past 4 to 5 years, and the new people recently involved, I say to you:

Thank you.

Table of Content

Index of Tables

Index of Figures

Nomenclature

d: Tuyere diameter, m.

e: Tuyere thickness, m.

D: Tank Diameter, m.

l: tuyere length, m.

A: Tuyere area, m^2.

L: General length scale, m.

H: Tank/Water level Height, m.

t: Time, m/s.

s: Tuyere interspace, m.

f: friction factor, -.

x: x coordinate, m.

y: y coordinate, m.

z: z coordinate, m.

r_∞: Jet boundary radius at a given axial distance, m.

c: Sound Speed, m/s.

p: Pressure, Pa.

T: Temperature, K.

u,v: Velocity components, m/s.

w: jet width, m.

U: Velocity vector, m/s.

a_b: Interface acceleration, m/s^2.

c_p: specific heat, J/kgK.

R: individual gas constant, J/kgK.

G: mass flow flux, kg/m^2s.

m, mass flow, kg/s.

M, jet momentum kgm/s.

V, jet volume, m^3.

L_p, potential core length, m.

F_{ent}: Normalized entrainment rate, -.

K, Kinetic (mechanical) energy, m^2/s^2.

k, Turbulent kinetic energy m^2/s^2.

Ma: Mach Number, -.

Fr: Froude Number, -.

ρ: Density, kg/m^3.

γ: specific heat ratio, -.

σ, Surface tension, $N \cdot m$.

η: Underexpansion level

α: volume fraction.

θ, jet opening angle at injection, rad.

β, jet boundary opening angle, rad.

ψ, compressibility factor, -.

ω, Specific energy dissipation, m^2/s^3.

ν, Kinematic viscosity, m^2/s.

μ, Dynamic viscosity, kg/ms.

λ, instability criteria limit, -.

τ, Shear stress, Pa.

Chapter 1

Introduction and Objectives

1.1. Introduction

Submerged injection is a process in which gas flow penetrates a liquid bath, generating different patterns, depending on injection characteristics, such as gas type (e.g. air, steam), velocity, pressure and temperature. This process has been studied for about 50 years through experiments (Aoki [3], Brimacombe et al. [8], Davidson & Amick [14], Davidson & Schuler [15], Harby et al. [26], Iguchi et al. [27], Themelis et al. [54], Weiland & Vlachos [57]), theoretical work (Chawla [13], Epstein et al. [19], Rosales et al. [48]) and numerical simulations (Gong et al. [24], Tang et al. [52]). Typical applications are found in different industrial sectors: metallurgical (Bustos et al. [9]), nuclear power plants (Gulawani [25], Suponitsky et al. [51]) and vehicle propulsion (Moon et al. [35], Tang et al. [52]).

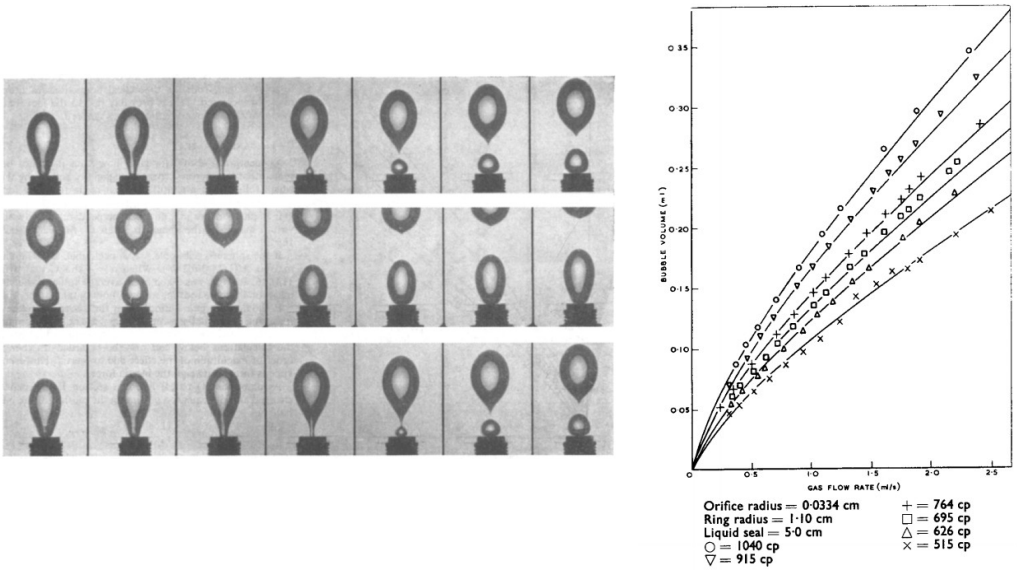

Figure 1.1: Bubble flow from Davidson & Schuler [15]. In addition, the bubble diameter is measured and plotted as a function of the gas flow rate and different liquid viscosities.

Early experiments by Davidson & Amick [14] and Davidson & Schuler [15] were dedicated to bubble dynamics injected in liquids (water and mercury), analyzing frequency and diameter as a function of flow rate (see Figure 1.1), where the main mechanism that drives the bubble motion is buoyancy and viscosity effects. As the injection flow increases, the relevant mechanism continues to be buoyancy. However, a preferential growth in the main velocity direction appears, giving rise to an ellipsoid-like bubble. The bubble initially becomes more ellipsoidal with increasing flow, as shown in Figure 1.2 . Once the bubble center is displaced by a magnitude approximately equal to the diameter of the injector, the bubble then detaches.

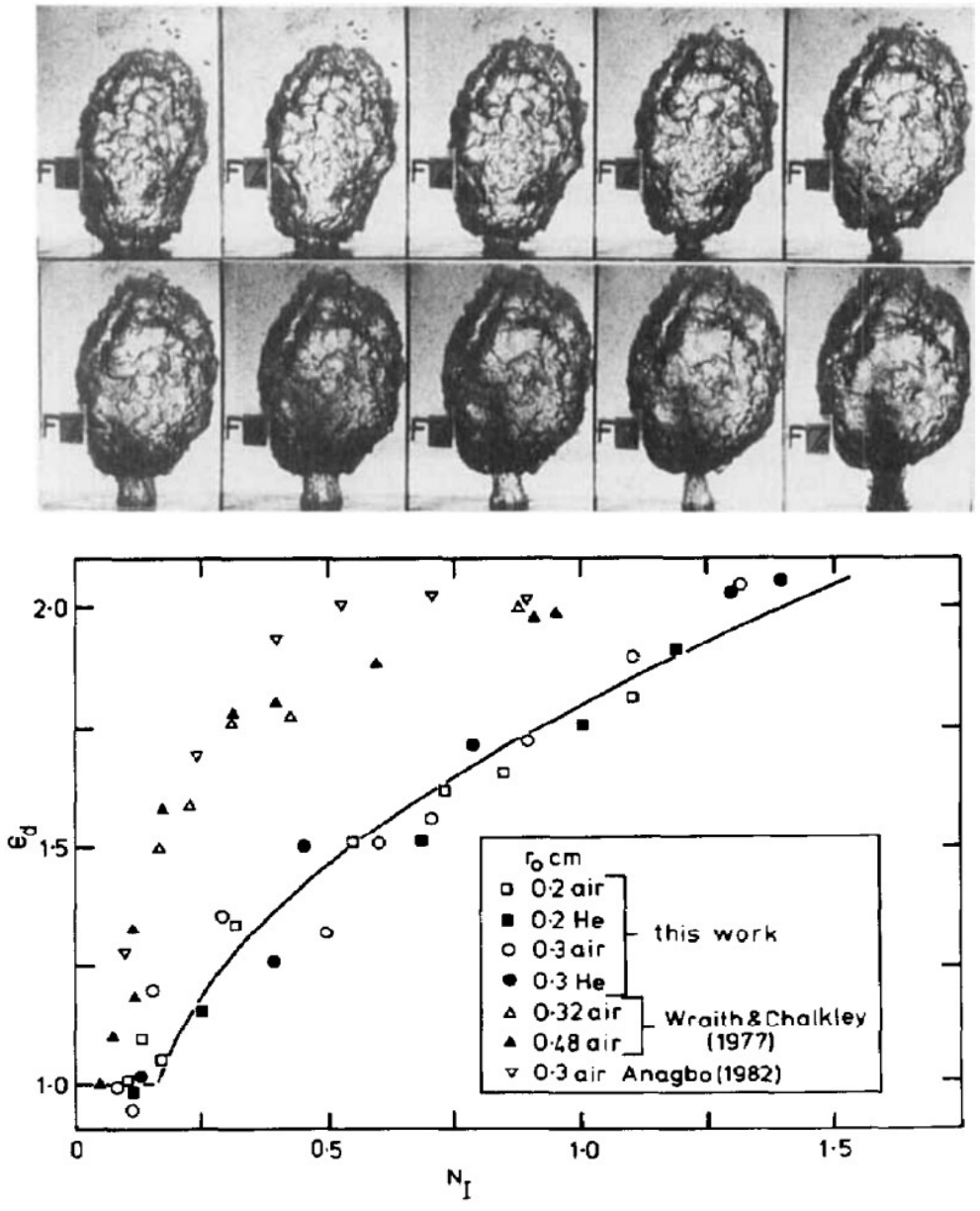

Figure 1.2: Elongated bubbling flow, where its eccentricity is plotted as a function of increasing normalized flow, N_I.

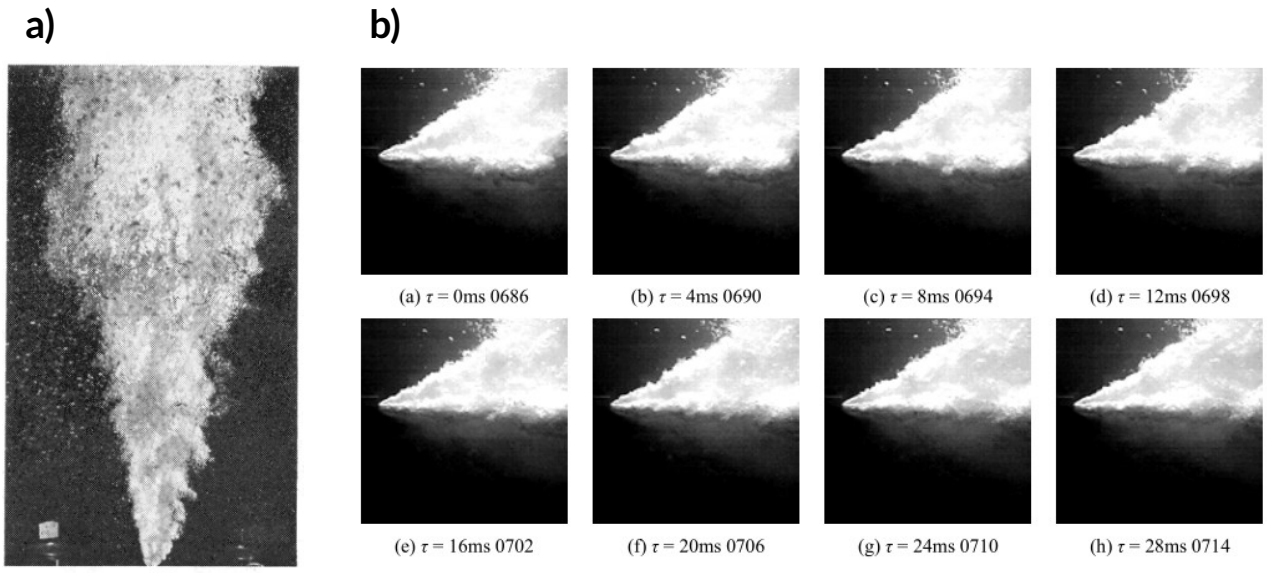

Figure 1.3: a) Jet flow from Mori et al. [36]. b) Jet flow from Miaosheng et al. [34].

The following four decades after, experimental studies related to copper and steel industries helped to define injection regimes (Brimacombe et al. [8], Bustos et al. [9], Mori et al. [36], Ozawa & Mori [40]). Mori et al. [36] and Ozawa & Mori [40] identify three main types: 1) bubbling, 2) transition and 3) jet. In the latter, submerged gas flow has a sonic velocity at the tuyere or nozzle exit, generating a continuous injection, characterized by a bubble curtain, as shown in Figure 1.3 . Under these conditions, the presence of a (hypothesized) single shock cell, classically determined by the intersection of oblique shocks (Donaldson & Snedeker [17]), defined by a Mach disk and barrel shock, was identified as an important flow feature (see 1.4). This structure was obtained in the experiments by Aoki [3] and Loth & Faeth [32], where pressure probes were used to identify a sinusoidal pattern in the axial direction, a behavior typically found in the extensively studied single-phase (air-to-air) underexpanded jets (Franquet et al. [22]).

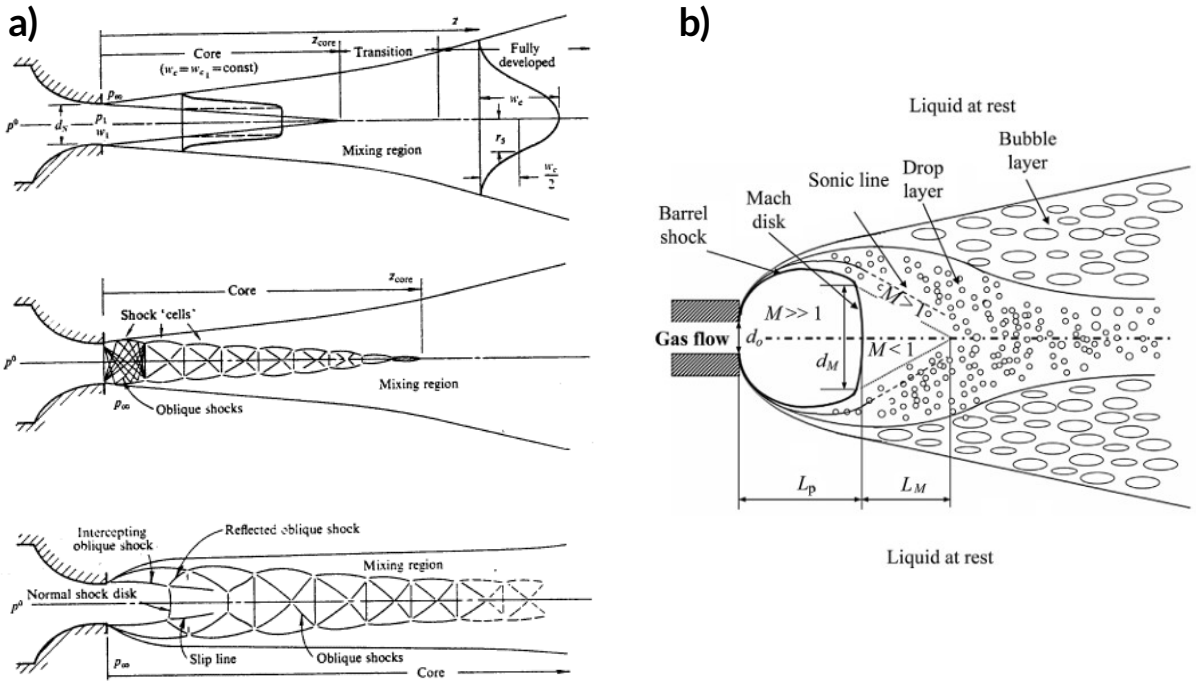

Figure 1.4: a) Shock cells in underexpanded jet flow from Donaldson & Snedeker [17]. b) Shock cell in submerged single underexpanded jet from Roger et al. [46].

During jet injection, several events are observed which vary in occurrence and intensity, depending on injection pressure, and are related to air-water interface deformations (Tang et al. [52]), as depicted in Figure 1.5: a) Expansion or Bulging, b) Necking, c) Breaking or Pinch-off and d) a wall-knocking effect, denominated back-attack by Aoki [3], but that is still a debatable definition (see Miaosheng et al. [34] and references therein). Interface interactions a) to c) are predominantly related to the growth of Kelvin-Helmholtz (KH) instabilities (Chawla [13], Epstein et al. [19]) that develop, depending on the gas-liquid density and viscosity ratios, and tuyere exit pressure. The back-attack effect was observed by Ozawa & Mori [41], where exit pressure, during a necking event, increased for larger exit velocities, ranging from sub- to super-sonic, and that the "wall-knocking" frequency dropped for increasing gas flow rate. Later, it was reported by Gulawani [25] and Miaosheng et al. [34] that to avoid back-attack, the tuyere exit-to-ambient pressure ratio, η_e, should be such that $\eta_e \approx 2$.

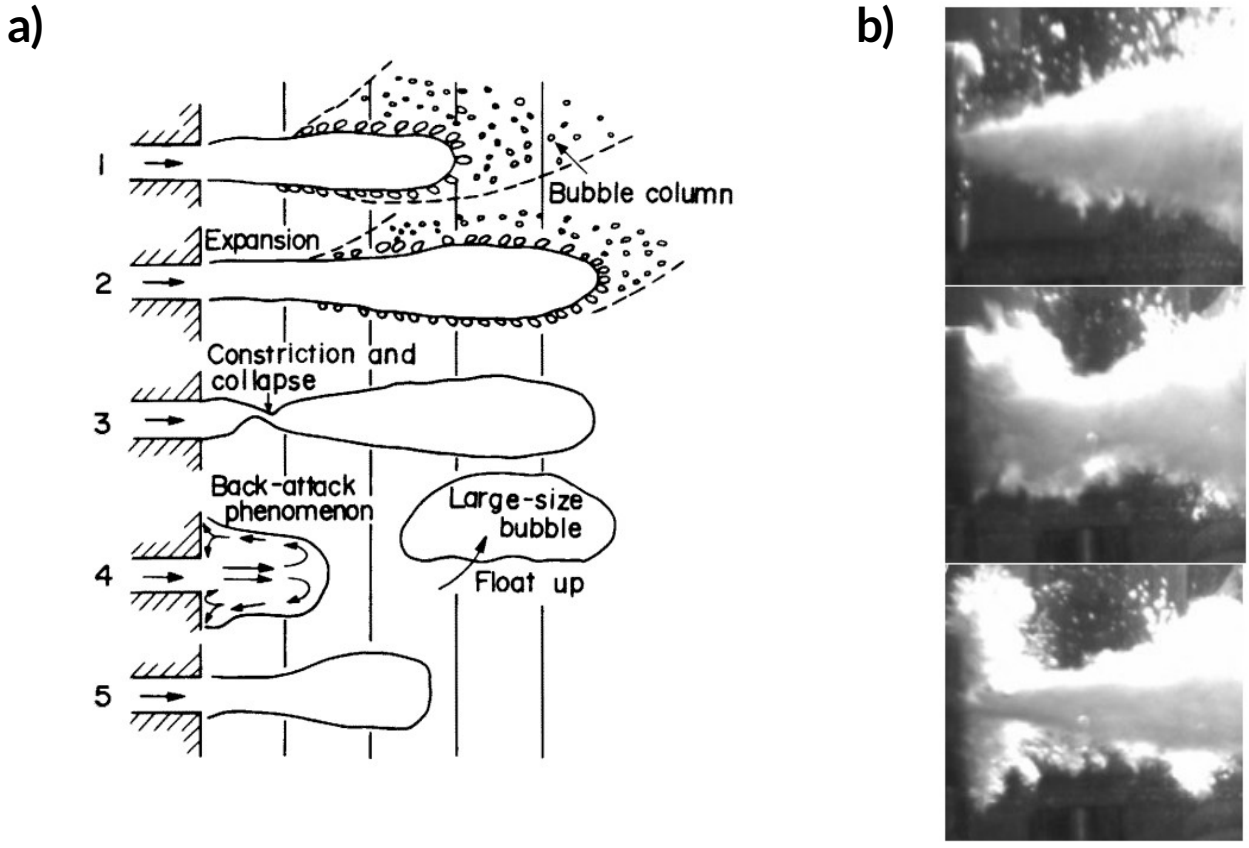

Figure 1.5: Events of Expansion or Bulging, Necking, Breaking or Pinch-off and back-attack: a) Schematic from Aoki [3], b) Back-attack from [52].

Twin injection has been largely studied for underexpanded supersonic air jets. In this arrangement, two identical tuyeres or nozzles are placed in such way that different modes of interactions are observed between jets. In the experiments of Raman & Taghavi [44] and Knast et al. [29] it is shown that these modes correspond in general to flapping (asymmetric) and waving (symmetric). Through sound spectra and pressure distributions analysis, it is argued that complex mechanisms involved in modes selection are related to sound-generated feedback between jets, an interaction that can be modified through interspace separation and jet injection characteristics. In contrast, interaction between submerged jets is no longer due to sound (since there is a large phase density ratio) but to other mechanisms, related to the gas-liquid interface dynamics (Shi et al. [49]), i.e. where there is a difference between the high speed gas jet and the liquid velocity, leading to interface deformation. Structure of turbulent (subsonic) and supersonic twin jets has been studied and observed by Carasik et al. [10], Essel et al. [20] and Bell et al. [5], where merging, converging and combined regions are defined and analyzed. These zones are useful to differentiate between single and twin jets, since only in the latter configuration it is possible to define them. In addition, the experiments by Oskouie et al. [39] show interaction of twin jets when their separation is increased, finding that velocity

fluctuations have an abrupt increase near the merging points, along the symmetry line, and that a peak in fluctuations is obtained as nozzles are further separated, as shown in Figure 1.6

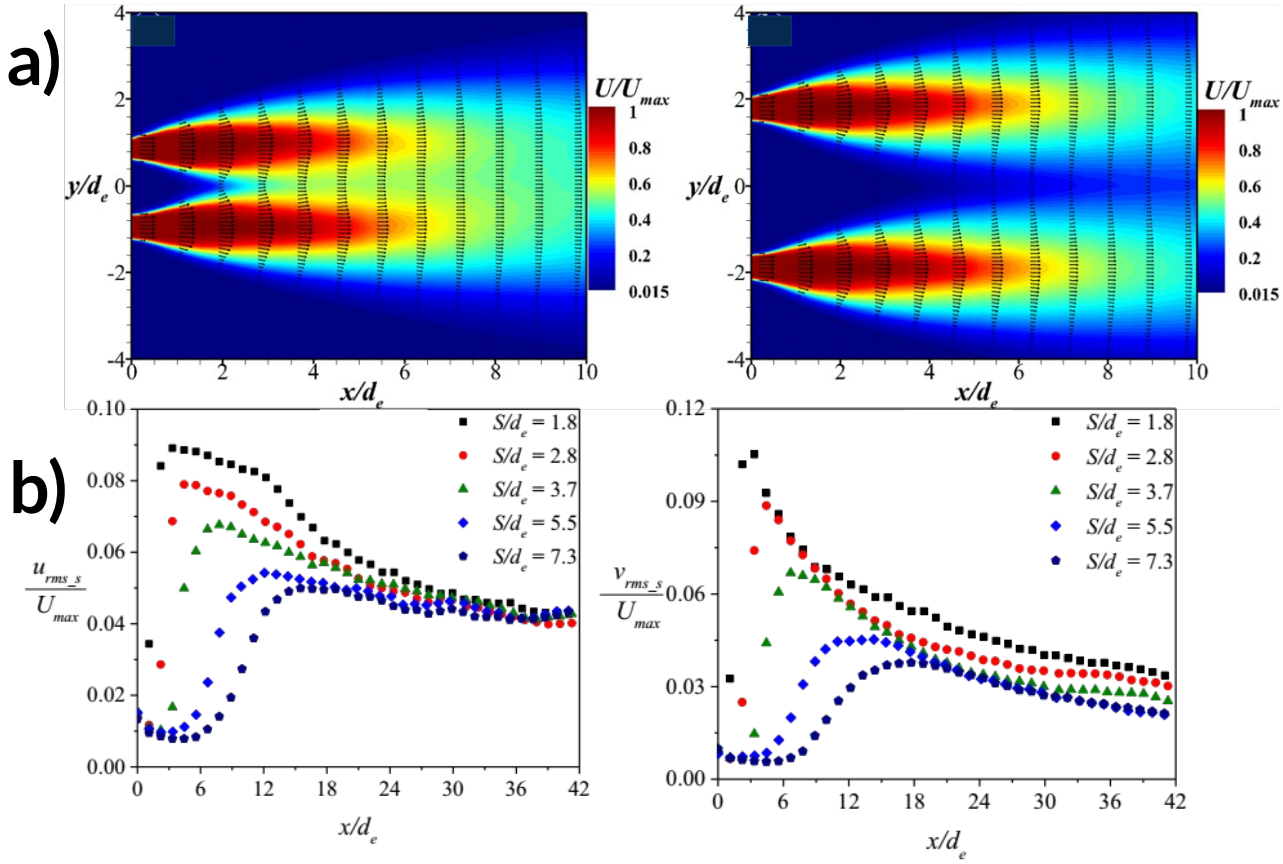

Figure 1.6: Results from the work by Oskouie et al. [39]: a) Mean flow b) streamwise and spanwise velocity rms along the symmetry line of the twin jets.

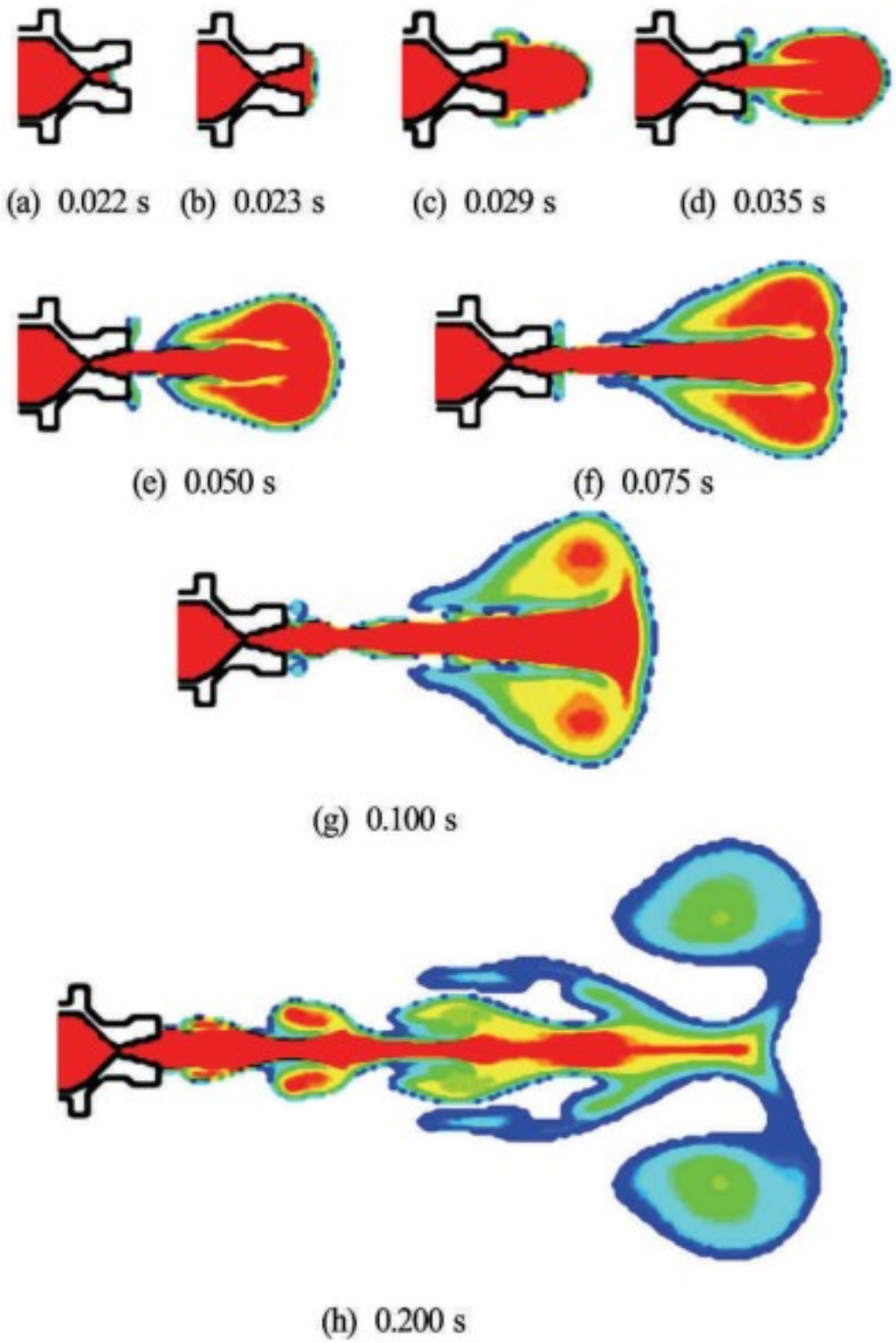

Figure 1.7: CFD simulation results of a single underexpanded nozzle by Gong et al. [24].

Submerged jets have also been studied through 2D and 3D CFD simulations, focusing in a single nozzle arrangement. Examples of such works are the 2D axi-symmetric simulations and experimental validations by Tang et al. [52] and Gong et al. [24]. On one hand, Tang et al. [52] show large instabilities that lead to back-attack events, along with strong pressure and velocity variations. In addition, Gong et al. [24] analyze the thrust generated by a Laval nozzle (see Figure 1.7), revealing that underwater jet injection offers great variation in thrust that decreases with depth of injection. On the other hand, the 3D simulation of a single nozzle by Fronzeo & Kinzel [23] demonstrate great changes in overall flow characteristics when the secondary phase density is increased.

All of the reviewed experimental and numerical works on submerged injection are related to the single jet, covering the bubbling to jet regimes. Underexpanded twin jet has been studied only for compressible single phase (e.g. air-to-air) flows, where particular attention is made to sound generation of such jets. In spite of all the advances in research on submerged injection, to the date of this article, the authors have not found analysis, either experimental or numerical, focused on submerged twin jet injection. Thus, it is of great interest and motivation to make a contribution to the studies of gas jets injected into liquids, with the primary objective of delivering the analysis of submerged and underexpanded twin gas jet interactions and characteristics.

1.2. Study Objectives

The study objectives of the present work are:

- Evaluate available experimental data for a single submerged jet injection
- Compare unsteady CFD simulation results with experimental data, considering the zone far from a free surface.
- Characterize the flow field and typical structure of underwater single and twin jets in terms of velocity and volume fraction distributions.
- Analyze the interaction between twin jets when tuyere's spacing is varied, with operating conditions equal to that of a single jet.
- Propose a general guideline to choose between any configuration, based on characteristics such as back-attack, mixing or entrainment, and length of inertial range

To achieve these objectives, Computational Fluid Dynamics (CFD) simulations will be used. In particular, the open source software OpenFOAM [38] which provides a series of modules that are brought together to analyze submerged underexpanded jets.

1.3. Hypothesis

The hypothesis in the present work is summarized in the following list

- It is expected that two jets will interact, producing different cell structures, modifying the typical single phase (air) jet structure and the mixing properties of the submerged jets.
- The interaction between two identical submerged jets is produced by means of their interface deformation, along with both pressure and velocity fluctuations. It is expected that sound generation will not have an effect in the resulting flow, as mentioned by Loth & Faeth [32] where the Richardson number, Ri, is about 10^{-4}.

Chapter 2

Review of Submerged Jet Description

2.1. Basic Mathematical Description

2.1.1. Overview of Ideal, Over and Underexpanded Jets

As a start, a converging nozzle is considered to gain insight in how the mass flow, related to velocity and pressure vary for different operating conditions. For isentropic flow (i.e. where pressure, p, and density, ρ, are such that p/ρ^{γ} is constant), the mass flow flux of a converging and diverging (CD) nozzle is given, in terms of the exit velocity, by equation 2.1.

$$G = \frac{m}{A} = p_{t,1}\sqrt{\frac{\gamma}{RT_{t,1}}}Ma_2\left[1+\frac{\gamma-1}{2}Ma_2^2\right]^{\frac{-(\gamma+1)}{2(\gamma-1)}} \tag{2.1}$$

where G is the mass flow flux in $kg/(m^2s)$, Ma_2 is the exit Mach number, $p_{t,1}$ is the total inlet pressure, and $T_{t,1}$ is the inlet total temperature. Using the relation for stagnation pressure in equation 2.2.

$$\frac{p_{t,1}}{p_{t,2}} = \left[1+\frac{\gamma-1}{2}Ma_2^2\right]^{-\gamma/(\gamma-1)} \tag{2.2}$$

Then, equation 2.1 can be replaced by equation 2.3.

$$G = p_{t,1}\sqrt{\frac{\gamma}{RT_{t,1}}}\left[\frac{2}{\gamma-1}\left(p_r^{(\gamma-1)/\gamma}-1\right)p_r^{-(\gamma+1)/\gamma}\right]^{1/2} \tag{2.3}$$

where $p_r = \frac{p_{t,1}}{p_{t,2}}$. With this relation, it is possible to analyze the behavior of mass flow and pressure under choking conditions for air (with R=286.9 J/kgK), i.e. when

Ma_2=1 for a critical pressure of $p_{r,c}$=1.893 or $p_{r,c}^{-1}$= 0.5283. Figure 2.1 shows the mass flow and exit pressure as a function of $1/p_{r,c}$. From this plot it is observed that for 0.5283< $1/p_r$ <1 the flow is subsonic and exit pressure corresponds to the ambient pressure. For $1/p_r = 0.5283$, the flow is sonic and the critical mass flow flux, G_c, becomes constant and is expressed by equation 2.4.

$$G_c = p_{t,1}\sqrt{\frac{\gamma}{RT_{t,1}}}\left[\frac{\gamma+1}{2}\right]^{\frac{-(\gamma+1)}{2(\gamma-1)}} \tag{2.4}$$

It can be noticed that mass flow depends now only on the total inlet conditions, and more specifically, for an approximately constant inlet total temperature, mass flow can be increased linearly with the inlet pressure.

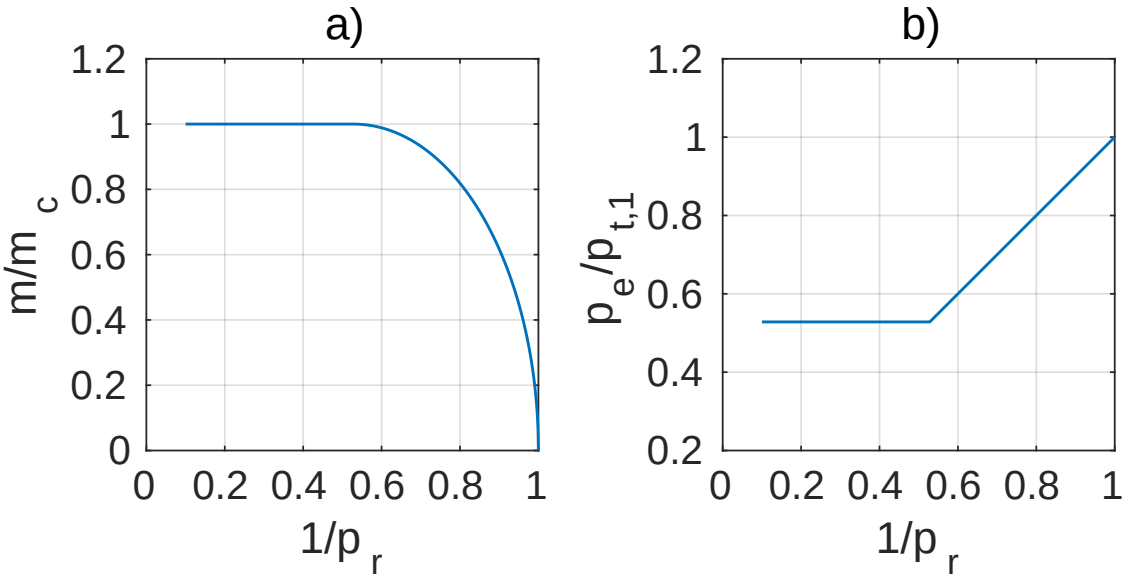

Figure 2.1: Flow conditions of a convergent nozzle as a function of the p_r: a) mass flow flux, b) pressure. Here, m_c is the critical mass flow rate at choking conditions, where for air, $1/p_{r,c}$=0.5283.

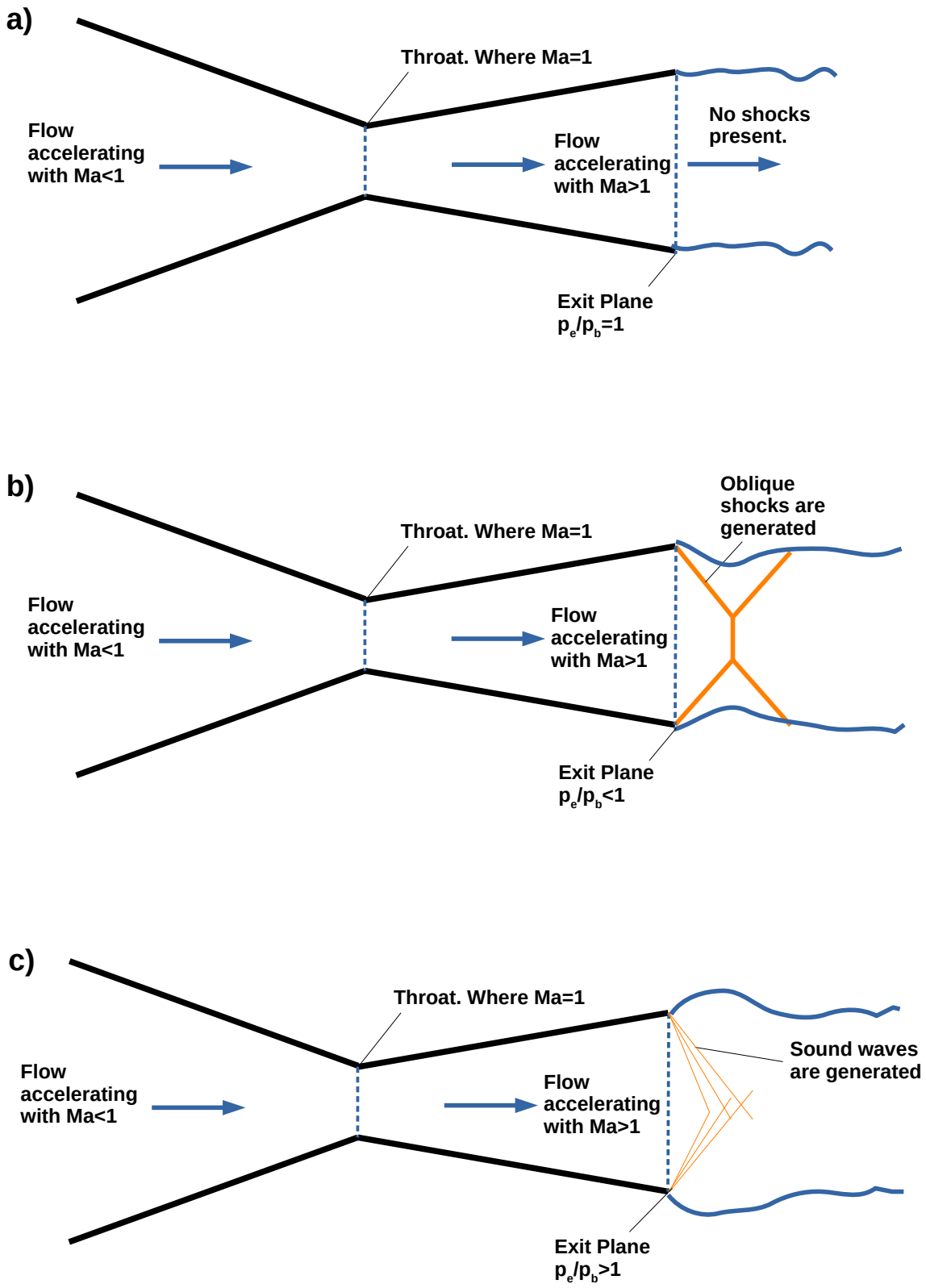

Figure 2.2: Sketch of ideal, over and under expanded flow through a converging and diverging nozzle.

For converging and diverging (CD) nozzles, a similar plot can be obtained, but now sonic conditions is achieved at the throat, and in the diverging part several flow features, depicted in Figure 2.2. Depending in the exit pressure, for Ma=1 at the throat, the following is observed, depending on the exit flow exit pressure, p_e:

- When p_e/p_b=1 (Figure 2.2 a)), the flow is ideally expanded. This means the supersonic flow expands and pressure drop is such that at the nozzle exit the flow pressure is equal to the ambient pressure.
- When p_e/p_b <1 (Figure 2.2 b)), an over-expanded flow is obtained. This means that the (supersonic) velocity is such that the ambient pressure is reached inside the nozzle. This usually means that shocks are present outside the nozzle, producing sub and supersonic speed regions. If velocity is further increased, shocks may appear inside the nozzle's diverging section.
- When p_e/p_b >1 (Figure 2.2 c)), underexpanded flow is obtained. Here, the supersonic velocity reached inside the nozzle still does not reach the ambient pressure. The remaining expansion occurs outside the nozzle. An expansion fan is centered at the nozzle lip, generating shock waves as reflected compression waves interact. Such interaction generates zones of super and sub sonic flow. The process continues until sonic flow is obtained and jet pressure is restored to the ambient pressure.

While the study of a CD nozzle covers the general flow features that can be present in sonic and supersonic flows, it is important to notice that the underexpanded condition can be obtained with converging and straight nozzles (or tuyeres) while over-expansion is not possible to attain.

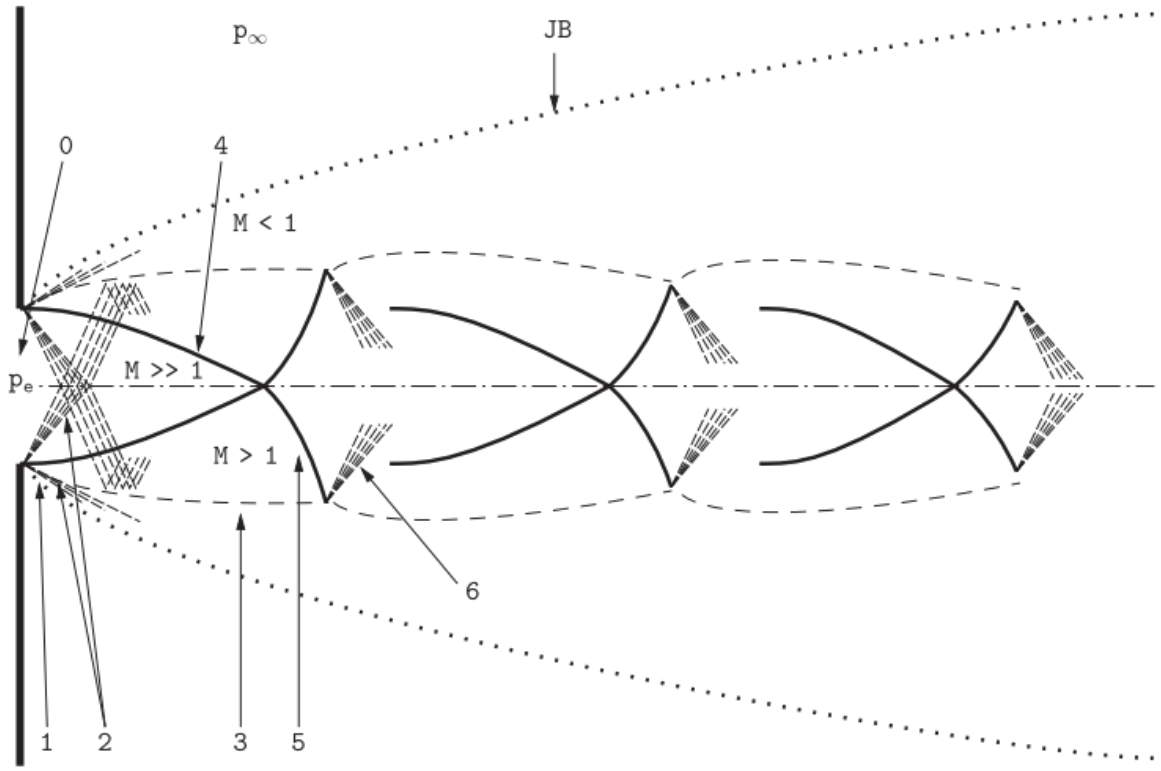

Figure 2.3: Sketch of a moderately underexpanded jet (extracted from Franquet et al. [22]). Here, $p_b = p_\infty$ and, in this figure only, M is the mach number.

In this subject, a more detailed flow description is now presented, following the review work by Franquet et al. [22]. Figure 2.3 shows a sketch of the typical flow structure of an underexpanded air jet, with roughly $1.1 < p_e/p_b < 3$, corresponding to a moderate condition. In general, the structure has the following features:

- Isentropic expansion, marker 0. In general, the sonic conditions are obtained at the nozzle or tuyere exit plane.
- A set of characteristic lines, i.e. Prandtl–Meyer fan (marker 2), or physically sound waves are present close to the nozzle or tuyere exit plane .
- The Jet Boundary (JB) starts roughly at the nozzle or tuyere edge, marker 1, due to the expansion.
- The expansion lines interact, which are physically acoustic waves, generating a non-simple region. These characteristics are reflected once the ambient pressure is reached, generating the jet core boundary (marker 3), where Ma=1, defining the sonic line.

- Expansion lines converge towards the jet axis, generating two oblique shock across which the flow is no longer isentropic (marker 4). The inner region created by the shocks is supersonic and in the outer region, subsonic flow is obtained. This shock structure defines the first cell.
- The oblique shocks reflect at the jet axis, generating another pair of oblique shocks (marker 5) which in turn generate a new expansion fan and the process repeats, generating a new cell, until the ambient pressure is reached and the sonic line closes, defining the core length. In parallel, the jet boundary develops mainly characterized by turbulent flow.
- Although not shown, downstream where the core ends, flow is subsonic and it can be described by typical turbulent jet analysis.

2.1.2. Fanno Flow

The characteristics of a gas flow (compressible) in a tuyere depend strongly on its velocity as changes in density and friction on the walls (considered hydrodynamically smooth) begin to be more relevant. Thus, when the flow is subsonic the changes in density are irrelevant in temperature and pressure variables when the Mach number, $Ma = u/c$ -where u is a reference velocity and c, the speed of sound- is such that Ma <0.3 and then it is valid to perform pressure and velocity calculations at different positions of the duct, using the Boernoulli equation, implying that the gas can be approximated as an incompressible fluid. Thus, the pressure gradient and velocity in the duct of uniform cross section are constant.

When Ma >0.3 the density changes begin to take greater relevance in the temperature, pressure and velocity variables at different positions in the tuyere. Thus, the pressure and velocity gradient as a function of tuyere position is nonlinear. This characteristic is the most relevant in high velocity flows inside tuyeres and determines its sizing and operational conditions.

For subsonic flow with $Ma > 0.3$, in a tuyere, the relationship between thermodynamic and fluid dynamic quantities is obtained by integrating the mass, momentum and energy balance equations.

The sketch in Figure 2.4 is useful to show the typical analysis made for a straight tuyere. Given a tuyere section of length L, hydraulic diameter d, and an absolute roughness e_r, faced with a shear stress τ, the ratio between the Mach number (M) at the inlet (indicated by the number 1) and outlet (indicated by the number 2) of the tuyere is obtained from equation 2.5, valid for steady and adiabatic flow.

$$\frac{dMa}{dx}\frac{2(1-Ma^2)}{\gamma Ma^2}\left(1+\frac{\gamma-1}{2}Ma^2\right)^{-1}=\frac{4f}{d_0} \tag{2.5}$$

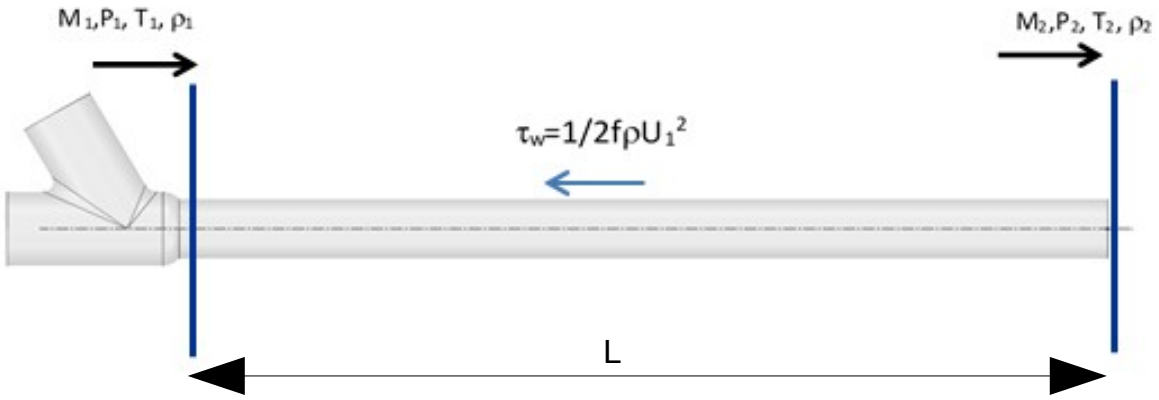

Figure 2.4: Sketch of a tuyere with length, L, and diameter, d. Inlet and and outlet planes are indicated with a suffix 1 and 2, respectively.

The derivation of the above widely known equation can be found in the book by Anderson [2].

which by integration gives equation 2.6

$$\left[\frac{-1}{\gamma Ma^2}-\frac{\gamma+1}{2\gamma}\ln\left[\frac{Ma^2}{1+\frac{\gamma-1}{2}Ma^2}\right]\right]_1^2=\frac{4f}{d}(x_2-x_1) \tag{2.6}$$

where x_1 is the position at the inlet and x_2 at the outlet, such that L = x_2 - x_1, f is the Fanning friction factor, which can be considered as constant given the high Reynolds number of the flow, and γ is the ratio between specific heats, which for ideal gas is γ= 1.4.

In the case where $M_2 = 1$, there is a critical length L^* that can be computed from equation 2.7.

$$\frac{4fL^*}{d}=\frac{1-Ma_1^2}{\gamma Ma_1^2}+\frac{\gamma+1}{2\gamma}\ln\left[\frac{(\gamma+1)Ma_1^2}{2-(\gamma-1)Ma_1^2}\right] \tag{2.7}$$

From this result it is possible to obtain, given an inlet velocity and in a direct way, the necessary length of pipe to obtain sonic conditions in the outflow. Alternatively, this equation establishes that given a tuyere length L*, with the sonic flow condition at the outlet, it is possible to obtain the required inlet velocity, using an iterative method or

tabulated values for the term. Then, from equation 2.7 it is possible to obtain Ma_1, p_1, T_1 and the (absolute) total inlet pressure, $p_{1,tot}$, estimated roughly with equation 2.8.

$$p_{1,tot} = p_{atm} + p_1 + \frac{1}{2}\rho_1 \left(Ma_1\sqrt{\gamma R T_1}\right)^2 \tag{2.8}$$

Other important results correspond to the relationships between the inlet and outlet properties, obtained from the mass, energy and state balance equations for ideal gases. Thus, the pressure ratio between the inlet and outlet are obtained from equation 2.9.

$$\frac{p_2}{p_1} = \frac{Ma_1}{Ma_2}\sqrt{\frac{2+(\gamma-1)Ma_1^2}{2+(\gamma-1)Ma_2^2}} \tag{2.9}$$

The temperatures at the inlet and outlet are obtained from equation 2.10.

$$\frac{T_2}{T_1} = \frac{2+(\gamma-1)Ma_1^2}{2+(\gamma-1)Ma_2^2} \tag{2.10}$$

While the density ratio is calculated with equation 2.11.

$$\frac{\rho_2}{\rho_1} = \frac{Ma_1}{Ma_2}\sqrt{\frac{2+(\gamma-1)Ma_2^2}{2+(\gamma-1)Ma_1^2}} \tag{2.11}$$

The relationships for Mach number, pressure, temperature, and density evaluated at two points of a uniform section pipe are applied to determine the tuyere dimensions.

The solution for the flow inside a submerged tuyere, applied to the blowing process in a reactor, is based on the given tuyere length, diameter, outer or back-pressure, p_b, and level of submergence in the liquid H_l, given in equation 2.12.

$$p_b = (p_{atm} + \rho_l g H_l)\eta_e \tag{2.12}$$

where p_atm is the atmospheric pressure, and η_e>1 is the level of underexpansion (recall that for the present application, the inlet velocity will be subsonic).

To represent the effect of variation in diameter and length, Figure 2.5 shows a surface plot that is useful to obtain the static inlet pressure, obtained by setting M_2=1, η_e=2 and $p_b = 1.2p_{atm}$.

It is clear from the surface plot that smaller tuyere diameter and longer length requires larger pressure, varying non-linearly with these parameters. In particular, the reduction

in diameter is more sensitive than length in terms of inlet static pressure.

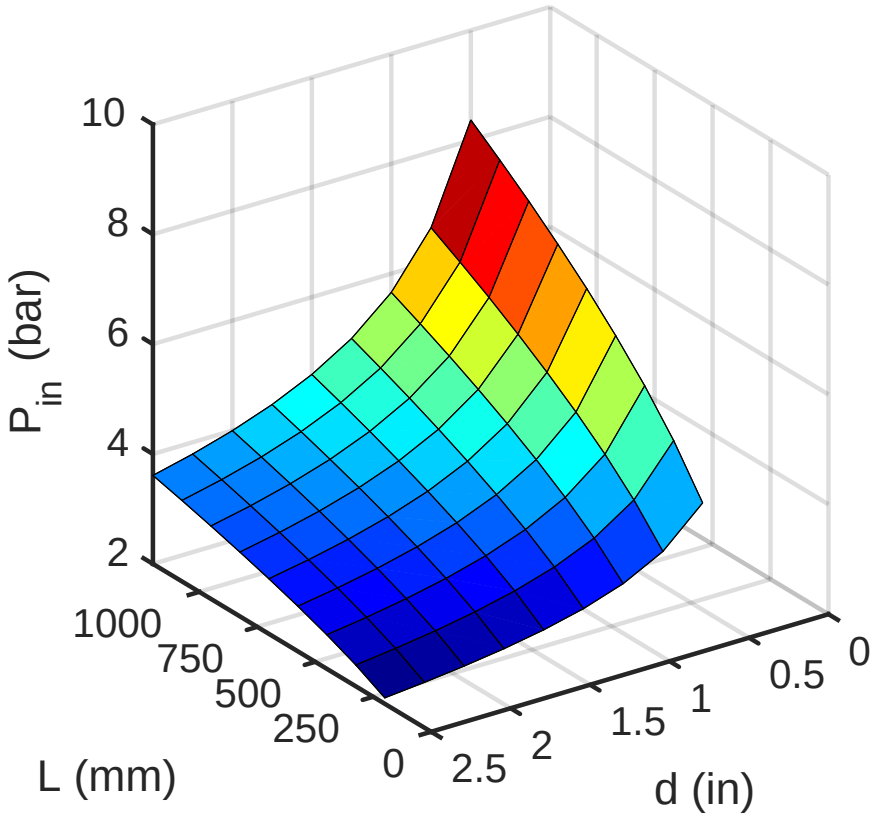

Figure 2.5: Manometric static inlet pressure as a function of tuyere length, L, and diameter, d.

Thus, using equations 2.7 to 2.10 are used to estimate total inlet pressure and total inlet temperature. These parameters are the relevant ones to describe the tuyere operation and will be used later in the boundary condition definition, given an underexpansion level.

2.1.3. The Themelis Jet

The work by Themelis et al. [54] shows a first approach to the mathematical description of submerged jets originating from a tuyere (or nozzle) of diameter d_0, having an exit velocity u_0, with an initial angle θ_c related to the Prandtl-Meyer expansion fan in underexpanded flows. The analysis is based on a simple form of the balance equations for continuity and momentum of a jet, using an infinitesimal element of thickness dx and a certain diameter $d(x)$ with an axis that forms an angle θ with the horizontal.

As a review, the following shows the main balance equations and the resulting equation for the jet trajectory. Then, a numerical solution of this equation is presented along with a parametric analysis of results.

The mass balance reads as in equation 2.13.

$$\rho_g u_0 d_0^2 = \rho_j u_x d^2 \alpha_g \tag{2.13}$$

where u_x is the velocity at a point x from the jet exit, having a diameter d; ρ_g is the gas density (e.g. air) ρ_j is the mixture density between the liquid density, ρ_l, and the gas density ρ_g, is given by equation 2.14.

$$\rho_j = \rho_l(1 - \alpha_g) + \rho_g \alpha_g \tag{2.14}$$

The momentum balance near the injection point, neglecting buoyancy and local drag effects, is computed as in equation 2.15.

$$\rho_g u_0^2 d_0^2 = \rho_j u_x^2 d^2 \tag{2.15}$$

Further downstream where buoyancy is relevant, the horizontal momentum is computed from equation 2.16.

$$M \cos\theta = \pi d_0^2 / 4 \rho_g u_0^2 \tag{2.16}$$

The vertical momentum of an element of volume, V is calculated from equation 2.17

$$M \sin\theta = g(\rho_l - rho_g)V \tag{2.17}$$

It's variation along the jet trajectory is obtained by equation 2.18.

$$d(M \sin\theta)/ds = g(\rho_l - rho_g)dV/ds \tag{2.18}$$

where dV is the volume of the infinitesimal gas element, as obtained from equation 2.19.

$$dV = \frac{\pi d^2}{4} \frac{dx}{\cos\theta} \alpha_g \tag{2.19}$$

Using all equations and trigonometric identities, the jet trajectory can be obtained by solving the non-linear Ordinary Differential Equation (ODE) 2.20, with an initially

horizontal tuyere (or normal to the gravity vector).

$$\frac{d^2 y_r}{dx_r^2} = 4Fr^{-1}\tan^2(\theta_c/2)\left[1+\left(\frac{dy_r}{dx_r}\right)^2\right]^{1/2} x_r^2 \alpha_g \tag{2.20}$$

where $x_r = x/d_0$, $y_r = y/d_0$ and Fr is the Froude number in equation 2.21

$$Fr = \frac{\rho_g u_0^2}{g(\rho_l - \rho_g)d_0} \tag{2.21}$$

The initial conditions are (equation 2.22)

$$y_r = 0 \tag{2.22}$$

and (equation 2.23)

$$\frac{dy_r}{dx_r} = 0 \tag{2.23}$$

both evaluated at $x_r = \frac{1}{2\tan(\theta_c)}$.

Equation 2.20 can be solved by with a 4th order Runge-Kutta Method, yielding the jet centerline trajectory. This can be easily expanded to compute the jet boundary, with the (strong) assumption that it is continuous everywhere.

Figure 2.6 shows an applied example for the use of the Themelis Model. A submberged and underexpanded jet with $\theta_c \approx 20deg$, exits horizontally from a tuyere, blowing into an agitated tank reactor (e.g. Teniente Converter, Noranda reactor, Peirce-Smith Converter) of 4 m in diameter. The tuyere is located 1m below the molten bath metal that covers 1.8m, measured from the tank bottom. Two mass flow rates are compared, corresponding to two Froude numbers, Fr=100, 200, 300.

The jet trajectory shows a large deflection near the adjacent wall to the tuyere. The Themelis model predicts that, for Fr=100 and Fr=200 submerged jet center will emerge in a distance of about one third the surface length, and according to Rosales et al. [47], the asymmetric mode will not yield resonance or increased agitation. In contrast, for Fr=300 the jet emerges closer to the surface center, and then the agitation mode corresponds to a symmetric mode that will result in high agitation, and in practical application, this could mean large splashing and sloshing that is not desirable and even dangerous, since molten metal can be projected out of the reactor.

The Themelis jet equation is a rough, but useful mathematical model that allows a simple and powerful tool for sizing reactors, particularly the tuyere position and blowing characteristics.

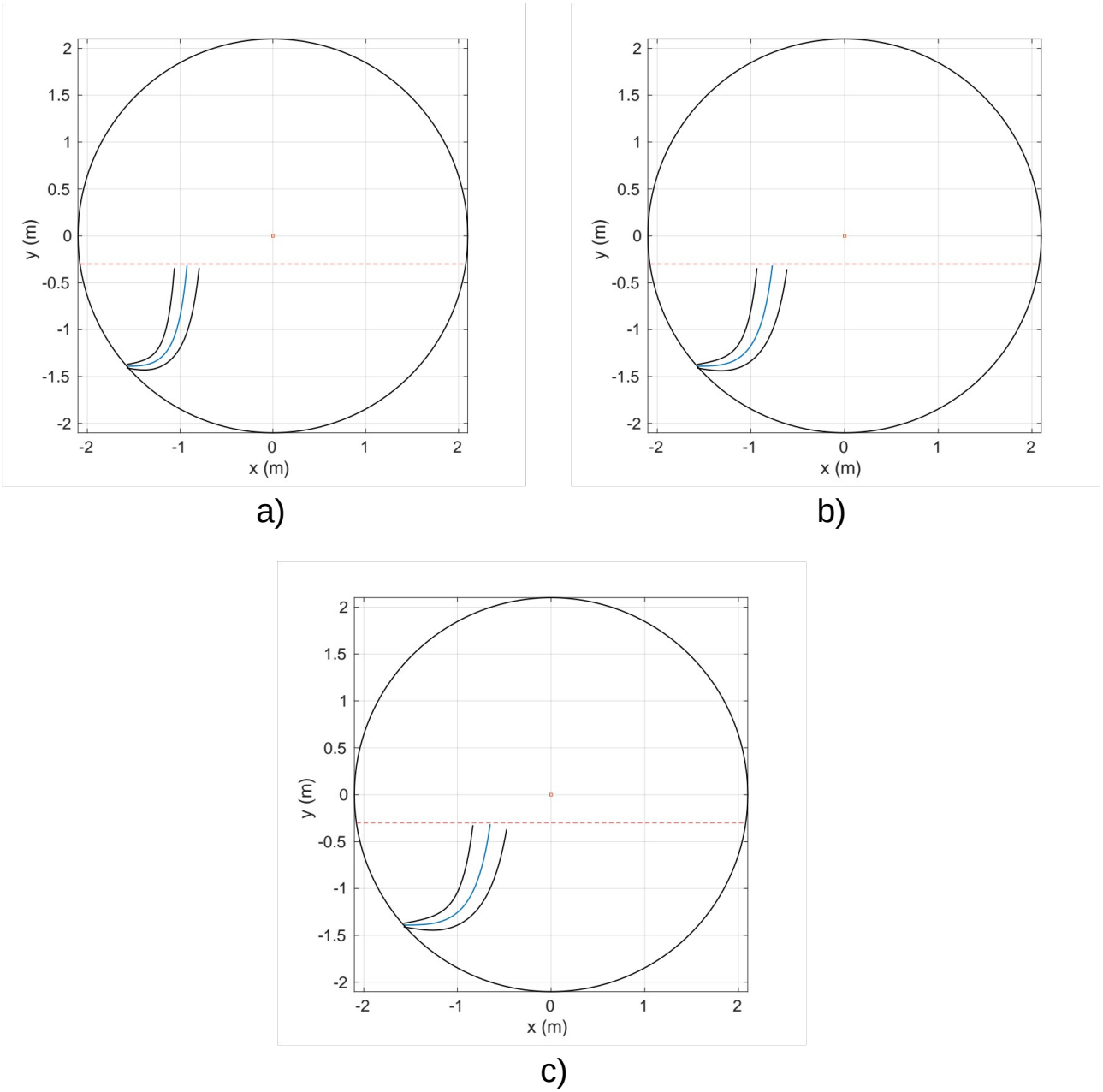

Figure 2.6: Jet trajectory at: a) $Fr = 100$, b) Fr=200, c) Fr=300

2.2. Statistical Description

2.2.1. Jet Characteristics

The jet characteristics that are presented in what follows are based on the work by Harby et al. [26] and Weiland & Vlachos [57].The first work shows a useful set of equations for inertial length, buoyant length, submerged jet expansion angle and jet half-width. The second work is useful to establish the relevance of different mechanisms in the jet behavior.

Figure 2.7 shows a sketch of typical penetration length, composed by an inertial and buoyant part.

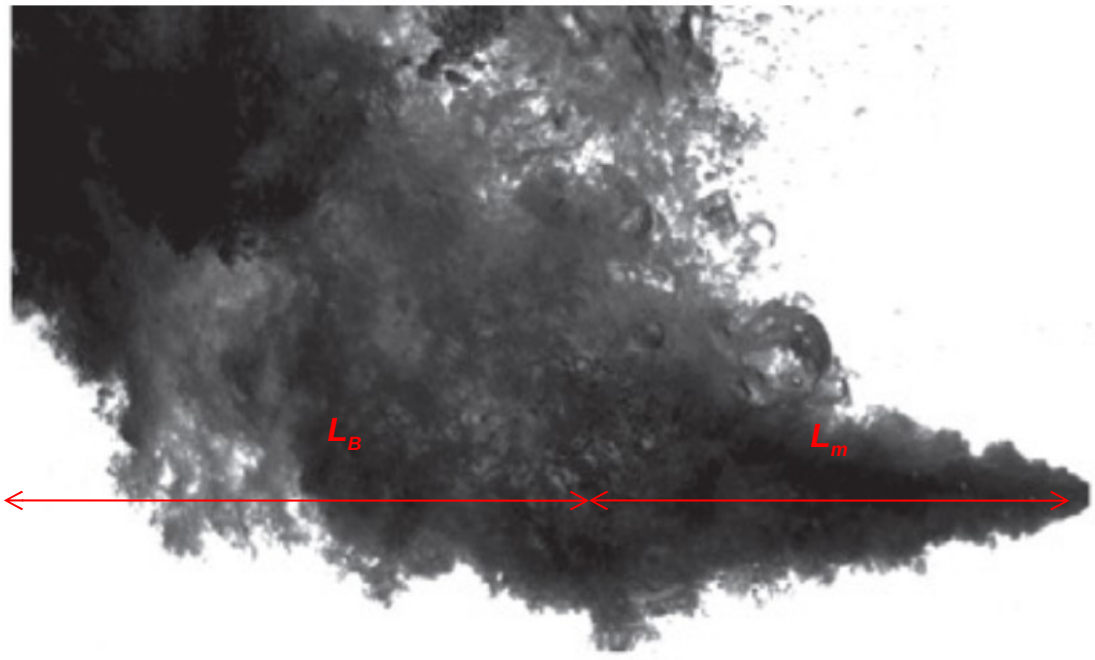

Figure 2.7: Penetration length of a horizontal underexpanded submerged jet, where L_m is the inertial part, and L_B is the buoyant lenth. Sketch based on the work by Harby et al. [26].

The inertial length of a submerged jet is related to its level of momentum, and can be represented in terms of the Froude number as (Harby et al. [26]) in equation 2.24.

$$L_m/L_q = a_1 Fr^{a_2} \tag{2.24}$$

where L_q=$\sqrt{A_0}$, A_0 is the tuyere (exit) cross-section, Fr is given by equation 2.21, and a_1=2.29 and a_2=0.305, are the model constants to fit the power law-like function.

This is scale is relevant as it quantifies the jet inertia is more important than buoyancy. It can be expected, though not expressed in the experimental work, that this scale is related to the inner structure of the jet, particularly when it is underexpanded. This has been already advanced by simulations (Gong et al. [24]) and experiments (Aoki [3], Loth & Faeth [32]).

The bouyant length is determined by the distance between the end point of the inertial length and the vertical line that is tangent to the jet boundary (Harby et al. [26]). This scale reveals where momentum is not enough to suppress hydrostatic pressure and then buoyancy becomes more important. In the experimental work, the buoyant length, L_B, is statistically better represented by a function of Fr, as shown in equation 2.25.

$$L_B/L_q = a_3 Fr + a_4 Fr^{1/2} + a_5 \tag{2.25}$$

where the model constants are a_3=0.0007(m), a_4=0.14(m), a_5=9.3.

The jet expansion angle corresponds to the measure of opening which can be different and larger than the typical 11 deg angle of a turbulent jet. It is important to notice that the expansion angle, θ_e, increases at non-linearly higher flow rate (Loth & Faeth [32]). In this case, the experimental work of Harby et al. [26] shows that θ_e is statistically better represented by equation 2.26:

$$\theta = a_6 \ln(u_0 \dot{m}_0) + a_7 \tag{2.26}$$

where $\dot{m}_0$ is the tuyere mass flow and, the models constants are a_6=2.227 and a_7=8.3953.

From this expression is can be observed that the cost of having a wider submerged is at the expense of much larger inlet pressure. For example, between small en large underexpansion levels, that is a increase by a factor of 5 in exit-to-back pressure ratio, there is only a 20% increase in the expansion angle.

The jet half-width measures the jet ability for entrainment and mixing. As found by Harby et al. [26] for a single tuyere, the half width is independent of the momentum and has the linear relation of equation 2.27

$$w/d_0 = a_8(x/d_0) + a_9 \tag{2.27}$$

where the model constants are a_8=0.19 and a_9=0.49.

This model agrees well with the experimental work of Drew et al. [18] that shows

that the jet half angle indicates a jet width that does not vary significantly with the exit velocity.

2.2.2. Entrainment

The entrainment in single phase jet is produced mainly due to KH type of instabilities, generating the jet boundary deformation. The mass flow entrained is also larger for an increasing distance, until the jet momentum dissipates, due to viscosity or Reynolds stresses, depending on the jet regime (see Pope [43] for details of turbulent jets).

When there is a different density of the jet and environment, Ricou & Spalding [45] found that the level of entrainment is increased, by a factor depending on the density ratio. The relation of the rate of entrainment along the streamwise direction, x, is given by equation 2.28.

$$\frac{d\dot{m}_e}{dx} = \frac{C_2}{d_0}\sqrt{\frac{\rho_l}{\rho_g}} \tag{2.28}$$

where C_2=0.32 a constant from experiments. This model indicates that the rate of entrainment is constant along the jet trajectory, which is similar, for example, to that of a single phase turbulent jet.

However, according to experimental work by Carreau et al. [11] and Loth & Faeth [32] show that the rate of entrainment has an approximate constant rate of entrainment only close to the injection point and that it increases non linearly with the streamwise direction. In the Loth & Faeth [32] experiment, the entrainment can be calculated with equation 2.29.

$$\frac{dm_{ent}}{dx} = 2\pi r_\infty \rho_l \left[u_\infty \tan(\beta) - v_\infty\right] \tag{2.29}$$

where m_{ent} is the mass flow entrained by the liquid. The term dm_{ent}/dx is calculated, using a conical surface of half-angle β, that corresponds to the jet boundary, and radius r_∞ outside the air interface; the streamwise, u_∞, and lateral velocities, v_∞, are both present outside jet boundary.

It is seen that entrainment depends on the jet velocity field away and downstream the jet boundary. This indicates that the jet inertial and buoyant portions determine the rate of entrainment behavior.

Regarding the effects of different jet behavior in the rate of entrainment, Epstein et al.

[19] shows a correlation, based on estimate of time scales of combined KH and Rayleigh-Taylor (RT) instabilities in surface waves. The total entrained mass flow is estimated with equation 2.30

$$m_{ent} \approx \frac{1}{\sqrt{3}}(\rho_g \rho_l)^{0.5} v \sqrt{\frac{6\lambda}{1+(1+3\lambda)^{0.5}}+1} \tag{2.30}$$

with

$$\lambda = \frac{\sigma a_b \rho_l}{\rho_g^2 v^4} \tag{2.31}$$

where a_b is the jet boundary acceleration (obtained by experiments), σ is the surface tension (air-water as in the present analysis), and v is the lateral jet velocity. This acceleration appears at the interface when density-driven buoyancy effects are present, where the internal pressure is variable, leading to the formation of waves. Following the analysis by Zhang et al. [59], this implies that a high degree of mixing occurs, as droplets are entrained and bubbles pinch-off the main jet structure, when large parts of fluids may approach its centerline.

When $\lambda << 1$, i.e. when inertia is relevant, the KH instability dominates entrainment, and then the asymptotic model for the entrained mass flow is given by 2.32.

$$m_{ent} \approx \frac{1}{3}\left(\rho_g \rho_l\right)^{1/2} v \tag{2.32}$$

When $\lambda >> 1$, i.e. when surface tension is the relevant force, the RT instability dominates entrainment, and it is computed with equation 2.33.

$$m_{ent} \approx \frac{2}{3}\left(\frac{3\sigma a_b}{\rho_l}\right)^{1/4} \rho_l \tag{2.33}$$

where a_b is the interface acceleration, which for a submerged jet can be obtained by experimental techniques (see Weiland & Vlachos [57]).

The experiments by Drew et al. [18] show that the value of λ is higher close just outside the injection point, indicating that RT instabilities predominate, but decreases fast within the inertial length, indicating that KH instabilities are predominant, and then λ increases again away from its endpoint. Also, it is shown that for increasing (supersonic) exit velocity, entrainment is explained mainly due to KH type of instabilities.

In addition Drew et al. [18] shows through PIV and image analysis that both Ricou

& Spalding [45] and Epstein et al. [19] (full) models seem to be more representative in the range $0 < x/d < 10$, but the last model being more accurate in this range. However, $x/d > 10$ the Epstein et al. [19] model overpredict the rate of entrainment, but still offers better qualitative results, while Ricou & Spalding [45] underpredicts the experimental values. Regarding the asymptotic, the KH model underpredicts the rate of entrainment but shows some qualitative behavior consistent with the experimental results in the range $0 < x/d < 10$. Therefore, it is possible to say that the main trigger of entrainment effects is the KH instability, which is similar to what happens in single phase turbulent single-phase jets (see Pope [43]).

2.3. Main Governing Equations

The main governing equations for jets are analyzed in the following subsections. In particular, the equations for continuity of phases and energy are derived to obtain its form that is better representative of the submerged compressible flow.

The following equations are solved for mixture values ϕ, expressed as $\phi = \alpha_1\phi_1 + \alpha_2\phi_2$, where ϕ_i represents flow variables (velocity, $\mathbf{U}$, temperature, T) and also phases properties (density, viscosity) , where i=1 corresponds to air and i=2, to water (later, the index 1 is dropped for ease of use).

2.3.1. Continuity and Momentum

The Continuity equation is solved for the mixture velocity field, $\mathbf{U}$, and is given by equation 2.34.

$$\frac{\partial \rho}{\partial t} = -\nabla \cdot (\rho \mathbf{U}) \tag{2.34}$$

The momentum equation, for constant molecular viscosity of the phases, is given by equation 2.35.

$$\frac{\partial \rho \mathbf{U}}{\partial t} + \nabla \cdot (\rho \mathbf{U}\mathbf{U}) = -\nabla(p + \frac{2}{3}\mu_{eff}\nabla \cdot \mathbf{U}) + \nabla \cdot (\mu_{eff}\nabla \mathbf{U}) + \nabla \mathbf{U} \cdot \nabla \mu_{eff} + \rho \mathbf{g} + f_{int} \tag{2.35}$$

where μ_{eff} is the effective viscosity, with μ_{eff}=μ +μ_t, μ is the molecular property, and μ_t is obtained by the turbulence model. The term $\mathbf{g}$ is the gravity vector $(-9.81, 0, 0)$ in m/s^2. The surface tension force, f_{int}, is expressed by the Continuum Surface Force model of Brackbill et al. [7], according to equation 2.36.

$$f_{int} = \int_V \sigma \kappa \nabla \alpha_1 dV \tag{2.36}$$

where $\sigma = 0.072 N/m$ is the air-water surface tension used in this study, and the surface curvature of α_1 is $\kappa = \nabla \cdot (\frac{\nabla \alpha_1}{|\nabla \alpha_1|})$.

2.3.2. Volume Fraction

The continuity of phases, for phase i (with i=1,2), without mass transfer between phases, is given by equation 2.37.

$$\frac{\partial \alpha_i \rho}{\partial t} + \nabla \cdot (\rho \alpha_i \mathbf{U}_i) = 0 \tag{2.37}$$

With ρ is the mixture density given by equation 2.38.

$$\rho = \alpha_1 \rho_1 + \alpha_2 \rho_2 \tag{2.38}$$

Expanding 2.37 in the left hand side (LHS) yields equation 2.39

$$\rho \frac{\partial \alpha_i}{\partial t} + \alpha_i \frac{\partial \rho}{\partial t} + \rho \nabla \cdot (\mathbf{U}_i \alpha_i) + \alpha_i \nabla \cdot (\rho \mathbf{U}_i) = 0 \tag{2.39}$$

which can be re-arranged as equation 2.40:

$$\frac{\partial \alpha_i}{\partial t} + \nabla \cdot (\mathbf{U}_i \alpha_i) = -\frac{-\alpha_i}{\rho_i} \frac{D\rho_i}{Dt} \tag{2.40}$$

where $\frac{D(\cdot)}{Dt}$ corresponds to the material derivative operator. Setting up two equations, one for each phase, (2.41 and 2.42).

$$\frac{\partial \alpha_1}{\partial t} + \nabla \cdot (\mathbf{U}_1 \alpha_1) = -\frac{-\alpha_1}{\rho_1} \frac{D\rho_1}{Dt} \tag{2.41}$$

$$\frac{\partial \alpha_2}{\partial t} + \nabla \cdot (\mathbf{U}_2 \alpha_2) = -\frac{-\alpha_2}{\rho_2} \frac{D\rho_2}{Dt} \tag{2.42}$$

Multiplying equation 2.41 by α_2 and equation 2.42 by $-\alpha_1$, adding them results in equation 2.43:

$$\alpha_2 \frac{\partial \alpha_1}{\partial t} + \alpha_2 \nabla \cdot (\mathbf{U}_1 \alpha_1) - \alpha_1 \frac{\partial \alpha_2}{\partial t} - \alpha_1 \nabla \cdot (\mathbf{U}_2 \alpha_2) = \frac{-\alpha_2 \alpha_1}{\rho_1} \frac{D\rho_1}{Dt} + \frac{\alpha_2 \alpha_1}{\rho_2} \frac{D\rho_2}{Dt} \tag{2.43}$$

The LHS of equation 2.43 can be further modified, conveniently in terms of α_1, to:

$$LHS = (1 - \alpha_1) \frac{\partial \alpha_1}{\partial t} + (1 - \alpha_1) \nabla \cdot (\mathbf{U}_1 \alpha_1) + \alpha_1 \frac{\partial \alpha_1}{\partial t} - \alpha_1 \nabla \cdot (\mathbf{U}_2 \alpha_2) \tag{2.44}$$

Equation 2.44 can be expanded by making use of the chain rule yielding equation 2.45.

$$LHS = \frac{\partial \alpha_1}{\partial t} + \nabla \cdot (\alpha_2 \alpha_1 \mathbf{U}_1) - \nabla \alpha_2 \cdot (\alpha_1 \mathbf{U}_1) - [\nabla \cdot (\alpha_1 \alpha_2 \mathbf{U}_2) - \nabla \alpha_1 \cdot (\alpha_2 \mathbf{U}_2)] \tag{2.45}$$

After some manipulation the LHS reads as in equation 2.46.

$$LHS = \frac{\partial \alpha_1}{\partial t} + \nabla \cdot (\alpha_2 \alpha_1 \mathbf{U}_r) + \nabla \alpha_1 \cdot (\alpha_1 \mathbf{U}_1) + \nabla \alpha_1 \cdot (\alpha_2 \mathbf{U}_2) \tag{2.46}$$

where $\mathbf{U}_r = \mathbf{U}_1 - \mathbf{U}_2$. In addition, the mixture velocity U is expressed as equation 2.47.

$$\mathbf{U} = \alpha_1 \mathbf{U}_1 + \alpha_2 \mathbf{U}_2 \tag{2.47}$$

Then equation 2.48 is obtained.

$$LHS = \frac{\partial \alpha_1}{\partial t} + \nabla \cdot (\alpha_1 (1 - \alpha_2) \mathbf{U}_r) + \nabla \alpha_1 \cdot \mathbf{U} \tag{2.48}$$

Using the chain rule for the last term in 2.46, yields equation 2.49.

$$LHS = \frac{\partial \alpha_1}{\partial t} + \nabla \cdot (\alpha_1 (1 - \alpha_1) \mathbf{U}_r) + \nabla \cdot (\alpha_1 U_1) - \alpha_1 \nabla \cdot \mathbf{U} \tag{2.49}$$

Then equation 2.42 is transformed to equation 2.50.

$$\frac{\partial \alpha_1}{\partial t} + \nabla \cdot (\alpha_1 U_1) + \nabla \cdot (\alpha_1 (1 - \alpha_1) \mathbf{U}_r) = \alpha_1 (1 - \alpha_1) \left[\frac{1}{\rho_2} \frac{D\rho_2}{Dt} - \frac{1}{\rho_1} \frac{D\rho_1}{Dt} \right] + \alpha_1 \nabla \cdot \mathbf{U} \tag{2.50}$$

Noticing that for air (i=1), the density is modeled as an ideal gas and that water (i=2) may be described in general with an isochoric model of equations 2.51 and 2.52.

$$\rho_1 = \psi_1 p \tag{2.51}$$

$$\rho_2 = \rho_{2,0} + \psi_2 p \tag{2.52}$$

In the above equations, $\psi_i = 1/c^2$- where c is the sound velocity in phase i- corresponds to the compressibility factor. For air $\psi_1 = 1/(\gamma R_1 T_1)$, with $R_1 = 286.9 J/kgK$ the individual gas constant for air and T_1 its temperature; and for water, $\psi_2 << 1$, i.e. considered as incompressible. It is important to remark at this point that water density can vary under very high pressure, ranging around 1GPa (Suponitsky et al. [51]).

Introducing equations 2.51 and 2.52 into 2.50, the continuity of the compressible phase α_1, i.e. air, is obtained in equation 2.53 (as expressed in the OpenFoam solver OpenFOAM [38]).

$$\frac{\partial \alpha_1}{\partial t} + \nabla \cdot (\alpha_1 \mathbf{U}) + \nabla \cdot (\alpha_1 (1-\alpha_1)(\mathbf{U}_1 - \mathbf{U}_2)) = \alpha_1 (1-\alpha_1)(\frac{\psi_2}{\rho_2} - \frac{\psi_1}{\rho_1})\frac{Dp}{Dt} + \alpha_1 \nabla \cdot \mathbf{U} \tag{2.53}$$

Equation 2.53 represents continuity of one phase (air in this case) where the contribution from the other phase and the changes in phase's density. In particular, the third term in the LHS represents the "compression" term of the phases near their interface. The right hand side are source terms that account for density changes of each phase due to pressure fluctuations and mixture density.

2.3.3. Turbulence

Turbulence is included in the simulations through the Unsteady Reynolds Navier-Stokes (URANS) model k-ω SST model, known to be more accurate when dealing with high-velocity compressible flows (value of constants are found in OpenFOAM [38]). These equations are 2.54 and 2.55 (as expressed in the solver).

$$\frac{\partial \rho k}{\partial t} = \nabla \cdot (\rho D_k \nabla k) + \rho G - \frac{2}{3}\rho k \, (\nabla \cdot \mathbf{U}) \tag{2.54}$$

$$\frac{\partial \rho \omega}{\partial t} = \nabla \cdot (\rho D_\omega \nabla \omega) + \frac{\rho \gamma G}{\nu} - \frac{2}{3}\rho \gamma \omega \, (\nabla \cdot \mathbf{U}) - \rho \beta \omega^2 - \rho \, (F_1 - 1) \, C D_{k\omega} + \tag{2.55}$$

In this turbulence model it is possible to include compressibility effects in the specific dissipation equation, but it is recommended and calibrated for specific applications only (Wilcox [58]). Birkby & Page [6] shows that k-ω SST with compressibility correction improves the developed flow downstream the potential core, but shows little change in predicted shock cell structure close to the injection point. In addition, the correction to transport equations in the URANS turbulence models would need to be calibrated for the underexpanded air injection into water, and then further numerical studies are required to establish the applicability of different correction models. This is outside the scope of this study, and it is proposed as a future work.

It is known that Large Eddy Simulations (LES) are more accurate to resolve underexpanded jets (Vuorinen et al. [56]). For submerged jets, it can be expected that LES would perform better than the k-ω SST model, but implementation of LES needs to be evaluated in detail. In spite of this, as a first approach to the study of submerged air jets interaction, the selected URANS model offers stability and enough accuracy for this application. In addition, it requires less computational effort compared to LES. Moreover, to the date of this article, the authors have not found references of LES to analyze air jets injected into water.

2.3.4. Energy Equation

The energy equation for a phase i (with i=1,2) without viscous dissipation effects, mass and heat transfer; sink and source terms is given by equation 2.56.

$$\frac{\partial \alpha_i \rho_i e_i}{\partial t} + \nabla \cdot (\alpha_i \rho_i e_i \mathbf{U}) + \alpha_i \nabla \cdot (\mathbf{U}p) + \alpha_i \frac{DK}{Dt} = \nabla \cdot (\alpha_{eff} \nabla e_i) \tag{2.56}$$

where $e_i = c_{v,i}T$ is the internal energy (for both an ideal gas and incompressible fluid), T is the mixture temperature, K=$1/2|U|^2$ is the kinetic energy, α_{eff} is the effective thermal diffusivity. The terms $c_{v,1}$ and $c_{v,2}$ correspond to the specific heat (at constant volume) for air and water, respectively.

Equation 2.56 can be expanded to equation 2.57.

$$c_{v,i}\frac{\partial \alpha_i \rho_i T}{\partial t} + c_{v,i}\nabla \cdot (\alpha_i \rho_i T \mathbf{U}) + \alpha_i \nabla \cdot (\mathbf{U}p) + \alpha_i \frac{DK}{Dt} = \nabla \cdot (\alpha_{eff} c_{v,i} \nabla T) \tag{2.57}$$

Adding equations 2.57 for i=1,2, leads to the energy equation 2.58, as expressed in the OpenFoam solver (OpenFOAM [38]).

$$\frac{\partial \rho T}{\partial t} + \nabla \cdot (\rho \mathbf{U} T) + \left(\frac{\alpha_1}{c_{v,1}} + \frac{1 - \alpha_1}{c_{v,2}} \right) \left(\frac{\partial \rho K}{\partial t} + \nabla \cdot (\rho \mathbf{U} K) + \nabla \cdot (\mathbf{U} p) \right) = \nabla^2 (\alpha_{eff} T) \tag{2.58}$$

Chapter 3

Simulations Setup

3.1. Geometry and Grid

Figure 3.1 shows the single and twin tuyere configurations. In the first, a tuyere of uniform circular cross-section, with diameter d and a length l, is connected to the center-bottom of a cylindrical water tank of diameter D=750 mm and a height H=2000 mm, with the water level being H_w=1500 mm. In particular, and similar to the Loth & Faeth [32] experiment, the tuyere inner diameter is d=11 mm and its length is l=230 mm, so their ratio is l/d=20.9. In the second configuration, two identical tuyeres are symmetrically placed about the xz-plane at y/d=0 and connected to the tank bottom wall, having a tuyere interspace, s, measured between centers. Furthermore, the length s has a minimum value of $s/(d+2e)$=1, where e is a certain tuyere thickness. In this way, realistic geometries are considered, leaving the situation where s/d=1 out of the scope of this study.

The tank diameter is selected to avoid wall effects, specifically from pressure reflection and flow recirculation. As in the experimental work by Loth & Faeth [32], the smallest side of the rectangular water tank base is D=1000 mm, so the tank-diameter-to-tuyere-diameter ratio is $D/d \approx$91. In this study, the ratio is $D/d \approx$68 for the single jet configuration, and for the twin jet setup the tank-diameter-to-interspace ratio is between $D/s \approx$38 and $D/s \approx$59.

The 3D geometry is divided into two equal parts, using a xy-plane at z/d=0, each containing sub-blocks. The mesh, shown in Figure 3.2, is generated using Ansys Meshing, where the sub-blocks are used to obtain an ordered and almost symmetric mesh.

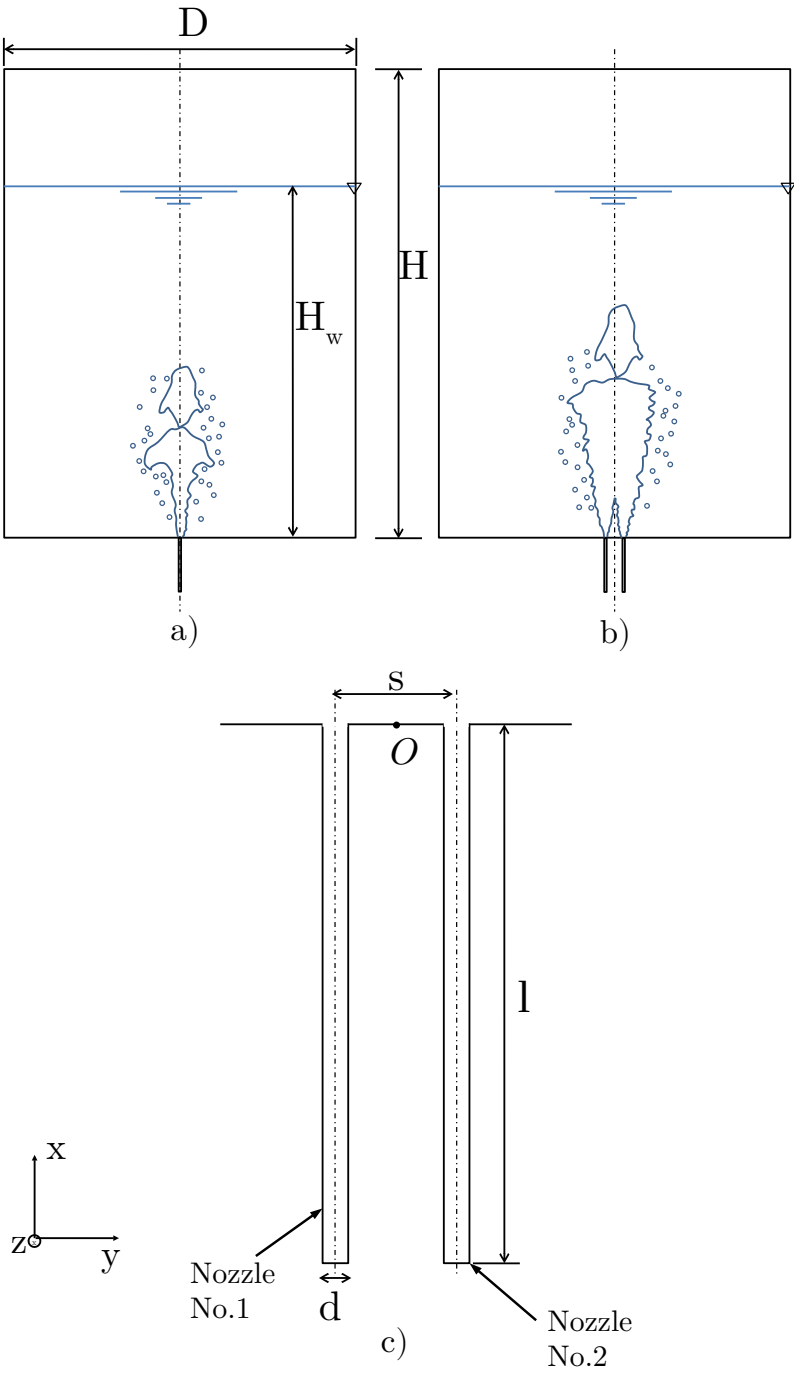

Figure 3.1: Sketch of the (3D) geometry used in the submerged jets simulations. The origin, O, is placed at the bottom center of the water tank, having a diameter, D=750mm, height, H=2000mm; The water level is H_w=1500mm. In this figure: a) single tuyere configuration, b) Twin tuyere configuration, c) enlargement of the twin tuyere configuration, showing the tuyere number. The tuyeres in both single and twin configurations are straight, having an internal diameter, d=11mm, and a length, l=230mm, and thickness, e (not shown). The spacing between tuyeres is s, and it is considered that $s/(d+2e) \geq 1$.

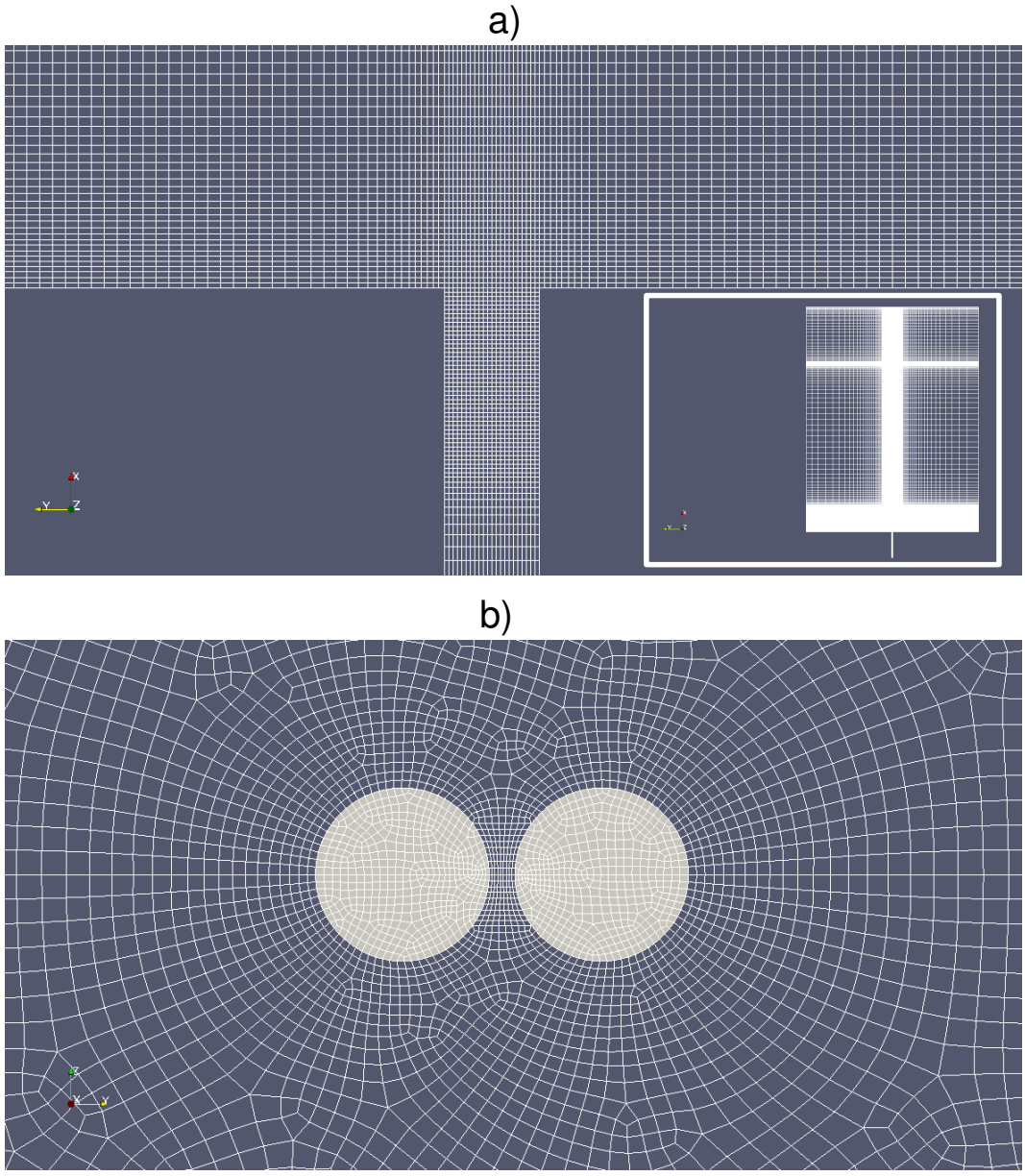

Figure 3.2: Grid of: a) Single tuyere configuration, showing an enlargement close to tuyere exit with a mini-view (bottom-right corner) of the complete grid in the xy-plane at $z/d = 0$, b) Twin tuyere configuration, showing a view in the yz-plane at x/d=0.

The grid is generated with refinement around the tuyeres in both single and twin configurations, using a cylindrical block of length $20d$ and diameter $17d$. The smallest size is $\Delta x_{min}/d = 1/22$ and it is located at the tuyere exit. Grid growth rate from this size is 5%, directed inside and outside the tuyere. This is done to capture the typical potential core length, of about $10d$ to $15d$ in the streamwise direction, and to resolve lateral motions of the jet. Downstream this block smooth transitions are made from fine to coarse grid size, using growth ratios between 5% to 8%. In addition, refinement is

implemented, using the same growth ratios, around the surface water level and the top part of the water tank. With this, the grids for single and twin configurations have, respectively, 2.6 and 2.7 million hexahedral cells, where about 55% of the cell count is in the cylindrical block.

3.2. Solution Methods

3.2.1. Physical Models

The *compressibleInterfoam* module in OpenFoam (OpenFOAM [38]) is used to solve the interaction of two compressible and non-isothermal immiscible fluids, using the volume of fluid model (VOF) with an interface capturing approach. This module addresses high-velocity flow, i.e. where compressibility becomes important in the following equations that will are used in the simulations:

- Continuity.
- Momentum.
- Continuity of phases (Volume of Fluid, VOF)
- Turbulence.
- Energy

Here, the air is considered as an ideal gas and for water, a constant density is used. For details of the equations, see Chapter 2, section 2.3.

3.2.2. Boundary and Initial Conditions

Inlet conditions are estimated, using one-dimensional (Fanno flow) equations, using zero absolute roughness for the tuyere walls, keeping in mind that they fail to represent the zone beyond where the sonic velocity is reached inside the tuyere (Lijo et al. [31]).

The total pressure and temperature at the tuyere's inlet are prescribed, where both parameters NPR and $\eta_{e,th}$ are varied, as shown later. The "ambient" pressure, p_b, corresponds to the (absolute) hydrostatic pressure at the tank bottom. This is similar to the normalization of pressure in single-phase air jets, where atmospheric pressure, p_{atm}, determines the underexpansion level. This parameter is set arbitrarily at p_{atm}=10^5 Pa. Furthermore, in the momentum equation, pressure, p, is absolute and thus the atmospheric pressure is needed. With this, the hydrostatic pressure is included in the inlet boundary condition as

$$p_b = p_{atm} + \rho_2 g H_w \tag{3.1}$$

While the term p_e is obtained from the following relation (at the tuyere exit, Ma_2=1 in equation 2.9)

$$\frac{p_e}{p_{in}} = Ma_{in}\sqrt{\frac{2+(\gamma-1)Ma_{in}^2}{\gamma+1}} \tag{3.2}$$

Calculated for an exit Mach number, $Ma_e = 1$, where p_{in} is the static pressure at the tuyere inlet, and Ma_{in} is the Mach number at the tuyere inlet. The latter value is calculated from

$$\frac{4fl}{d} = \frac{1-Ma_{in}^2}{\gamma Ma_{in}^2} + \frac{\gamma+1}{2\gamma}\ln\left(\frac{(\gamma+1)Ma_{in}^2}{2+(\gamma-1)Ma_{in}^2}\right) \tag{3.3}$$

Where f the Fanning friction factor.

The turbulence intensity at the tuyere inlet, I, is estimated with the correlation I=$0.16Re^{-1/8}$ (used by Valencia et al. [55]. Similar correlations are found in the work by Basse [4]), that is used for developed turbulent flow in a pipe. Also, the ratio l/d=20.9 ensures this holds (Loth & Faeth [32]).

At the tank top, atmospheric air pressure and temperature values are prescribed. Backflow conditions are also set (velocity, temperature and pressure), but are not expected to have a relevant influence in the results.

The tank and tuyere's walls have a non-slip and no penetration condition. In the energy equation, walls are adiabatic. For the turbulent kinetic energy and specific dissipation equations, built-in wall functions are used.

The initial conditions for the simulations are the same for all cases (defined later). At time t=0 s the height of water inside the tank is H_w=1500 mm. The tuyeres arranged in the single and twin configurations are pressurized with air, where the initial static pressure corresponds to the total pressure prescribed at the inlet. This type of setting for the initial condition has been used in simulations for highly underexpanded flows by Vuorinen et al. [56]. In addition, pressure in the tank is set equal to the atmospheric pressure and the tuyere volume has the same pressure value prescribed at its inlet. With this initial condition, the injection starts at rest, then with subsonic velocities, accelerating as the gas expands while pressure drops accordingly, reaching the sonic velocity inside the tuyere. This is a simplification of a more simple and direct initial condition, where the tuyere starts filled with water and then air must move the small liquid column, achieve the initial subsonic regime, and then make the transition to the sonic condition. Although the resulting initial flow may vary with different initial conditions, by starting

with a pressurized tuyere it is possible to save considerable computational time since the interesting flow feature is the continuous gas flow (Miao et al. [33]), achieved after the first bubble pinch-off event. Furthermore, after the first recorded time step, the hydrostatic profile is obtained and no surface level oscillations are observed. Moreover, the first bubble is not taken into account for the statistical analysis, since it is expected that the simpler initial condition will change bubble-growth and pinch-off times.

3.2.3. Numerical Schemes and Solution

The numerical schemes is summarized in what follows:

- For time discretization, a first order implicit Euler scheme is used in all time-dependent equations, and chosen mainly for stability reasons.
- The gradients are computed with a linear scheme with a multi-directional cell limiter. This choice is made upon stability considerations of the simulation, given the high gradients of flow variables, particularly pressure and velocity.
- The surface-normal gradients scheme is linear with full orthogonal correction. This enforces correction particularly in cells close to the tuyere walls.
- The divergence scheme for all variables (volume fraction, velocity, pressure, energy, k and ω) corresponds to second order linear upwind. This scheme is used for accuracy and stability.
- Second order spatial derivatives (Laplacians) are computed using an unbounded linear scheme, given the low non-orthogonality of the meshes used in the single and twin configurations.
- The interpolation between cell and faces used is the van Leer scheme. Although typical linear interpolations are often used and recommended, in preliminary test runs, this method offered slightly better smoothing effects across air-water interface.

The numerical solution is similar to that found in the incompressible solver that uses the VOF method in OpenFOAM, *interFoam*. The general algorithm is listed below.

- Initiate fields
- Start runtime
  - Time step calculation
  - Iterating over the PIMPLE Loop nOuterCorrectors times
    - Solving the equation for α (VOF and MULES)
    - Compute the mixture properties (ρ, α, surface tension)
    - Solve the momentum equation

    - Pressure correction (PISO loop)

- Calculate the turbulence properties

In particular, the numerical solution is set as follows

- The maximum Courant number, Co, is kept at Co=0.2 for the gas phase and for the gas-liquid interface. With the minimum grid size of $\Delta x_{min}/d = 1/22$ and a velocity scale equal to the sonic velocity,$u_s = \sqrt{\gamma R T_a}$, then the time step, Δt, has a value of $\Delta t = Co\ u_s\ /\Delta x_{min} \approx$ 2.1e-7s.

- The pressure-velocity coupling is solved using the PIMPLE (SIMPLE and PISO combined) algorithm implemented in OpenFOAM, using with one outer correction, which acts like de PISO scheme, having two corrections at each time step. The under-relaxation factors that are required to input for the algorithm are: for pressure, 0.5; momentum, 0.5; energy, 0.9; turbulent kinetic energy and specific dissipation rate: 0.6.

  As a reference diagram of the PIMPLE scheme is shown in Figure 3.3. At a given time step, the volume fraction equation is solved, update density (e.g. ideal gas law for air) followed by momentum; then the energy equation is solved. After this step, the pressure correction is made (where the 2 inner iterations are made), and finally the turbulence equations are solved (in the example in Figure 3.3, other models are updated and solved). Since there is one outer correction, the solution advances to the next time step. The small time step and Co number ensures stability during the simulations.

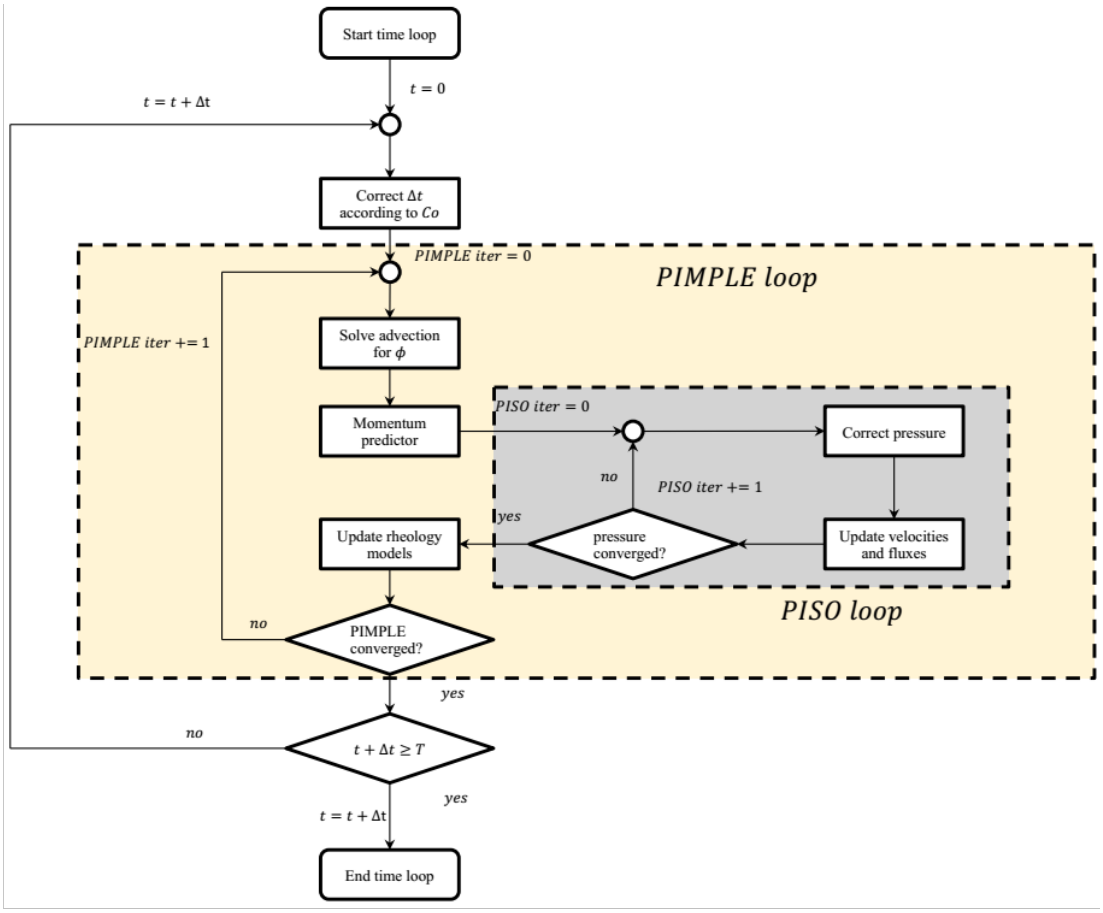

Figure 3.3: Flowchart for the PIMPLE Algorithm in OpenFOAM (Municchia et al. [37]). In this flowchart T is the simulation time and ϕ is a scalar that is advected.

- The interface tracking is solved explicitly, using the Multidimensional Universal Limiter with Explicit Solution (MULES) used in OpenFOAM (OpenFOAM [38]). The MULES is an iterative scheme that includes a weighted solution with and without the compression term in equation 2.53, using a limiter that is used to bound the solution. This method has shown excellent results in describing the interface with different shapes when advection is present (Desphande et al. [16]). The tolerance used to solve the VOF equation, using the MULES scheme, is 1e-9, using two corrections at each time step.

- For the VOF, velocity, energy, k and ω equations, the well known Gauss-Seidel elimination is used. The tolerance used in the method is 1e-10.

- Pressure equation is solved with a Preconditioned Conjugate Gradient, using a Diagonal-based Incomplete Cholesky. This method has been proven to be more stable than using a Gauss-Seidel elimination method. The tolerance used here is 1e-6.

3.3. Case Definition

Table 3.1 shows the case definition. The case labeled SJ corresponds to a single tuyere configuration, operating under a jet regime (Mori et al. [36] and Aoki [3]), with a Nozzle Pressure Ratio, NPR, that is NPR=7.3, and with a theoretical tuyere-exit-to-hydrostatic-pressure ratio, $\eta_{e,th} = p_e/p_b$, that is $\eta_{e,th}$=3 (p_e is the tuyere exit pressure). With these parameters, underexpansion is expected to avoid back-attack effects (Gulawani [25], Miaosheng et al. [34]). This case corresponds to a representation of the Loth & Faeth [32] experiment for d=11 mm and $\eta_{e,th}$ =3, where pressure data, obtained with Pitot probes, is available for comparison and validation of this case.

Table 3.1: Case Definition. Configuration is indicated. Values for interspace, s/d, NPR and $\eta_{e,th} = p_e/p_b$ are shown.

Case	Configuration	s/d	NPR	$\eta_{e,th}$
SJ	Single Jet	-	7.3	3
TJ1.15	Twin Jet	1.15	7.3	3
TJ1.8	Twin Jet	1.8	7.3	3
SJ-eq	Single, Twin equivalent	-	5.5	1.65

The case labeled TJ1.15 corresponds to the twin jet injection with an interspace of s/d=1.15. Case TJ1.8 represents the twin tuyere setup with s/d=1.8. In these cases, the same values of NPR and $\eta_{e,th}$ in case SJ are used.

The case labeled SJ-eq represents a single tuyere that is area-equivalent to a twin tuyere configuration, i.e. it has a cross-section area equal to twice the tuyere area in case SJ. Then, the equivalent diameter is d_{eq}/d=$\sqrt{2}$. The NPR and $\eta_{e,th}$ values in the SJ-eq case are also computed, using one-dimensional equations (Fanno flow) followed by small adjustments that are made to match the total mass flow rate obtained in cases TJ1.15 and TJ1.8.

The simulations are run in the NLHPC facilities, using 40 nodes, and using preliminary test runs, it is estimated that each simulation takes about 50 to 60 days to obtain around 140 to 180 ms of evolution, which according to the literature reviewed in Chapter 1 is enough to obtain a submerged jet structure (that is, within the inertial range).

Chapter 4

Results and Discussion

4.1. Grid Sensitivity

A grid sensitivity analysis is made, using mesh sizes, N_g, (with g=3,2,1) that are: coarse, with N_3=2.1, medium, with N_2=2.6 and a fine grid, with N_1=3.77 million elements. The solver *compressibleInterfoam* is used in a single phase (air-to-air) simulation of a single tuyere into an initially quiescent air in the tank, with the same boundary and initial conditions defined for Case SJ. The main modifications of grid size correspond to both cell size and growth ratio inside the tuyere and cylindrical block used for refinement. In general, the grid growth rate is 1.3 between the coarse and medium meshes, and 1.4 between the medium and fine meshes. The runs are made in the NLHPC facilities, using 40 nodes, each run taking between 5 to 10 days to obtain a developed jet with its structure not varying over time.

A single phase simulation and sensitivity is performed to evaluate the solver ability to capture the jet structure which, according to experiments (Aoki [3], Loth & Faeth [32]), is similar to that found in air-water injection. Furthermore, within the jet core the greatest fluctuations in flow variables can be found, and thus the grid size will have an effect mainly in the distribution of shock cells and the definition of velocity change in the regions between a pair of cells. As a contrast, Making a sensibility analysis for the grid size for the VOF model, the grid size will have an effect only on the air-water interface spatial resolution. However, diffusion effects are taken into account through the compressive formulation and numerical scheme MULES. Thus, the significant flow feature is the air jet and its characteristics.

Figure 4.1 shows Mach and pressure profiles along a centerline. No significant change is observed in typical instantaneous profiles for $x_c/d > 0$. Some differences are found inside the tuyere for the fine grid (i.e. for $x_c/d < 0$), but have little impact in the profile for $x_c/d > 0$. In this region, the main differences in the mesh sizes are observed in the number of points used to resolve the typical sinusoidal pattern of underexpanded single-phase flow

related to the presence of shockwaves.

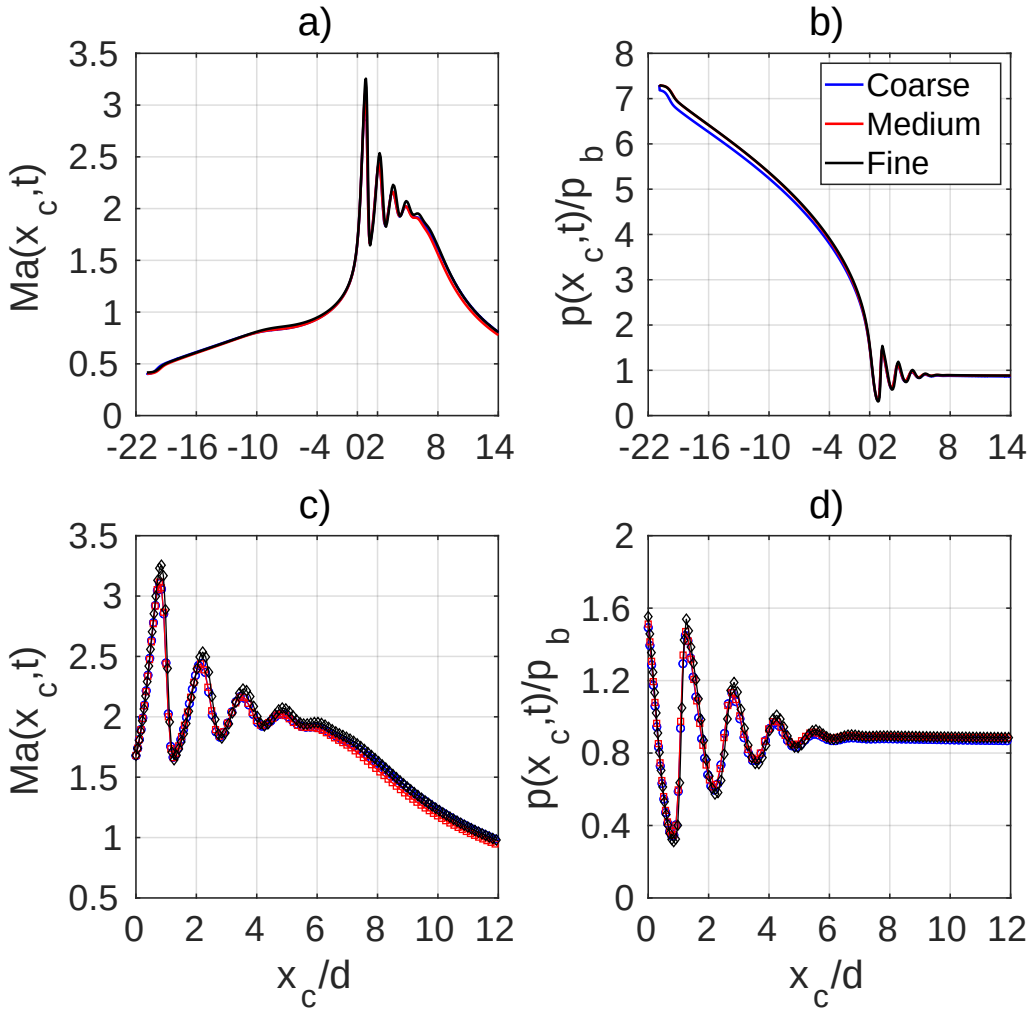

Figure 4.1: Grid sensitivity instantaneous profiles, for a single-phase (air-air) injection at $t^e = tu_e/d$=564.1: a) Mach for -21< x_c/d <14, b) Pressure for -21< x_c/d <14, c) Mach, enlarged for 0< x_c/d <12, d)Pressure, enlarged for 0< x_c/d <12.

Figures 4.2 and 4.3 show, respectively, Mach and pressure profiles in the y-direction for all grid sizes and for different axial positions at the same instants as in the axial profiles. It is shown that the grid sizes are such that in all streamwise positions the differences are found near the maximum velocity and minimum pressure locations for $x/d \leq$2. All grids seem to converge quickly between sizes. This is more evident for positions x/d=6 and x/d=12, where already for the medium grid the profiles converge, and the fine grid is different only in the positions of shockwave reflection, but without a considerable change in the jet width.

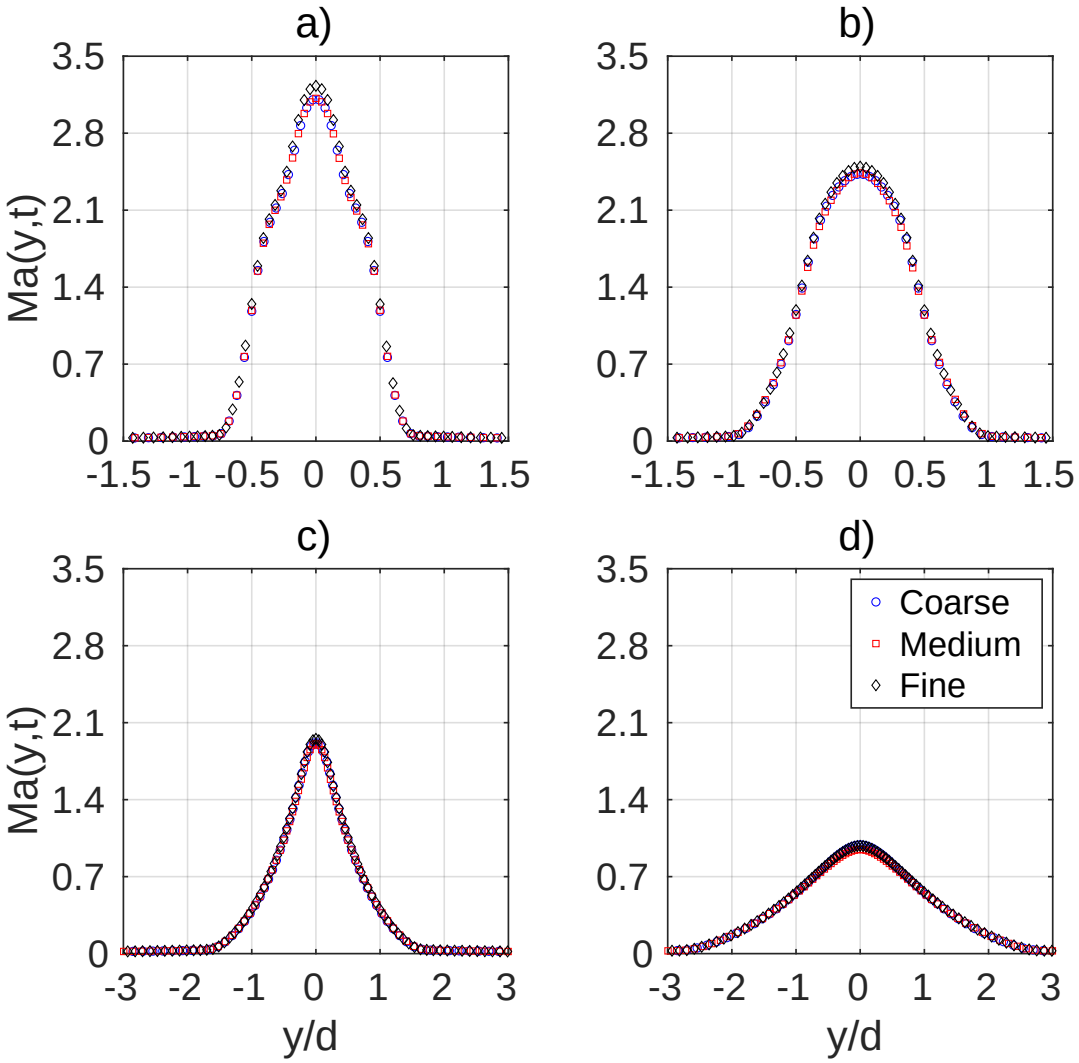

Figure 4.2: Grid sensitivity of Mach profiles, for $0< y/d <12$, for a single-phase (air-air) injection at $t^e = tu_e/d$=564.1, time at which the profile does not vary over time: a) x/d=0.8, b) x/d=2, c) x/d=6, d) x/d=12.

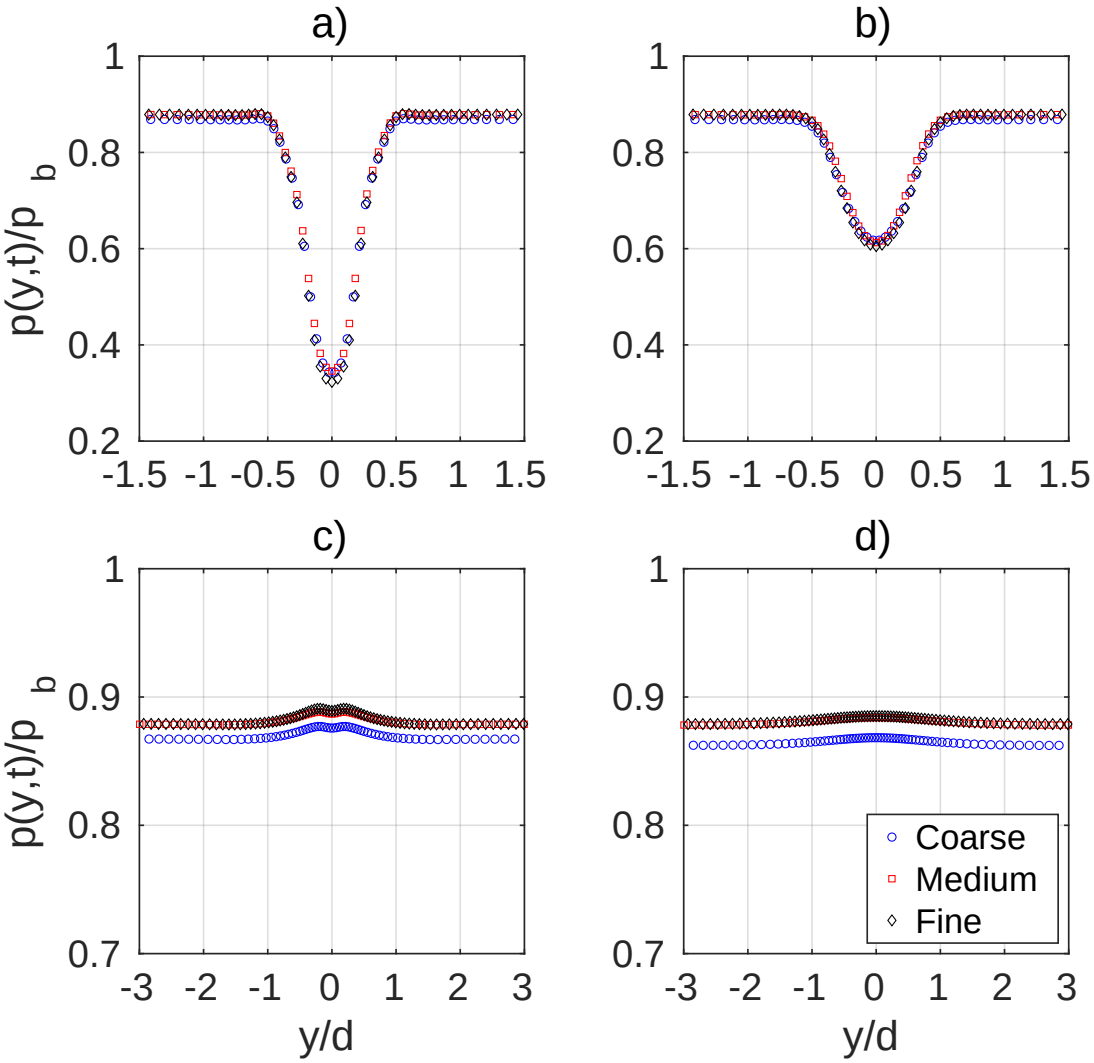

Figure 4.3: Grid sensitivity of pressure profiles, for $0< y/d <12$, for a single-phase (air-air) injection at $t^e = tu_e/d$=564.1, time at which the profile does not vary over time: a) x/d=0.8, b) x/d=2, c) x/d=6, d) x/d=12.

The method by Celik et al. [12] is applied to obtain the relative difference between grids and to have a measure of the Grid Convergence Index, GCI, although it is important to notice that there are several positions where difference between values obtained in different grids, are "close to zero", as observed by the authors, and therefore the method might not be representative at such locations. The analysis can be done, however, for maximum Mach number and minimum pressure, but where the apparent order shows to be greater than the scheme order.

Following the procedure of grid analysis, it is found that GCI=10.9% for the minimum pressure at x/d=0.8, GCI=1.7% for the maximum Mach values, both obtained between the medium and fine grids, and where the relative difference of maximum Mach number, between the coarse and medium meshes, are e_{32}=0.39%, and e_{21}=3.56%, respectively. For minimum pressure this relative differences are e_{32}=1.49%, and e_{21}=4.52%

This above shows that there is about 3.5 and 4.5% improvement in the maximum velocity and minimum pressure can be obtained, respectively, with the finer grid with respect to the medium grid, with about 40% more in cell count. In addition, the computation (wall-clock) time for the fine grid size is found to be about 60% larger between time steps as compared to the medium grid size. Thus the increase in accuracy shows a small improvement with respect to the computational cost.

Therefore, given the results of grid analysis and assessing the computational costs, the medium sized grid with 2.6 million elements will be used as it shows good representation of the first shock cell and general jet structure.

4.2. Time Evolution

The simulation results are analyzed as a function of the normalized time $t^e = tu_e/d$, using the exit velocity, u_e, and tuyere diameter, d. This normalized time has been used in the work by Tang et al. [52] and represents time units of large scales, particularly the typical core size in the submerged jet. Other works (Gong et al. [24],Miaosheng et al. [34]) use time units in seconds to describe the submerged jet. However, the time description is only used to analyze the submerged jet evolution which then sets the basis for statistical description of the flow.

Figure 4.4 shows, for all cases, the area-weighted average, denoted as $< . >_A$, of Mach number, Ma, normalized static pressure, p/p_b, as a function of time $t^e = tu_e/d$, at the tuyeres exit plane at x/d=0. In case SJ, the acceleration and decrease in pressure between $0< t^e <50$ are followed by an approximate flat profiles related to the first bubble growth, extending up to $t^e \approx$1300, when bubble detachment occurs. For $t^e >$1300, fluctuations of these flow variables are observed, noticing that time-average of $< p >_A /p_b$ is 2.1, while for $< Ma >_A$ is 1.05.

Figure 4.5 shows, for all cases, the area-weighted average of temperature $< T/T_{in} >_A$, and density, ρ/ρ_{in} as a function of time $t^e = tu_e/d$, at the tuyeres exit plane at x/d=0, where T_{in} and ρ_{in} are the total temperature and density at the tuyere inlet, respectively. The profile shows a decrease in temperature and density at the tuyere exit plane, and then shows large fluctuations that follow the pressure behavior accordingly because of flow compressibility. From this profile, the time-averaged exit temperature is T/T_{in}=0.78 for

Cases SJ, TJ1.15 and TJ1.8, and T/T_{in}=0.5 for Case SJ-eq. The time-averaged density is ρ/ρ_{in}=0.34 for Cases SJ, TJ1.15 and TJ1.8, and ρ/ρ_{in}=0.47 for Case SJ-eq.

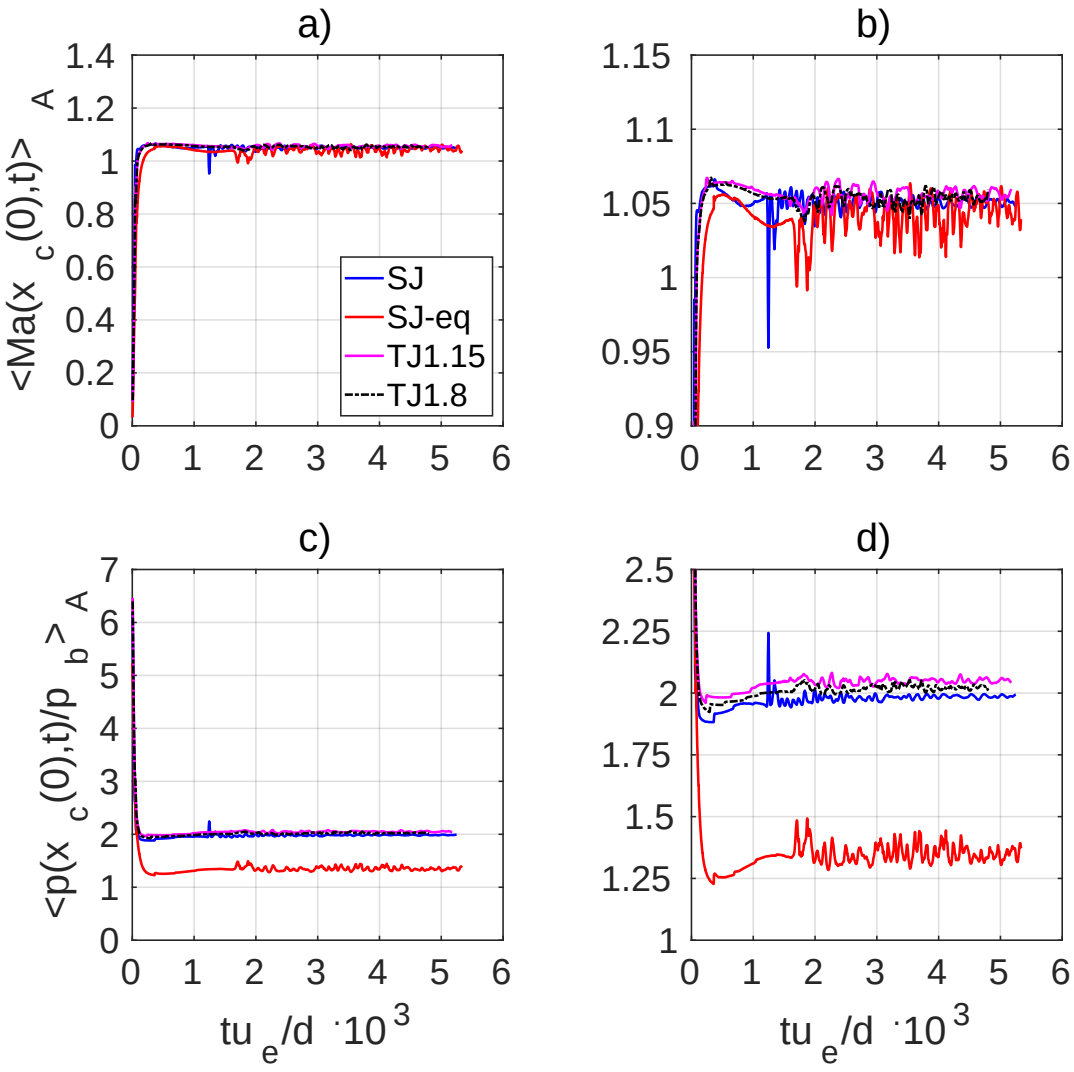

Figure 4.4: Area-weighted average at tuyere exit, x_c/d=0, as a function of time, in units of u_e/d, of: a) Temperature, $< Ma(x_c(0),t) >_A$, b) Enlargement of $< Ma(x_c(0),t) >_A$ b) Pressure, $< p(x_c(0),t)/p_b >_A$, d) Enlargement of $< p(x_c(0),t)/p_b >_A$. Here u_e the average exit velocity, at the indicated tuyeres exit plane located at x_c/d=0 (with x_c the centerline coordinate), and computed as $u_e =< Ma >_A \sqrt{\gamma R_1 < T >_A}$, with $< T >_A$ is the time-average exit air temperature.

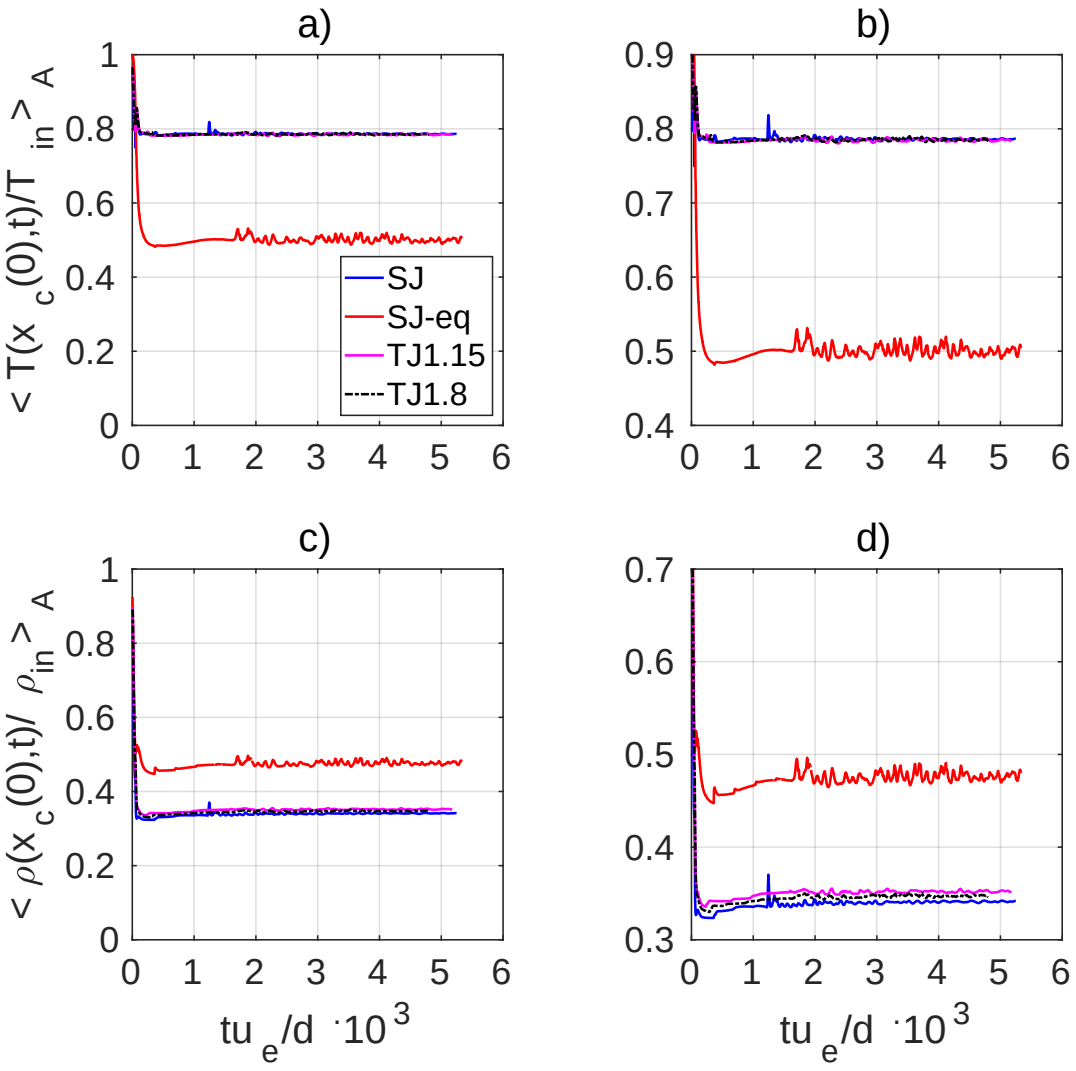

Figure 4.5: Area-weighted average at tuyere exit, x_c/d=0, as a function of time, in units of u_e/d, of: a) Temperature, $< T/T_{in} >_A$, b) Enlargement of $< T/T_{in} >_A$ b) Density, ρ/ρ_{in}, d) Enlargement of ρ/ρ_{in}.

Cases TJ1.15 and TJ1.8 show a similar signal in all variables, where effects of detachment are not clearly observed, but fluctuations are still present. In case SJ-eq, a behavior similar to case SJ is seen before the first bubble detachment. This happens at $tu_e/d \approx$1600, since larger mass flow rate is injected and bubble volume, before detachment, is also larger. After this event, substantial fluctuations are observed as compared to the rest of the cases, which is a direct effect of the lower underexpansion level in this case.

Figure 4.6 shows, for all cases, a 3D representation of the axial velocity profile, $u(x_c,t)/u_e$ as a function of time, t^e, for $0 \leq x/d \leq 15$. It is clear that in during the

initial bubble growth, the flow has the typical sinusoidal profile observed in underexpanded air jets. These profiles start to fluctuate as the jet develops after the first bubble detachment, where its main characteristic is an irregular sinusoidal profile indicating that a distorted cell arrangement is obtained in the flow.

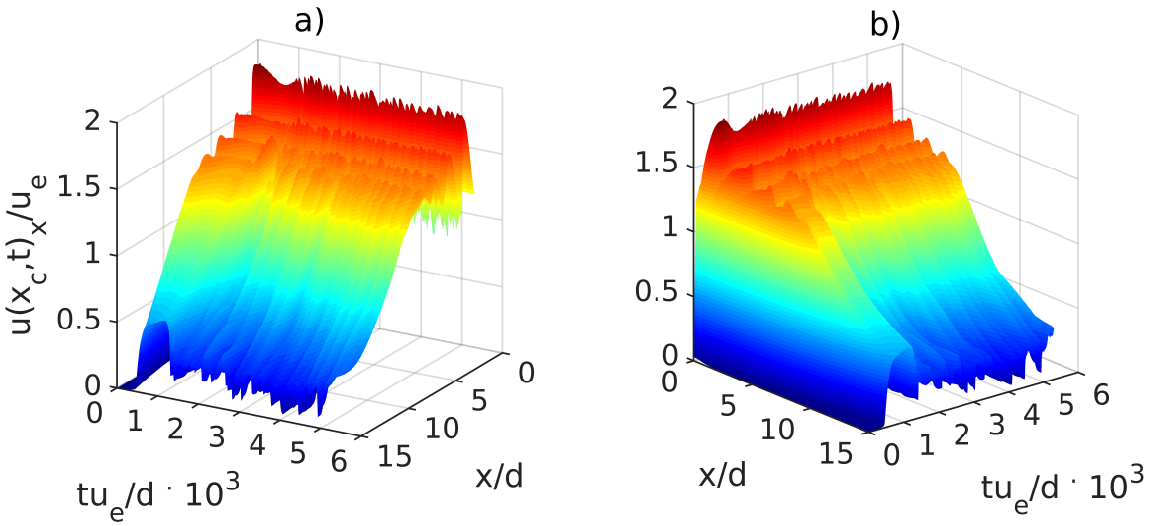

Figure 4.6: Time evolution of axial velocity profile, $u(x_c, t)/u_e$,as a function of time, t^e, for $0 \leq x/d \leq 15$: a) view from reversed time, b) general view.

4.3. Flow Visualization

In general, the flow with single and twin tuyeres configurations can be described by an initial ellipsoidal bubble growth, as shown for Case SJ in Figure 4.7, with its major axis in the streamwise direction (Kyriakides et al. [30]). This elongated bubble then detaches from the tuyere at a characteristic time, obtained from equating buoyancy and inertia, when the distance to the tuyere exit equals half the bubble length (Anagbo et al. [1]). After this instant, a continuous air flow starts to develop, characterized by air-water interaction events (e.g. bulging, necking) that alternate in time. This is represented in Figure 4.14, showing typical air volume fraction and Mach number contours in the xy-plane for z/d=0, for two instants.

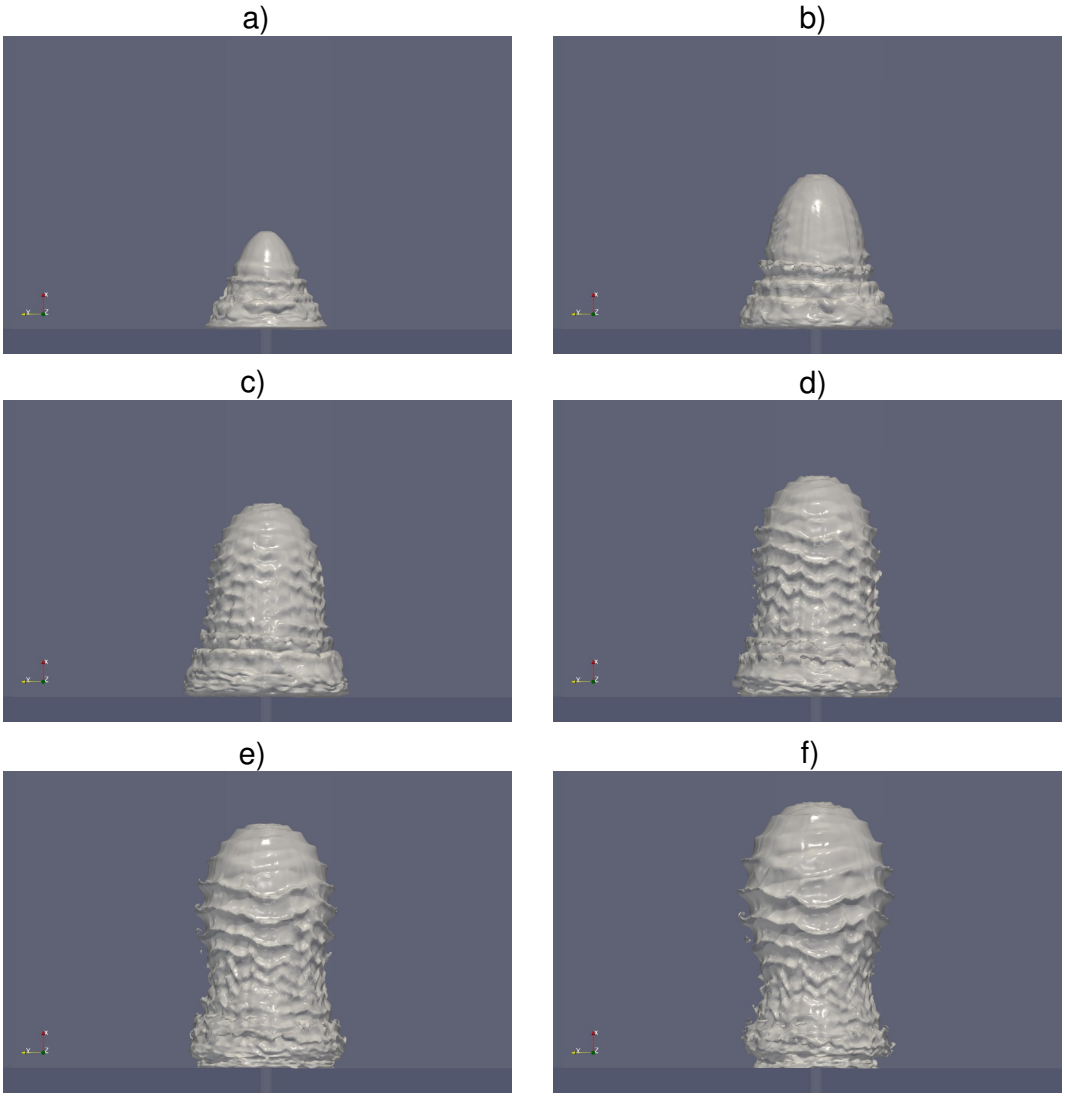

Figure 4.7: Initial Isosurfaces of α=0.5 for Case SJ, as a typical reference. The remaining cases show similar behavior. The instants shown from a) through f) correspond, respectively, between t^e= 133 and t^e= 798, with time steps of Δt^e= 133.

Figures 4.8 to 4.13 show contours of α of water volume fraction α, Mach Ma, temperature $T/T0$ and pressure p/pb between times t^e= 133 and t^e= 798. It is seen that the jet develops following a typical underexpanded air jet at t^e=133 , where an increase in velocity is observed at instants t^e=266 and t^e=399 as the bubble expands in the axial and radial directions. When the contraction effect starts (as buoyancy equates inertia) near the time t^e=532, prior to detachment, the velocity starts to decrease, as seen between times t^e=665 and t^e=798. The rest of the variables show an analog behavior.

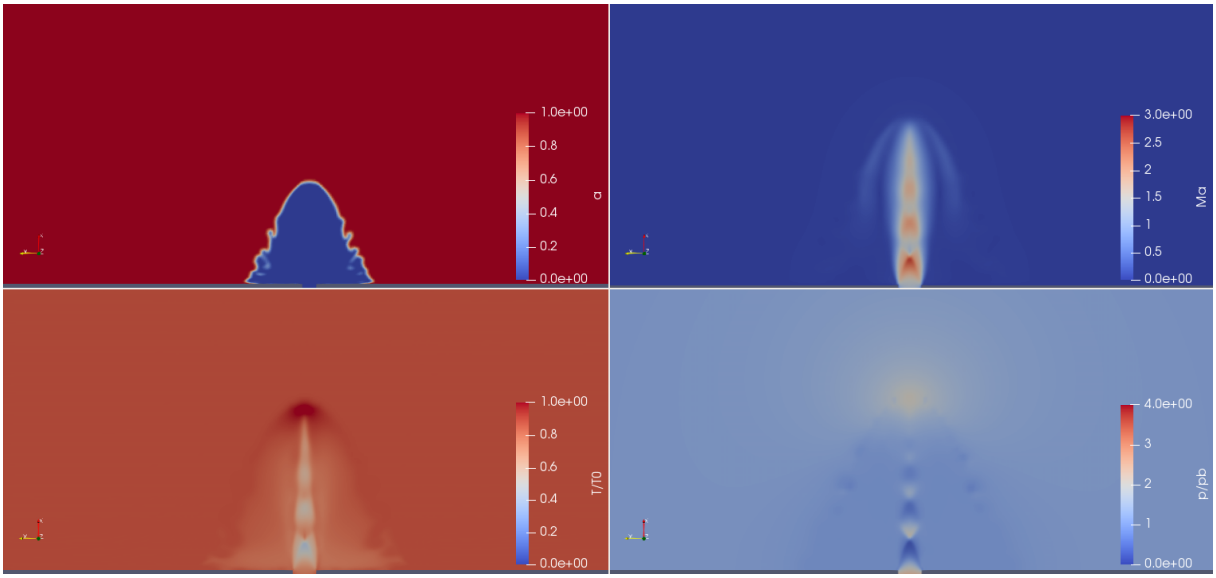

Figure 4.8: Contours of α, Ma, T/T_0 and p/pb for Case SJ at time t^e= 133. (Raw ouput data from OpenFOAM).

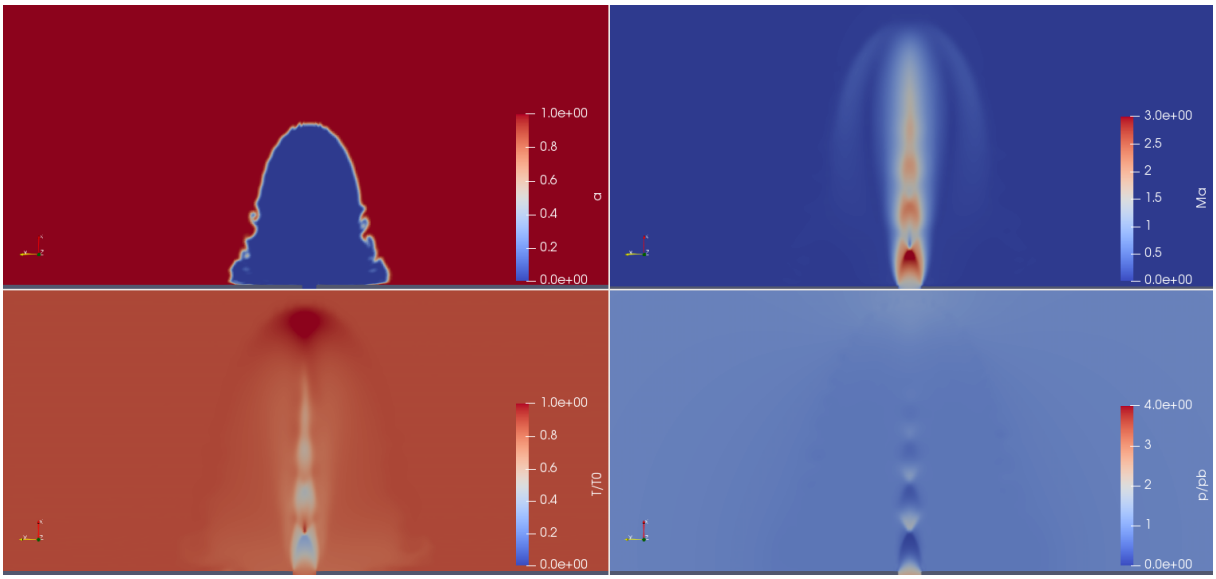

Figure 4.9: Contours of α, Ma, T/T_0 and p/pb for Case SJ at time t^e= 266. (Raw ouput data from OpenFOAM).

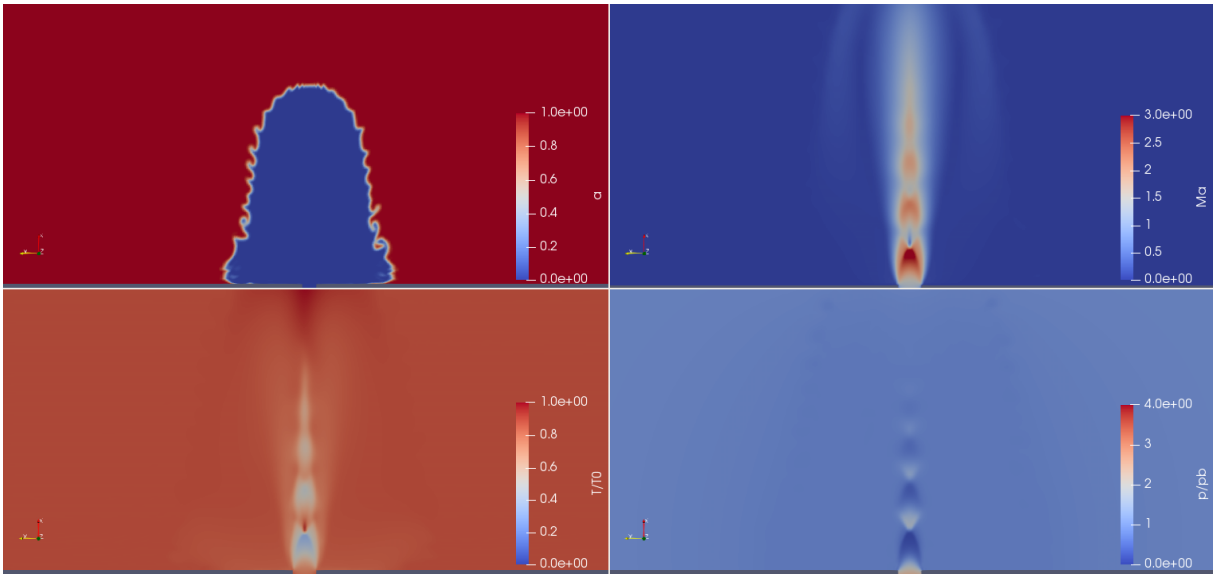

Figure 4.10: Contours of α, Ma, T/T_0 and p/pb for Case SJ at time t^e= 399. (Raw ouput data from OpenFOAM).

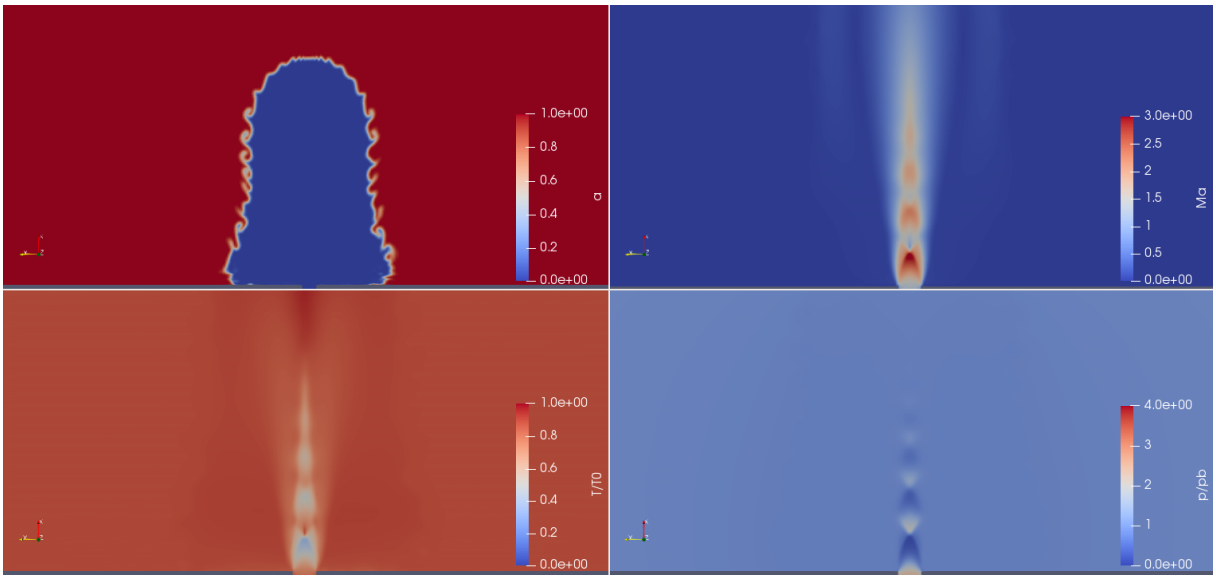

Figure 4.11: Contours of α, Ma, T/T_0 and p/pb for Case SJ at time t^e= 532. (Raw ouput data from OpenFOAM).

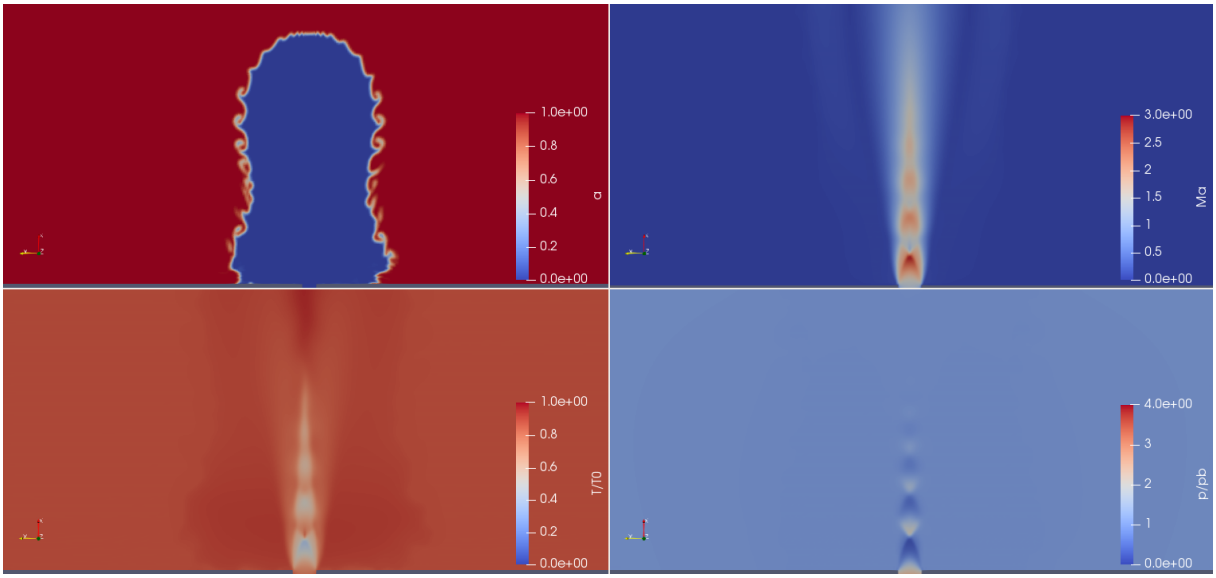

Figure 4.12: Contours of α, Ma, T/T_0 and p/pb for Case SJ at time t^e= 665. (Raw ouput data from OpenFOAM).

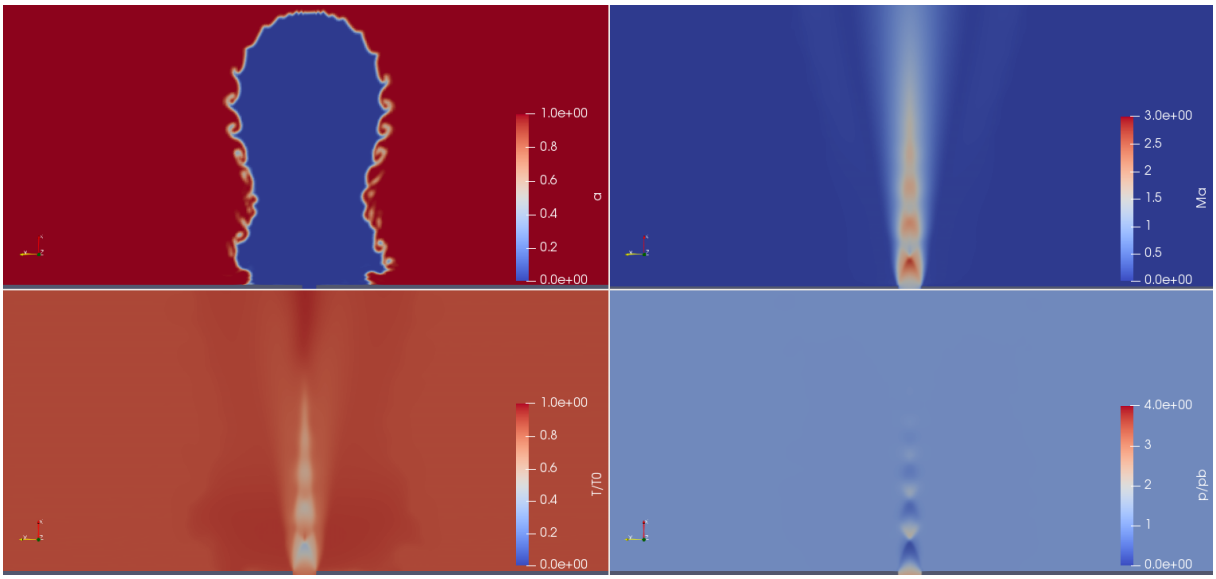

Figure 4.13: Contours of α, Ma, T/T_0 and p/pb at for Case SJ time t^e= 798. (Raw ouput data from OpenFOAM).

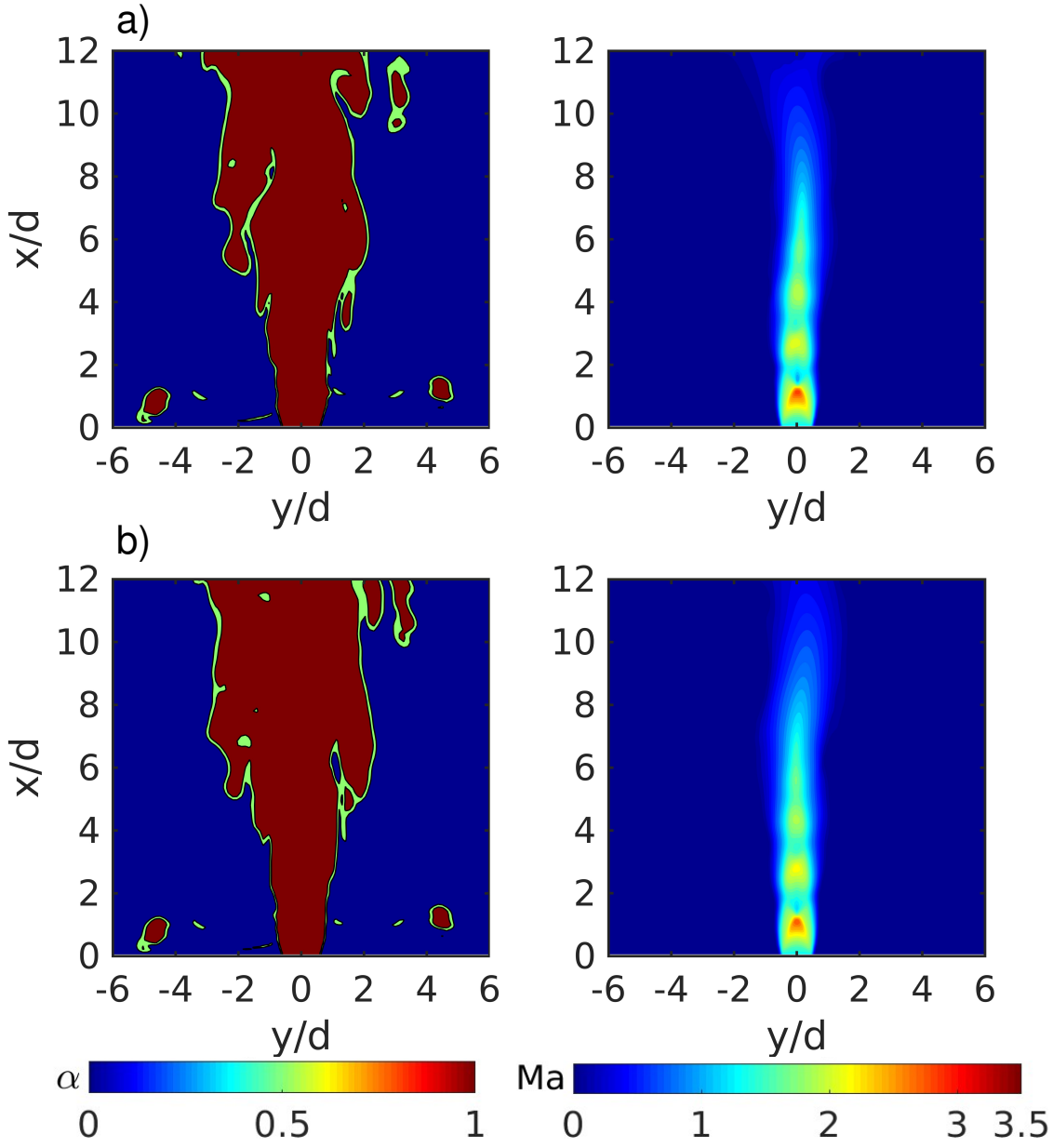

Figure 4.14: Contours of air volume fraction, α (left column) and Mach, Ma, (right column) for Case SJ: a) t^e= 3404, b) t^e= 3471. (Raw ouput data from OpenFOAM).

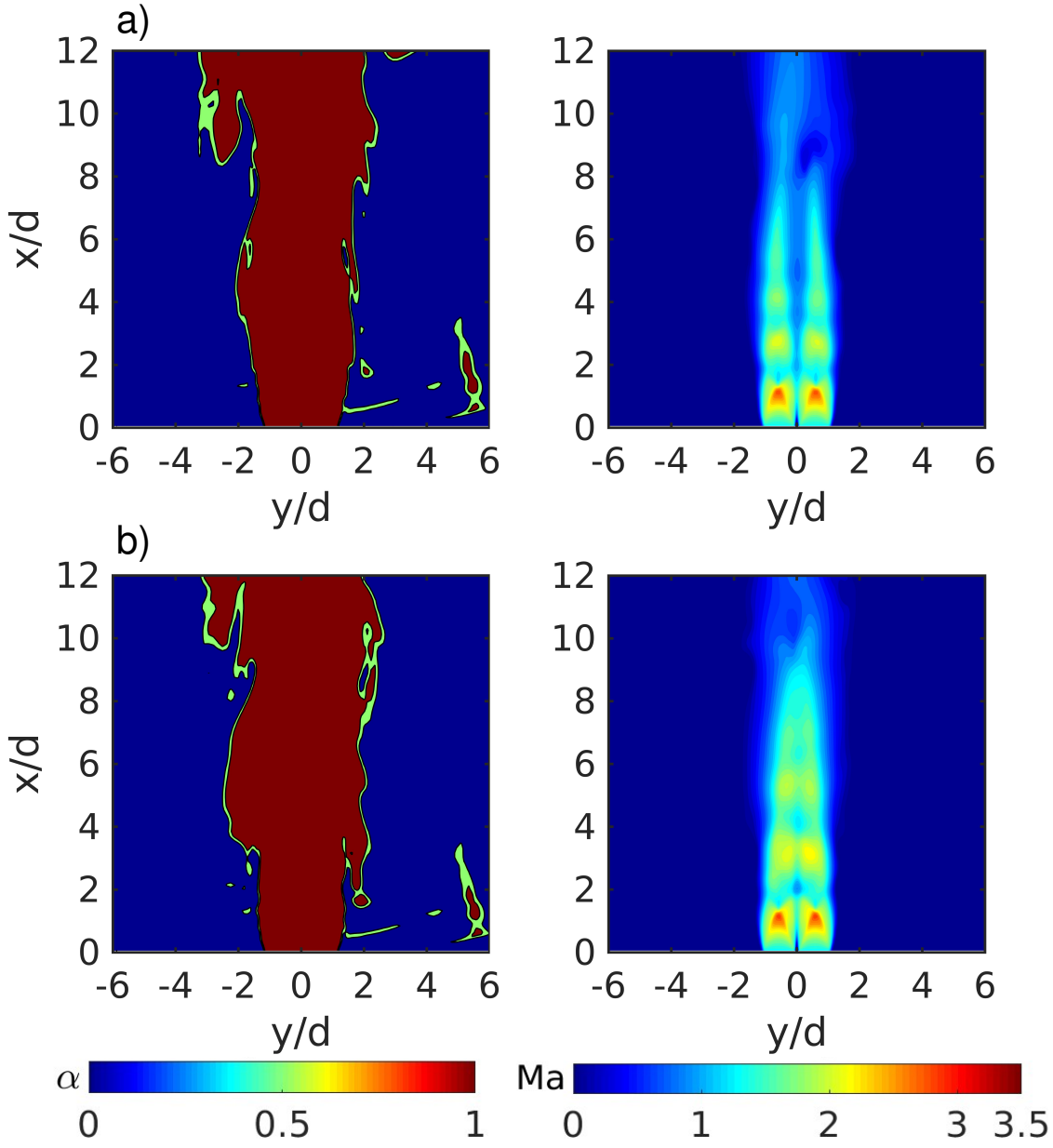

Figure 4.15: Contours of air volume fraction, α (left column) and Mach, Ma, (right column) for Case TJ1.15: a) t^e= 4426, b) t^e= 4473. This configuration shows an example of a symmetric (flapping) mode.

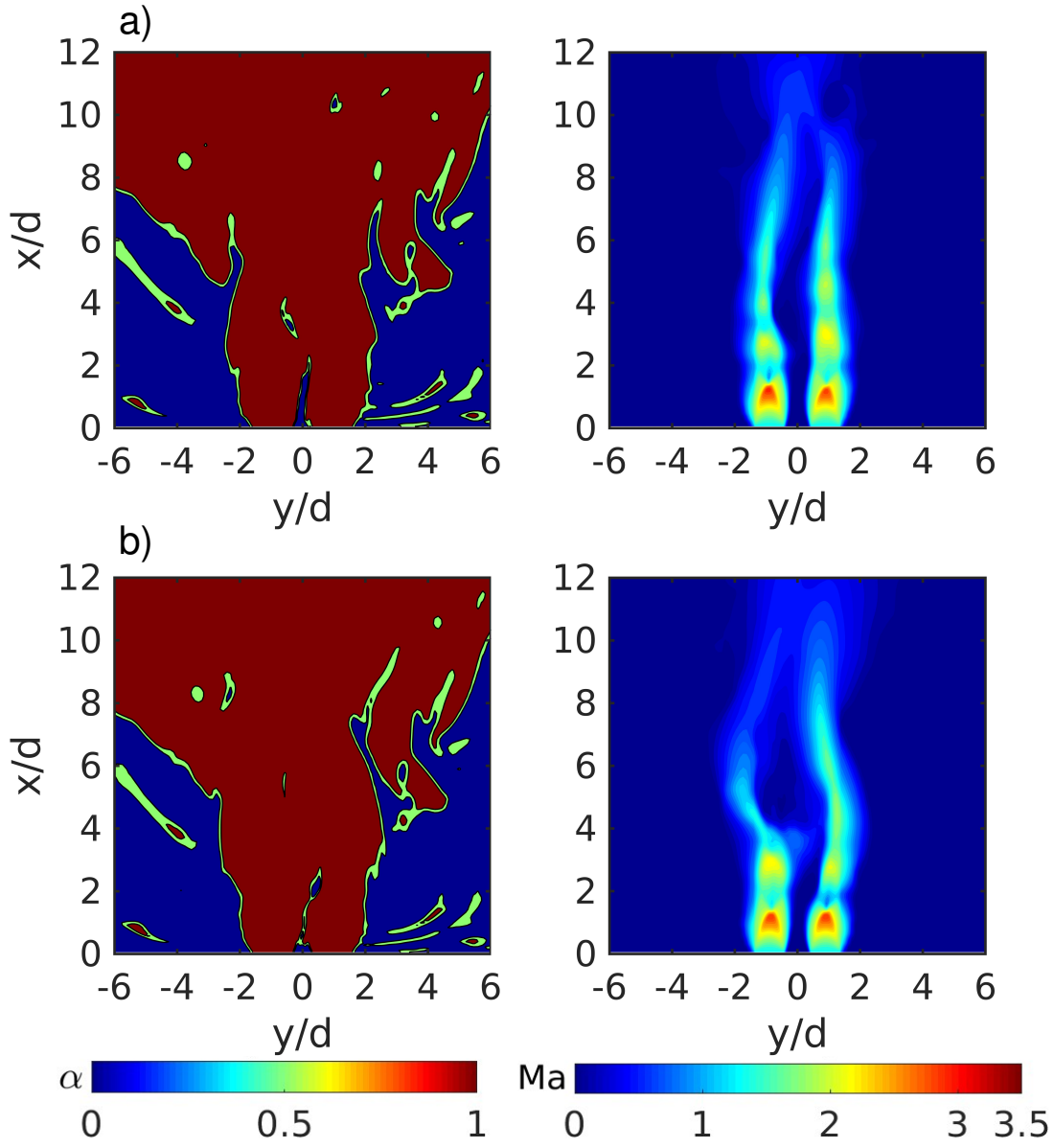

Figure 4.16: Contours of air volume fraction, α (left column) and Mach, Ma, (right column) for Case TJ1.8: a) t^e= 3889, b) t^e= 3955. This configuration shows an example of an asymmetric (waving) mode.

In case SJ, shown in Figure 4.14, the shock cell arrangement is slightly distorted, specially near the instantaneous potential core "tip", where cells change in size, "vibrating", a result also reported by Gong et al. [24]. In particular, the first shock cell has a length and width that vary strongly in time as it passes from the x-shaped to other type of shockwave structures, mainly due to air-water interface deformation. Given the injection conditions in case SJ and, similarly to what was observed by Miaosheng et al. [34] and Miao et al. [33], bulging and necking frequencies drop, and are observed here as rather

small deformations of the interface as compared to those present downstream the point where the potential core ends.

In case TJ1.15, shown Figure 4.15, jets show symmetric (flapping) and asymmetric (waving) modes, where the latter seems predominant over the former. In addition, larger cell size variation in the streamwise direction is obtained, particularly in the first cell of each jet. Furthermore, cell structure indicates that, at given instants, shockwaves cross-reflection from each jet is present, and also that potential cores seem to be deflected towards each other. Moreover, it is observed that relevant underwater twin jet motion happens predominantly in the xy-plane, rather than in the yz- and xz-planes. This observation, discussed further in this section, is also found in the single-phase twin jet experiments of Raman & Taghavi [44] and Knast et al. [29]. It is important to notice that the denominations of "waving" and "flapping" modes from these authors are used here only as a name reference, since the source of such behavior is based on sound interaction, while for the submerged jets it is suspected that interaction rather comes from air-water interface effects.

A different flow field is obtained in case TJ1.8, shown in Figure 4.16, where the asymmetric mode is predominant. Air-water interface of each jet interact, strongly influencing the individual shock cell structure where, at an instant, the first two cells remain in one of the tuyere exit and in the other, a typical cell arrangement can still be observed, although visibly distorted. This indicates that larger tuyere separation produces a strong variation in the core's length and it is expected to produce a greater mixing rate as compared to case TJ1.15, particularly in the tuyeres interspace.

Figure 4.17 shows isosurfaces of α=0.5 and Ma=1 at different instants for cases SJ, TJ1.15 and TJ1.8. For all these cases, the instant t^e= 133 shows the initial elongated bubble and potential cores. It is clear that in case TJ1.15 cores are combined, while for case TJ1.8, they are separated. At t^e= 798 and t^e= 929, for case SJ, the typical interface deformation is shown, which is related to the KH instabilities. In addition, the potential core seems to maintain its position, varying its length mainly in the x-direction. In case TJ1.15 a clear variation of the combined potential cores in the x-direction is shown; and in case JT1.8, the waving of individual potential cores are observed. Moreover, close to the bottom tank wall, the α isosurfaces indicate presence of air which in experiments (Miao et al. [33]) is observed as bubbles remaining that position, possibly due to recirculation patterns of the surrounding water.

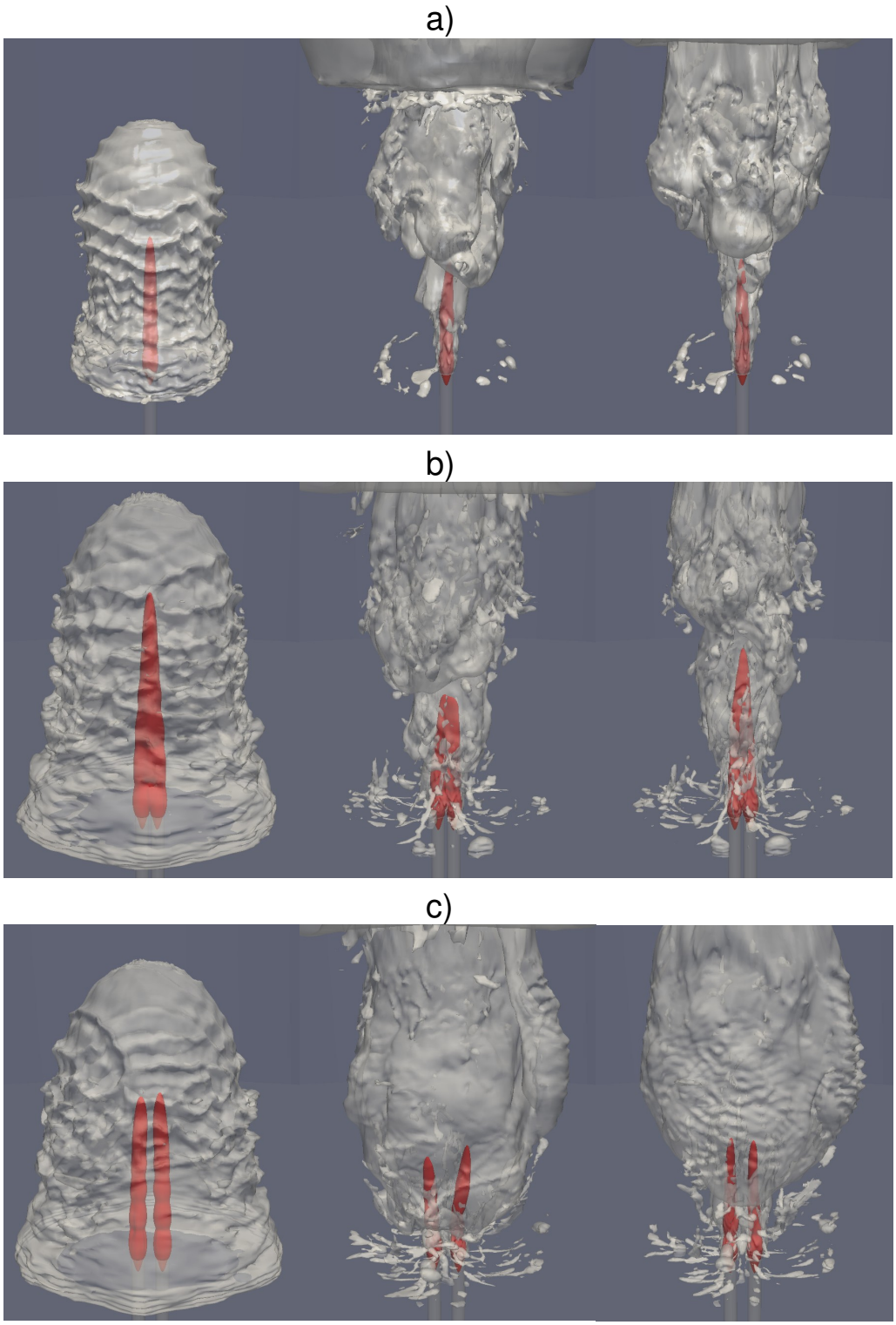

Figure 4.17: Isosurfaces of α=0.5 and Ma=1 (in red) for: a) Case SJ, b) Case TJ1.15 and c) Case TJ1.8. The instants shown correspond, from left to right: t^e= 133, 798 and 929.

4.4. Statistical Profiles

Time-average and root mean square (rms) of velocity and pressure are used to analyze profiles. The time-average of a quantity $\phi(x,t)$ is $< \phi(x,t) >_t = \frac{1}{N}\sum_{i=1}^{N}\phi(x,t_i)$, and rms is computed as $[\phi(x,t)]^2_{rms} = \frac{1}{N^2}\sum_{i=1}^{N}(\phi(x,t_i) - < \phi(x,t) >_t)^2$, where N is the number of data samples, with $N \to \infty$. The statistics are obtained in the window defined by -20.9$< x/d <$14, -10$< y/d <$10 and -10$< z/d <$10, where they converge after the instant t^e=2655.

The number of data analyzed is N=300 to N=350, and each are stored at the time step Δt^e=6.636. Within this window, different lines are created: 1) centerlines: straight lines that correspond to the tuyeres axis and 2) *flow-centerlines*: inclined lines, following a resulting average jet inclination.

4.4.1. Single Jet Validation

Figures 4.18 a) and b) show, for case SJ, the time-average profiles of Mach number, with $Ma = u/\sqrt{\gamma R T_1}$, and normalized pressure in the axial direction, x_c respectively.

Inside the tuyere, for $x_c/d <$0, typical non-linear velocity increase and pressure decrease are found. Outside the tuyere, for 0$< x_c/d <$14, the profile of $< p >_t / p_b$ shows a sinusoidal behavior, consistent with the presence of shock cells in the underwater jet structure. Pressure data from the Loth & Faeth [32] experiment is plotted in Figure 4.18 to validate case SJ. The time-average of normalized pressure profile shows good agreement with the experimental data for 0$< x_c/d <$5, whereas for $x_c/d >$5 results underpredict pressure values. Also, the average cell structure seems to be shorter than the obtained in experiments, indicating that the core length might be underpredicted as well. This is a limitation of URANS turbulence models related to cells damping effects (Birkby & Page [6]). With this in mind, the potential core length can be estimated from the profile for $< Ma(x_c,t) >_t$, shown in Figure 4.18 a), using the definition of Franquet et al. [22], i.e. the point in the axial direction where flow becomes subsonic and turbulent layers merge. Thus, the core length is L_p/d=8, which is about 30% of the inertial length scale (for details of this scale, see Harby et al. [26]).

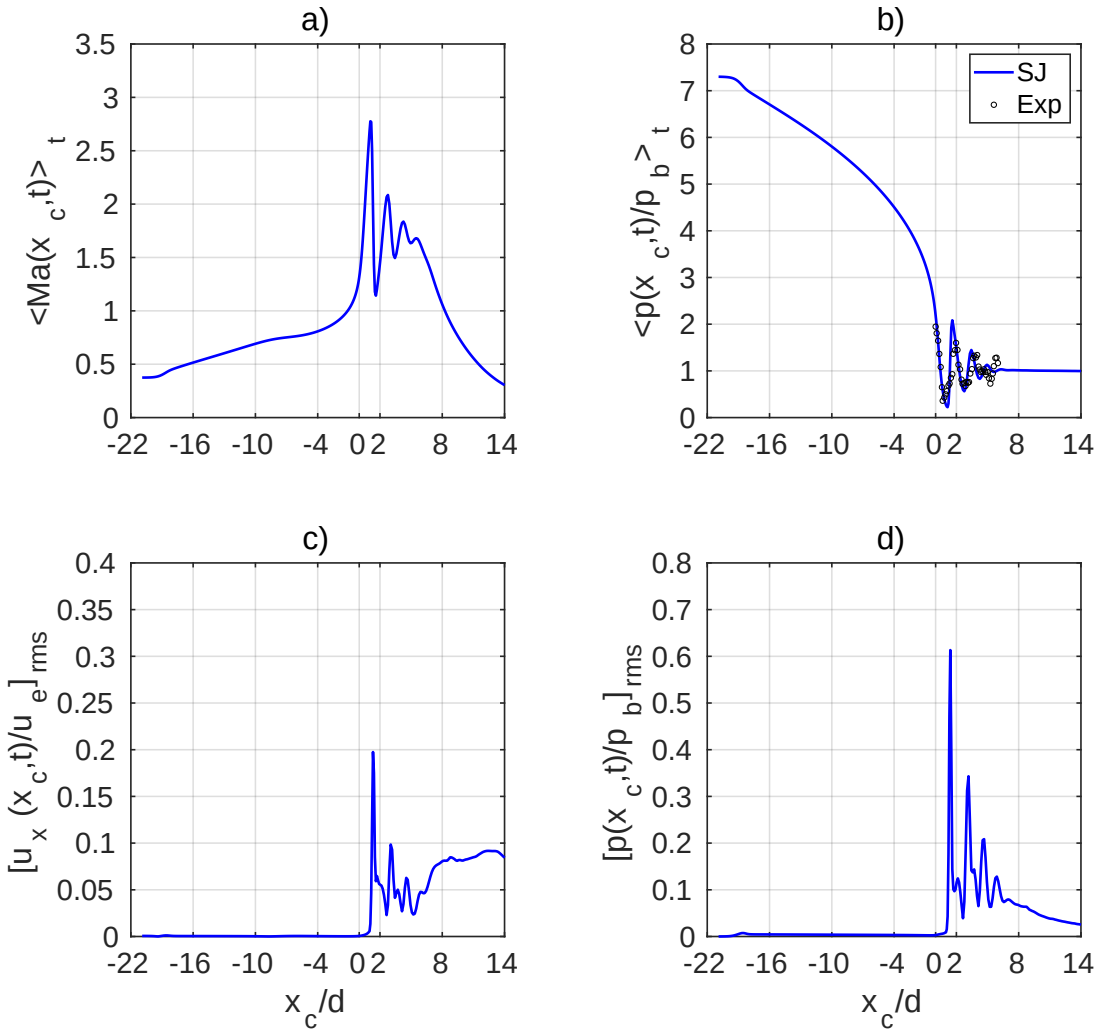

Figure 4.18: Case SJ. Time-averaged profiles of :a) Mach; b) Pressure. Rms profiles: c) Normalized streamwise velocity, and d) normalized pressure. The dots on top of the pressure profile correspond to the pressure data from Loth & Faeth [32]. The centerline is x_c, defined where y=0 and z=0 for all x_c.

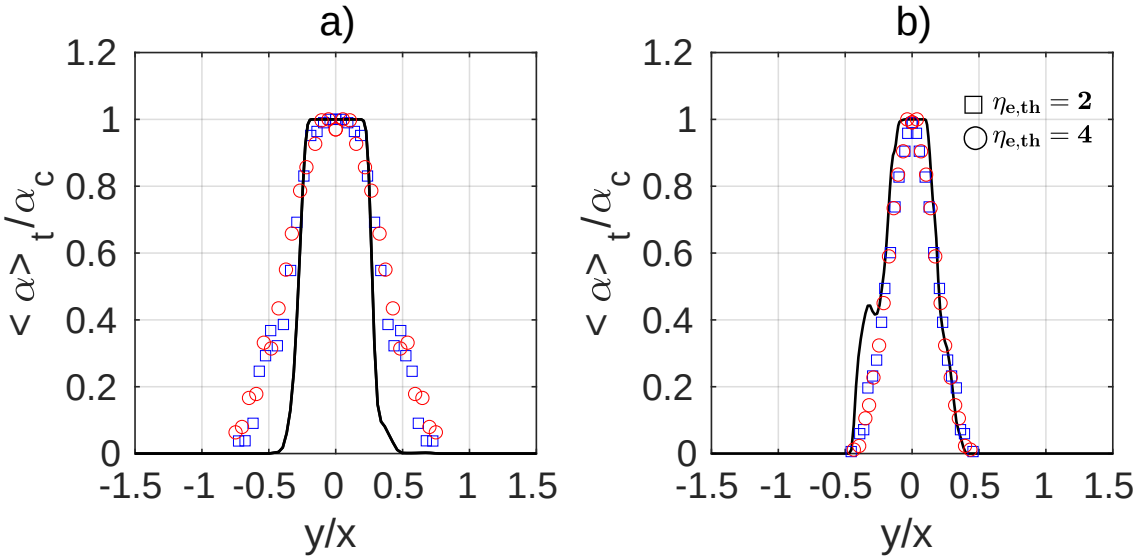

Figure 4.19: Case SJ. Time-averaged profiles of air volume fraction, normalized by the centerline value, α_c, at positions:a) x/d=4 and b) x/d=8. As a reference, experimental data (mirrored here for display purposes) from Loth & Faeth [32] is plotted for $\eta_{e,th}$=2 and $\eta_{e,th}$=4. Thus, case SJ can be representative of $\eta_{e,th}$=3, for -0.5< y/x <0.5.

Figures 4.18 c) and d) show, respectively, the normalized rms profiles of streamwise velocity, u_x, and pressure, p, in the axial direction for -21< x_c/d <14. Inside the tuyere, for -21< x_c/d <0, rms values are very low, indicating that large perturbations are diminished. This result is well-known and documented for tuyeres operating in furnaces (e.g. in the steel and copper industries) under a jet regime, with sonic or supersonic flow, where exit underexpansion ratios, η_e ≈2 can suppress pressure fluctuations inside the tuyere, including back attack events (Miaosheng et al. [34]). This is also substantiated by results from other experiments and industrial applications (Brimacombe et al. [8], Bustos et al. [9], Taylor et al. [53]). However, small pressure fluctuations are present, but typical effects of back-attack and large pressure peaks are not observed or have a small frequency as underexpansion increases (Gulawani [25] and Miaosheng et al. [34]). In the tuyere near field, for 0< x_c/d <1, fluctuations are small and related to small bulging events. For 1< x_c/d <1.6 there is a sharp increase in fluctuations followed by decrease for 1.6< x_c/d <1.8, and this repeats for 1.8< x_c/d <8. Peak values are reached at the position where, in average, the first set of shockwaves reflect. In this regard, it has been argued by Tang et al. [52] and in two articles by Shi et al. (Shi et al. [49], Shi, Wang and Dai [50]) that shockwaves may be the source of instability feedback for submerged injection and that such interaction inside a bulge can explain further interface instability development. Therefore, the average position of shockwave reflection may indicate the location where instabilities growth becomes more important. For 7< x_c/d <14 pressure rms tends to die out, but velocity rms shows that there are considerable fluctuations just outside the potential core. This may indicate that inertia becomes less important and

that buoyancy predominates, characterized by larger interface deformations. Further downstream, it is suspected that velocity fluctuations will be dominant over pressure variations, where pinch-off events occur.

Figure 4.19 shows the average air volume fraction, $< \alpha >_t$, normalized by the centerline value, α_c, plotted for different positions in the streamwise direction. As shown in Figure 4.19 a), close to the tuyere, at x/d=4, the VOF model is not able to capture real air volume fraction, in part due to the presence of typical bubble curtain surrounding the jet. Another reason for this, is that a higher grid density would be needed to reproduce generation of bubbles where shearing is present close to the injection point. To overcome part of this deficiency, considerably larger simulation times would be required to produce detachment of bubbles, scaling with d. Downstream, at x/d=8 the VOF model captures entrainment effects. The slight asymmetry in the solid line of Figure 4.19 b) is related to the interface deformation in time. This can be resolved by increasing simulation time which would render a smoother profile, moving away from the injection point. However, this will not produce a significant change in statistics and subsequent analysis.

4.4.2. Submerged Jets Velocity and Pressure Distribution

Figure 4.20 a) shows, for case SJ, the contours of mean streamwise velocity, $< u_x >_t /u_e$, on the xy-plane through the tank middle, and Figure 4.21 a) shows the distribution of streamwise velocity rms, $[u_x]_{rms}/u_e$, on the same plane. The contours of $[u_x]_{rms}/u_e$ and $< u_x >_t /u_e$ reveal that the largest velocity fluctuations occur at the average location of the first shockwave reflection. Furthermore, almost null velocity fluctuations are found inside the potential core, for x/d <1.8. Moreover, fluctuations are also present in the y-direction outside the Ma=1 limit line and are mainly explained by velocity variations near the interface, being deformed predominantly by KH type of instabilities. In addition, for x/d <1.8 velocity fluctuations outside the potential core are smaller as compared to those found for x/d >1.8. Thus, upstream this location, it can be expected that entrainment rates will bee smaller as well. In contrast, moving downstream for x/d >1.8, fluctuations related to shockwave reflection tend to die out, but with increasing fluctuations outside the potential core. All these characteristics indicate larger interface deformation that can be associated to increasing entrainment rates (Drew et al. [18]). In summary, velocity fluctuations outside the core can be used to indicate the level jet interface deformations, reveal the presence of "turbulence driven by density difference" (Weiland & Vlachos [57]) and analyze the mixing characteristics of submerged jets.

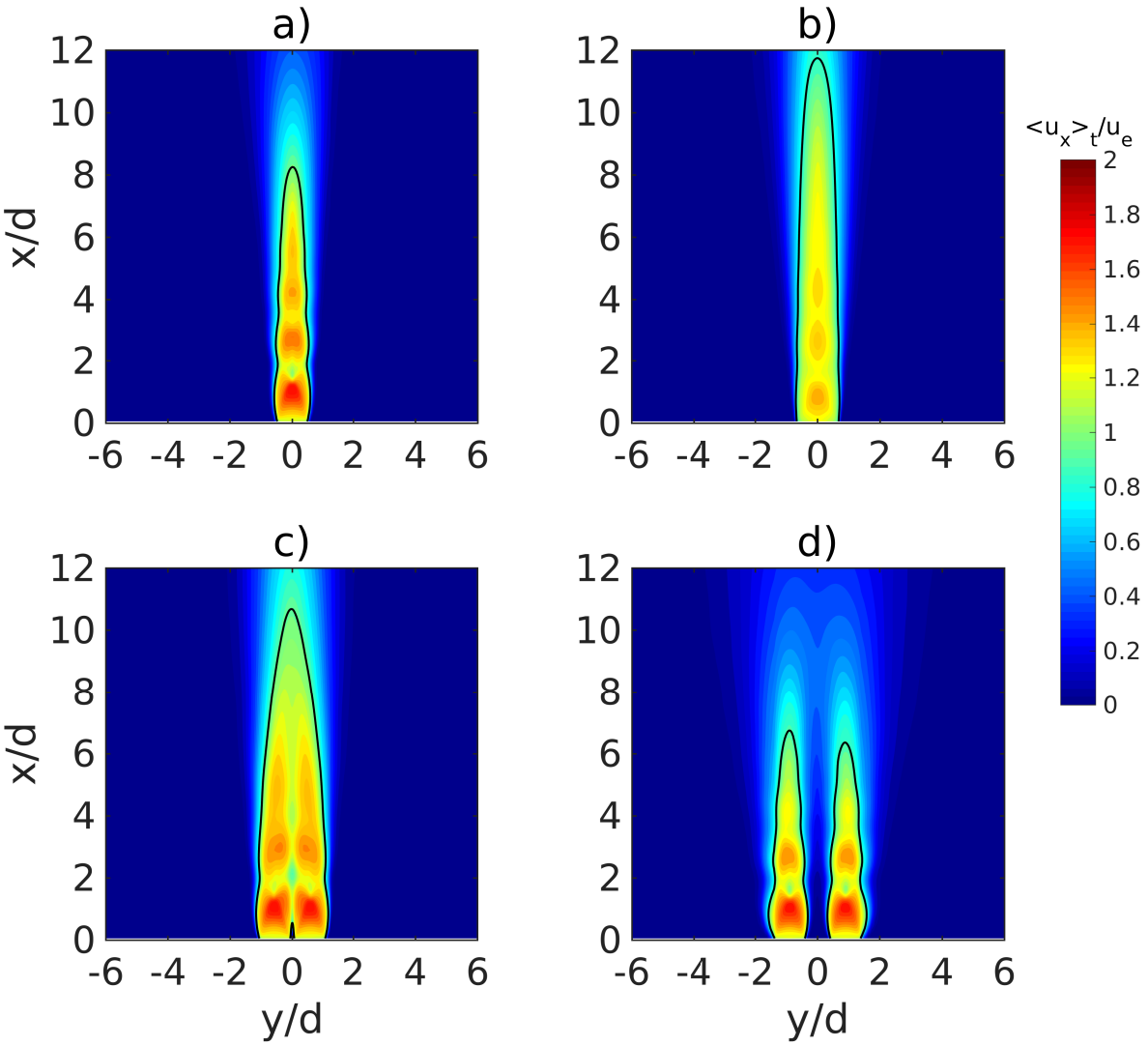

Figure 4.20: Average streamwise velocity field normalized by exit velocity, $< u_x >_t /u_e$, within the region defined by 0$< x/d <$12 and -6$< z/d <$6, for cases: a) SJ, b) SJ-eq, c) TJ1.15 and d) TJ1.8. The continuous contour line for Ma=1 is also plotted.

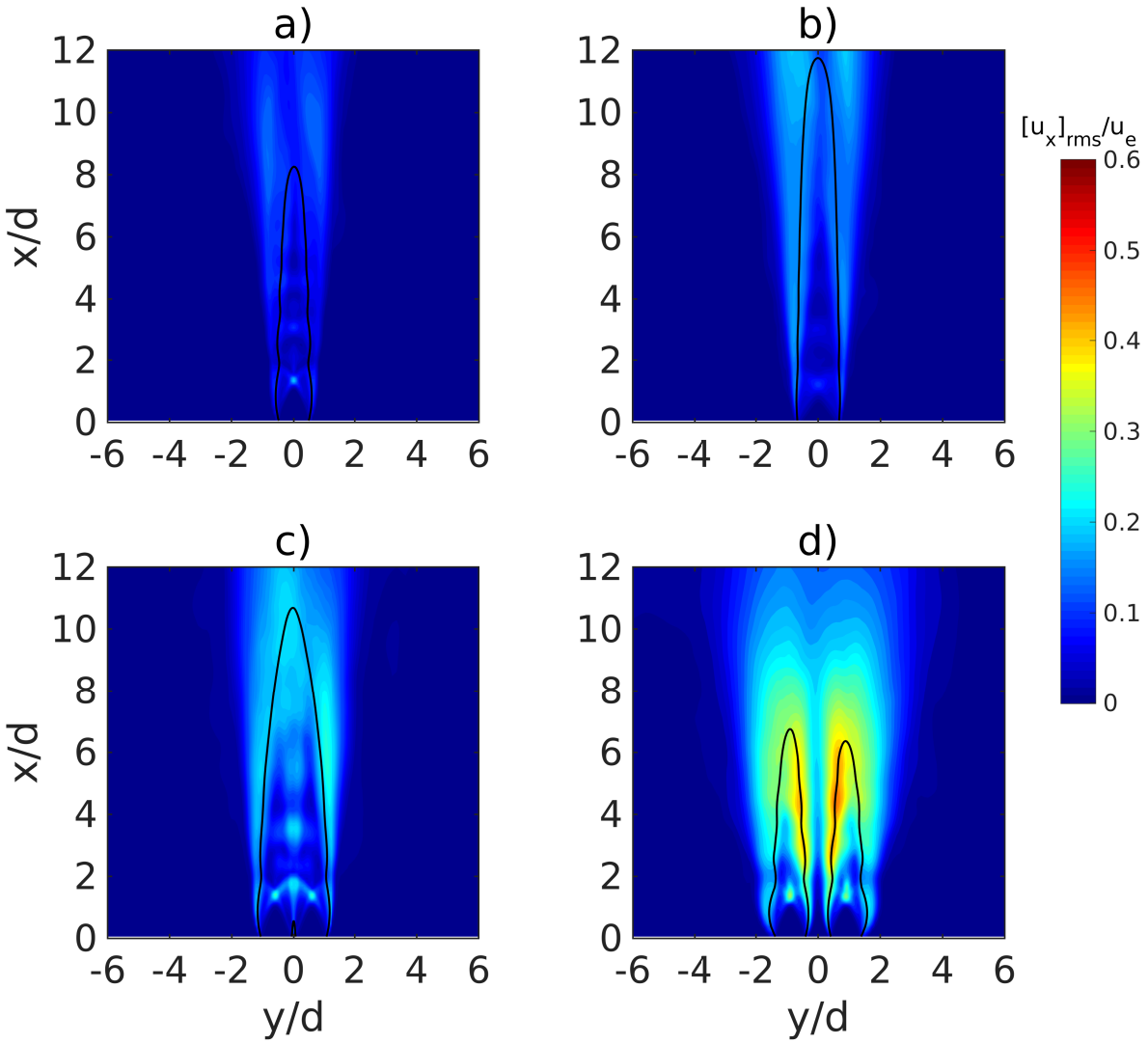

Figure 4.21: Normalized rms streamwise velocity field, using the air exit velocity, $[u_x]_{rms}/u_e$ within the region defined by 0< x/d <12 and -6< z/d <6, for cases: a) SJ, b) SJ-eq, c) TJ1.15 and d) TJ1.8. The continuous contour line for Ma=1 is also plotted.

In case SJ-eq, the contours of $< u_x >_t /u_e$ and $[u_x]_{rms}/u_e$ in Figure 4.20 b) and Figure 4.21 b), respectively, show a distribution similar to case SJ, but with larger penetration and velocity fluctuations outside the potential core. This level of penetration is mainly due to higher momentum (Harby et al. [26]), while fluctuations can be attributed to the lower value of η_e, as with lower underexpansion levels the submerged jet has larger air-water interface fluctuations (Miaosheng et al. [34], Tang et al. [52]).

In case TJ1.15, from the $< u_x >_t /u_e$ contours shown in Figure 4.20 c), almost identical

jets are formed, leaning towards each other with an elongation of the first two cells. A *flow-centerline* is defined here by the points of minimum pressure (where shockwaves reflect), having an inclination of about 2 degrees towards the tank axis, and used later to generate profiles along this line. Furthermore, following the work of Carasik et al. [10], the average merging point, i.e. the position where centerline streamwise velocity changes sign from negative to positive, locates at x_{mp}/d=0 and the average combined point, i.e. where the first maximum streamwise velocity is found, locates at x_{cp}/d=1.3. The configuration in this case shows that, in average, a combined potential core region appears, having approximately twice the width of a single jet, producing a similar effect observed in experiments of underexpanded supersonic air jets, using the Schlieren photography (Field et al. [21]). A combined potential core is defined here, in a way similar to a single potential core (Franquet et al. [22]), as the region delimited by the line where $< Ma >_t$=1, and outside this region the flow is everywhere subsonic. The combined potential core length is measured between tank bottom and the last point where $< Ma >_t$=1 in the streamwise direction. The difference between single and combined potential cores is that, inside the latter, converging, merging and combined regions can be defined. The combined potential core in this case has a larger extent, and can be related to larger inertial length (Harby et al. [26]) as compared to case SJ, which otherwise would have been obtained by increasing the underexpansion level of a single jet (Phalnikar et al. [42]). As for streamwise velocity rms, Figure 4.21 c) shows similar distribution to that described in case SJ, where the first shockwave reflection is found at x/d=1.8. In addition, for x/d >1.8, outside the $< Ma >_t$=1 limit line, there is an increase of about two times the rms of streamwise velocity obtained in case SJ, indicating larger entrainment rates as compared to case SJ. It is interesting to notice that, along the tank axis, velocity fluctuations appear, corresponding to the interaction between jets, mainly due to interspace shockwave reflections. Furthermore, and similar to case SJ, these fluctuations tend to die out inside the combined potential core.

Figure 4.20 d) shows, for case TJ1.8, a return to the single jet cell structure, roughly similar to case SJ, but with shorter cores, each of them reaching L_p/d=6.5. The merging point locates at x_{mp}/d=0 and the combined point, at x_{cp}/d=7.8. In contrast to case TJ1.15, jets do not lean towards each other, since interspace pressure is approximately equal to the hydraulic pressure, and then no "ambient" force acts on the jets (Carasik et al. [10]). The merging point locates outside the individual potential cores, whereas in case TJ1.15 the shorter interspace generates a combined core, where the merging point locates inside it. This suggests that shorter interspace favors jets inertia, where the core can be longer than the one obtained with a larger interspace, as individual jets inertia seems not enough to produce at least the same core length obtained with a single tuyere (the latter, resembling a case with very large separation). In Figure 4.21 d) two main zones of streamwise velocity rms appear, and are almost symmetric about the xz-plane at y/d=0. Inside each individual core, fluctuations distribution is similar to that observed in case SJ. In contrast, outside the sonic line, velocity fluctuations are the highest and

are not located along the tank axis, but within the zone defined by 3< x/d <6 and -0.5< y/d <0.5. The fluctuations magnitude are up to three times higher than in case TJ1.15, indicating that the largest entrainment rate is expected for case TJ1.8. This increase in velocity fluctuations with larger tuyere separation are also observed in the experiments of Oskouie et al. [39] for s/d=1.8 and higher. Such interaction has an effect in the average potential core which, due to larger velocity variations, produces overall shorter individual cores. This could be analyzed through a theoretical approach to the interaction of incoming KH type of instabilities from each jet, which may explain the indicated larger fluctuations for increasing tuyere interspace.

To show that twin jets movement is predominantly in the xy-plane, Figure 4.22 shows the time-average distribution of spanwise velocity, $< u_y >_t /u_e$, in the y-direction. The lateral motion close to the nozzle, at x/d=2, covers mostly the y-direction where the highest velocities are found as compared to the location at x/d=5. Furthermore, spanwise velocity rms, $[u_y]_{rms}/u_e$, are shown in Figure 4.23, on the same yz-planes. A similar result is obtained here, indicating that spanwise fluctuations are also dominant in the y-direction.

Figure 4.24 shows the average pressure field for all cases. The pressure spatial flucutation occurs inside the potential core, and outside it pressure corresponds to the hydrostatic pressure. The cell arrangement in the cores is more clear using these fiels, where in Case SJ the spatial pressure variation shows higher difference between local maximum and minimum values than in Case SJ-eq. In Case TJ1.15 it is seen that at about x/d=2 the cells merge and generate a different cell structure, as already observed in underexpanded air twin jets (Field et al. [21]). For Case TJ1.8, the cell arrangement is recovered within the separated potential cores.

Figure 4.25 shows the rms values of the pressure field, which can bee seen as the effect of pressure in the submerged jets. In Case SJ the maximum pressure fluctuation,$[p]_{rms}/p_b$=0.6, is at the location where shockwaves reflect and decay rapidly along the streamwise direction, inside the potential core. Outside the core, pressure fluctuations are relevant in the spanwise (and radial) direction for about $y/d = \pm 1.8$ and reach levels of $[p]_{rms}/p_b$=0.07 similar to those inside the core for 6< x/d <8. In Case SJ-eq the maximum pressure fluctuations are slightly smaller than in Case SJ inside the core, reaching $[p]_{rms}/p_b$=0.48, but slightly higher outside it, where $[p]_{rms}/p_b$=0.1, covering a wider range, defined about $y/d = \pm 2$. Case TJ1.15 shows that fluctuations are in general higher inside the core, where the maximum value is $[p]_{rms}/p_b$=0.68 , but levels outside it are similar to those found in SJ-eq, noticing a small zone with a larger increase in fluctuations in the range $y/d = \pm 1.8$, where $[p]_{rms}/p_b$=0.13. In Case TJ1.8 pressure fluctuations are clearly higher, where the maximum value is $[p]_{rms}/p_b$=0.72, and outside it reaching $[p]_{rms}/p_b$=0.15 in the range $y/d = \pm 2$, noticing in the cores interspace a pressure-driven interaction is identified in the same region where large rms velocity are present.

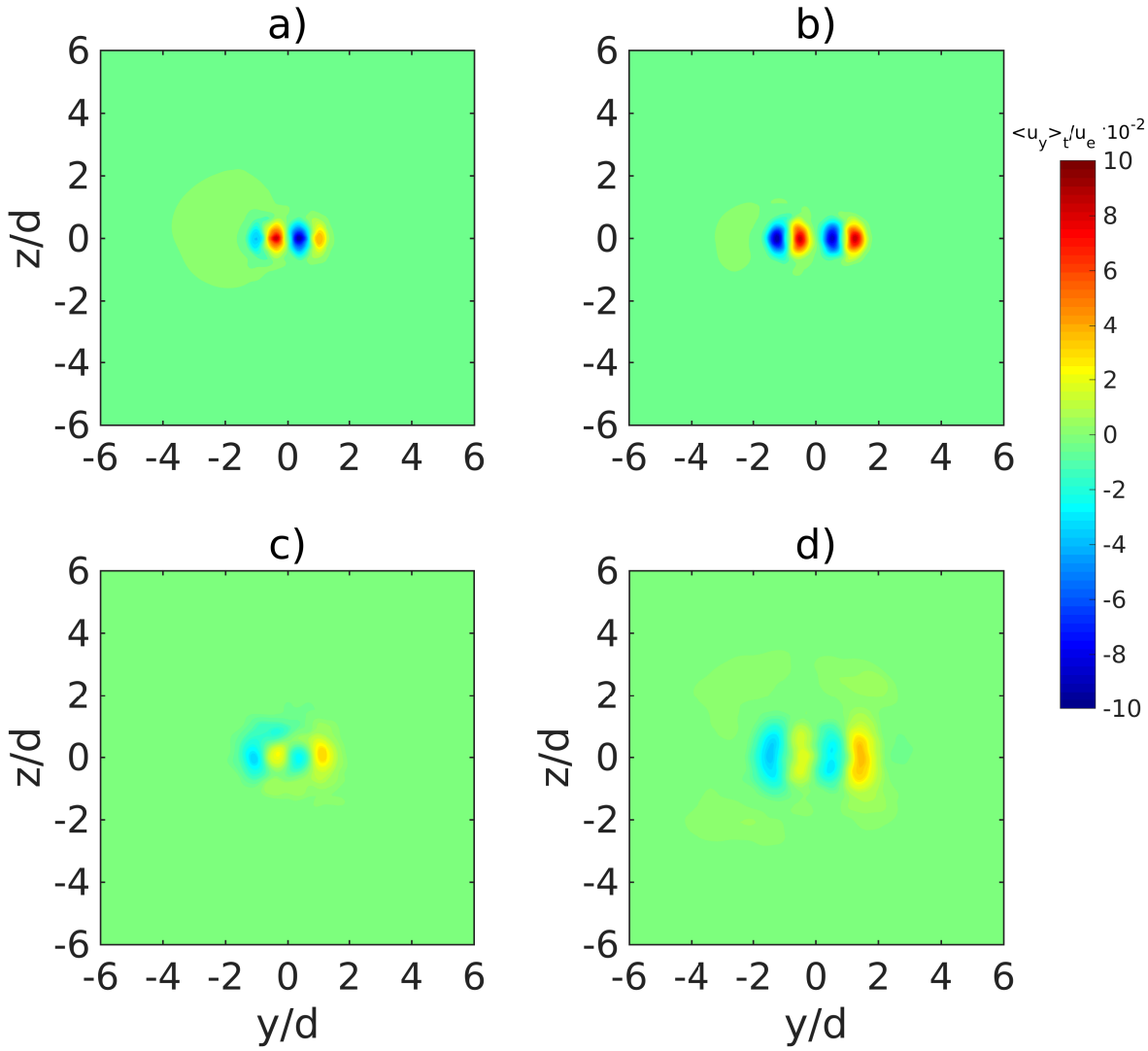

Figure 4.22: Average spanwise velocity field,$< u_y >_t$, normalized by exit velocity in two yz-planes,for cases: a) TJ1.15 at x/d=2, b) TJ1.8 at x/d=2, c) TJ1.15 at x/d=5 and d) TJ1.8 at x/d=5.

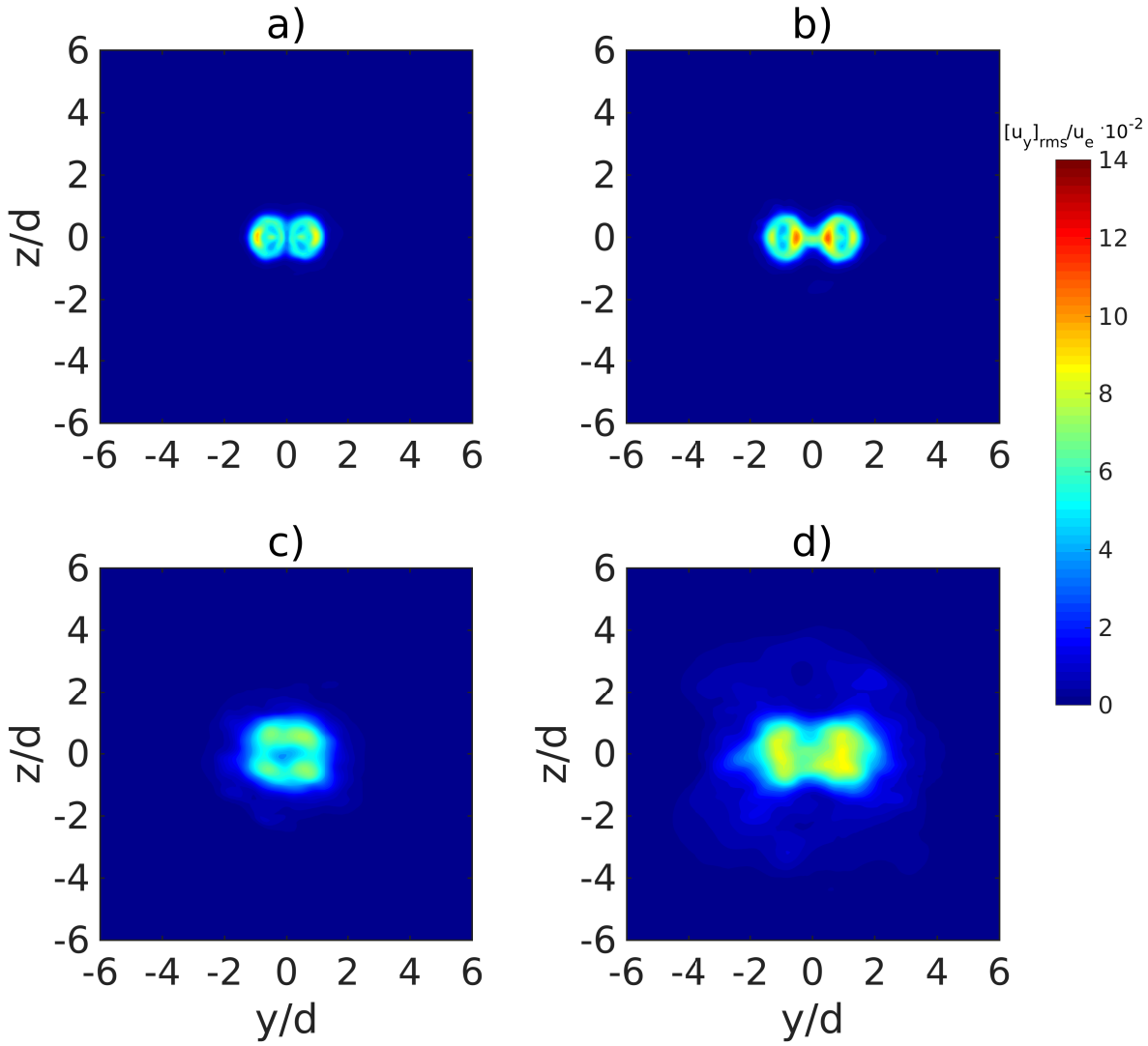

Figure 4.23: Normalized rms spanwise velocity field,$< u_y >_t$, using the air exit velocity in two yz-planes,for cases: a) TJ1.15 at x/d=2, b) TJ1.8 at x/d=2, c) TJ1.15 at x/d=5 and d) TJ1.8 at x/d=5.

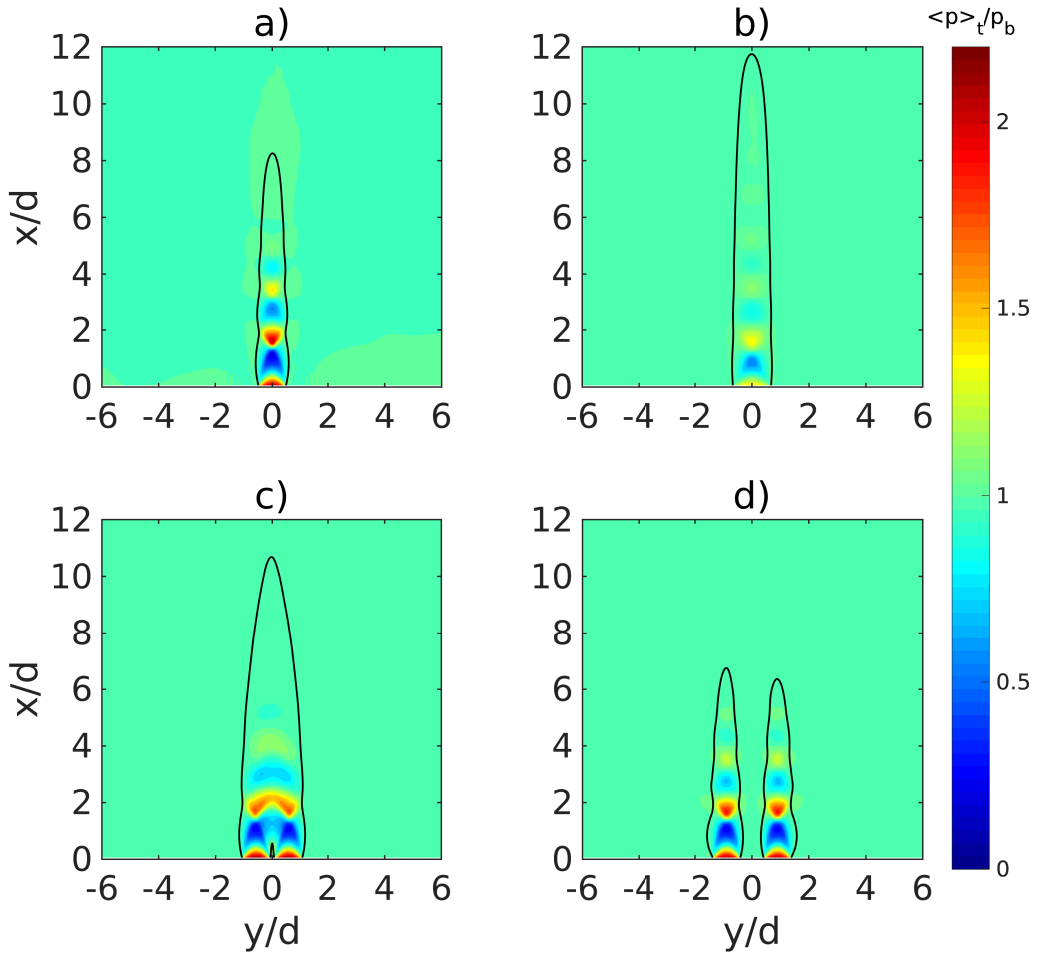

Figure 4.24: Average pressure field normalized by back-pressure, p_b, $< p >_t / p_b$, within the region defined by $0 < x/d < 12$ and $-6 < z/d < 6$, for cases: a) SJ, b) SJ-eq, c) TJ1.15 and d) TJ1.8. The continuous contour line for Ma=1 is also plotted.

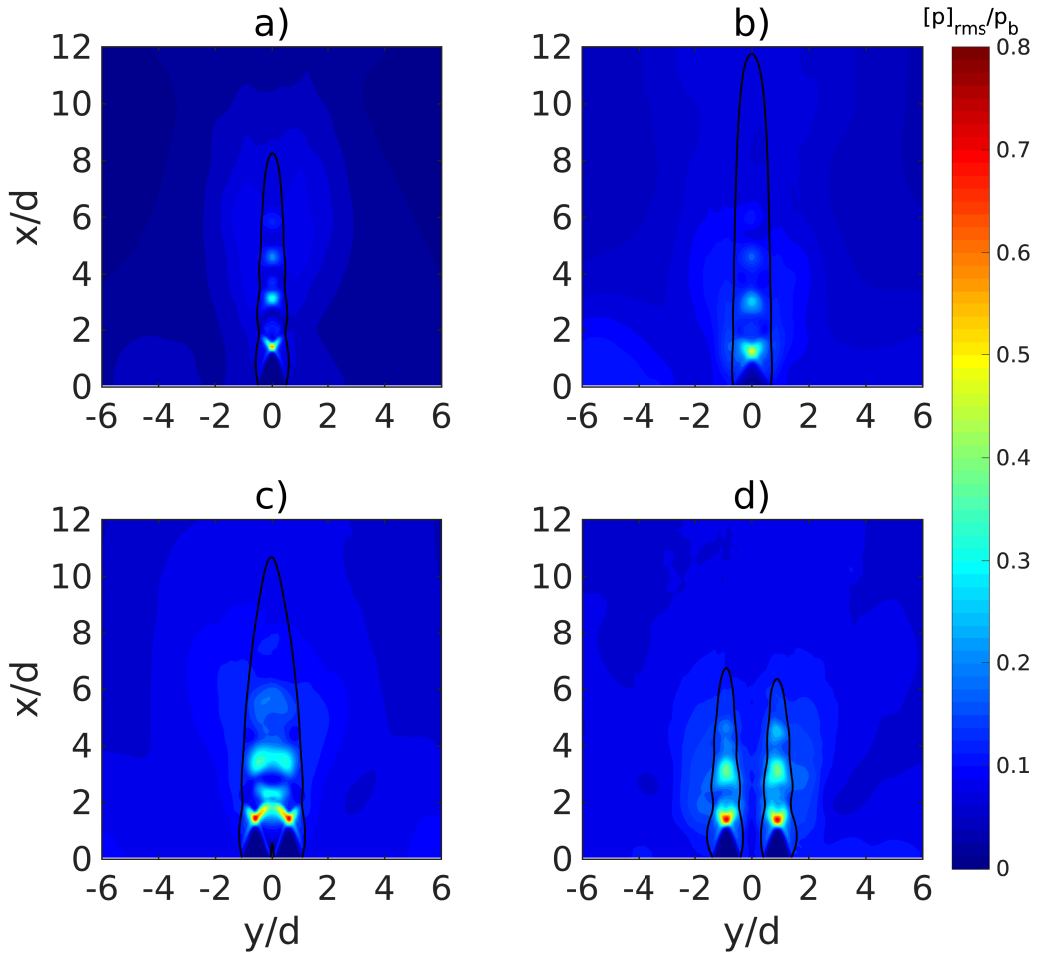

Figure 4.25: Normalized rms pressure field, normalized by p_b, $[p]_{rms}/p_b$, within the region defined by 0< x/d <12 and -6< z/d <6, for cases: a) SJ, b) SJ-eq, c) TJ1.15 and d) TJ1.8. The continuous contour line for Ma=1 is also plotted.

In general, it is found from the pressure fluctuations that single jet in Case SJ-eq and twin jet configurations, TJ1.15 and TJ1.8, offer larger values outside the core as compared to the single jet (Case SJ). However, the levels outside the core, as compared to those found inside it, show that away from the tuyeres pressure variations do not have an effect in the average jet structure. Only when there is enough separation between jets, pressure fluctuations are the highest, particularly in the core interspace where an interaction driven by pressure fluctuation is found.

With the preceding analysis and discussion, it is possible to establish that, in the average sense, when space between the submerged air jets is small, shockwave interaction allows the generation of a combined potential core, and that it is no longer formed when the spacing between tuyeres is enough for hydrodynamic effects to appear.

4.4.3. Entrainment

Streamwise rate of entrainment is computed, for all cases, using the following relation (Drew et al. [18]):

$$\frac{dm_{ent}}{dx} = 2\pi r_{\infty}\rho_2[u_{\infty}^2 \sin^2(\beta) + v_{\infty}^2 \cos^2(\beta)]^{0.5} \tag{4.1}$$

Where m_{ent} is the mass flow entrained by the liquid. The term dm_{ent}/dx is calculated, using a conical surface of half-angle β (see Table 4.1), that corresponds to the jet boundary, and radius r_{∞} outside the air interface; the streamwise, u_{∞}, and lateral velocities, v_{∞}, are both present outside jet boundary.

It is important to mention that in this study the main focus is the submerged jet, defined statistically between the point of injection and extending up to the inertial length. Away from where the inertial length ends, pinch off is observed and buoyancy effects are the relevant flow features which are the main contributor to entrainment. With this in mind, the entrainment is computed for the jet structure, where entrainment starts and has different contributions from mainly two type of instabilities: Rayleigh-Taylor (RT) and Kelvin-Helmholtz (KH).

The normalized entrainment rate, $F_{ent} = \frac{dm_{ent}}{dx}(m_e u_e \rho_2)^{-0.5}$, is plotted in Figure 4.26 and compared to experimental data obtained from experiments (Loth & Faeth [32] and Carreau et al. [11]), recalling that in the present simulations the injection arrangement is similar to those presented in the experiments. Also, the well-known model from Ricou & Spalding [45] is used to compare results from cases SJ and TJ1.8. In addition, the asymptotic model from Epstein et al. [19] is used, as it represents effects of KH instabilities in the rate of entrainment. In Case SJ, shown in Figure 4.26 a), some fair agreement with experiments is obtained for $2< x/d <10$. Close to the injection points, and along to most part of the potential core, entrainment shows mild variations, in contrast to the increase close to the core tip, at x/d=8. For $x/d >10$, the entrainment shows a significant increase, but overestimating the data from experimental results. This effect may be due to a limitation of the present simulations since, to capture jet motion several diameters away from the potential core, where RT instabilities, buoyancy effects and pinch-off events are present (Weiland & Vlachos [57]), considerably longer simulation times are needed. Another feature of the present simulations that can be improved, is the underexpansion effect in the shock cells number, as they would lead to larger potential cores. As for entrainment models, the Ricou & Spalding [45] model shows, for cases SJ and TJ1.8, that the constant entrainment rate offers a rough estimate for $x/d <1$. The model from Epstein et al. [19] shows similar profile to that obtained for case SJ, but it underestimates rate of entrainment, an effect observed in the experimental work by Drew et al. [18]. Therefore, the characteristics for entrainment rate found in this study for a

single jet is in agreement to what is described in experimental works (Loth & Faeth [32], Weiland & Vlachos [57] and Drew et al. [18]).

Regarding the rest of jet configurations, it is interesting to notice that cases SJ and SJ-eq show similar profiles, but for cases TJ1.15 and TJ1.8 normalized entrainment rates are larger, as presented in Figure 4.26 b). This can be related to the increase in velocity fluctuations levels observed for twin jets (see Figure 4.21), rather than the influence of larger mass flow injected.

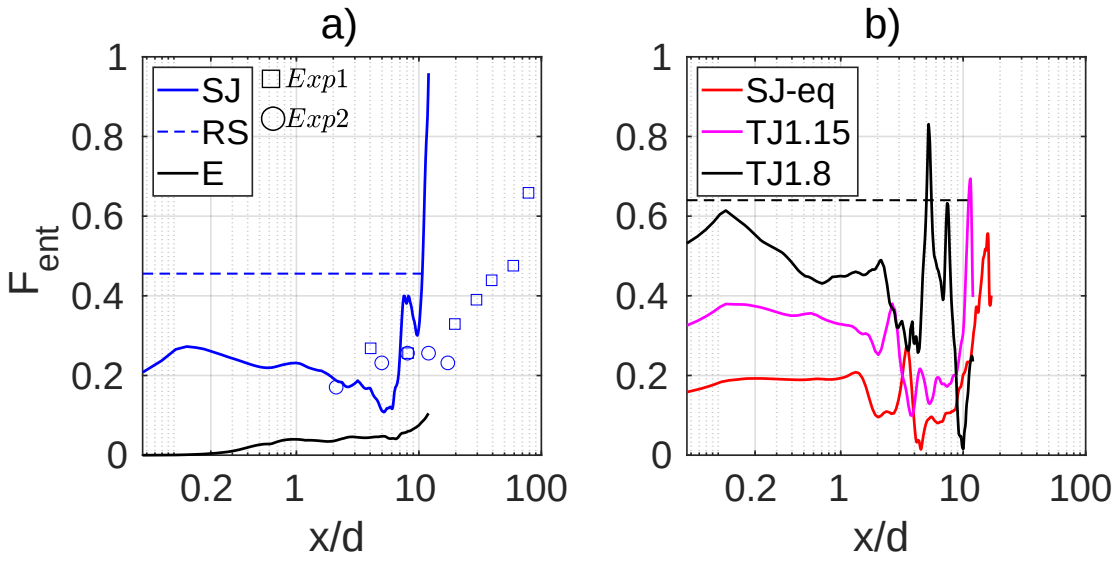

Figure 4.26: Normalized entrainment rate, $F_{ent} = \frac{dm_{ent}}{dx}(m_e u_e \rho_2)^{-0.5}$, using the liquid density, ρ_2, and the tuyere thrust at the exit, computed as $m_e u_e$, where m_e is the injected air mass flow rate, and the exit velocity, u_e: a) Case SJ, b) Cases SJ-eq, TJ1.15 and TJ1.8. RS: Ricou-Spalding model, in dashed lines, Ricou & Spalding [45] with coefficient c_2=0.32. E: Epstein asymptotic model Epstein et al. [19]. *Exp1* corresponds to experimental data from Loth & Faeth [32] and *Exp2*, to results from Carreau et al. [11].

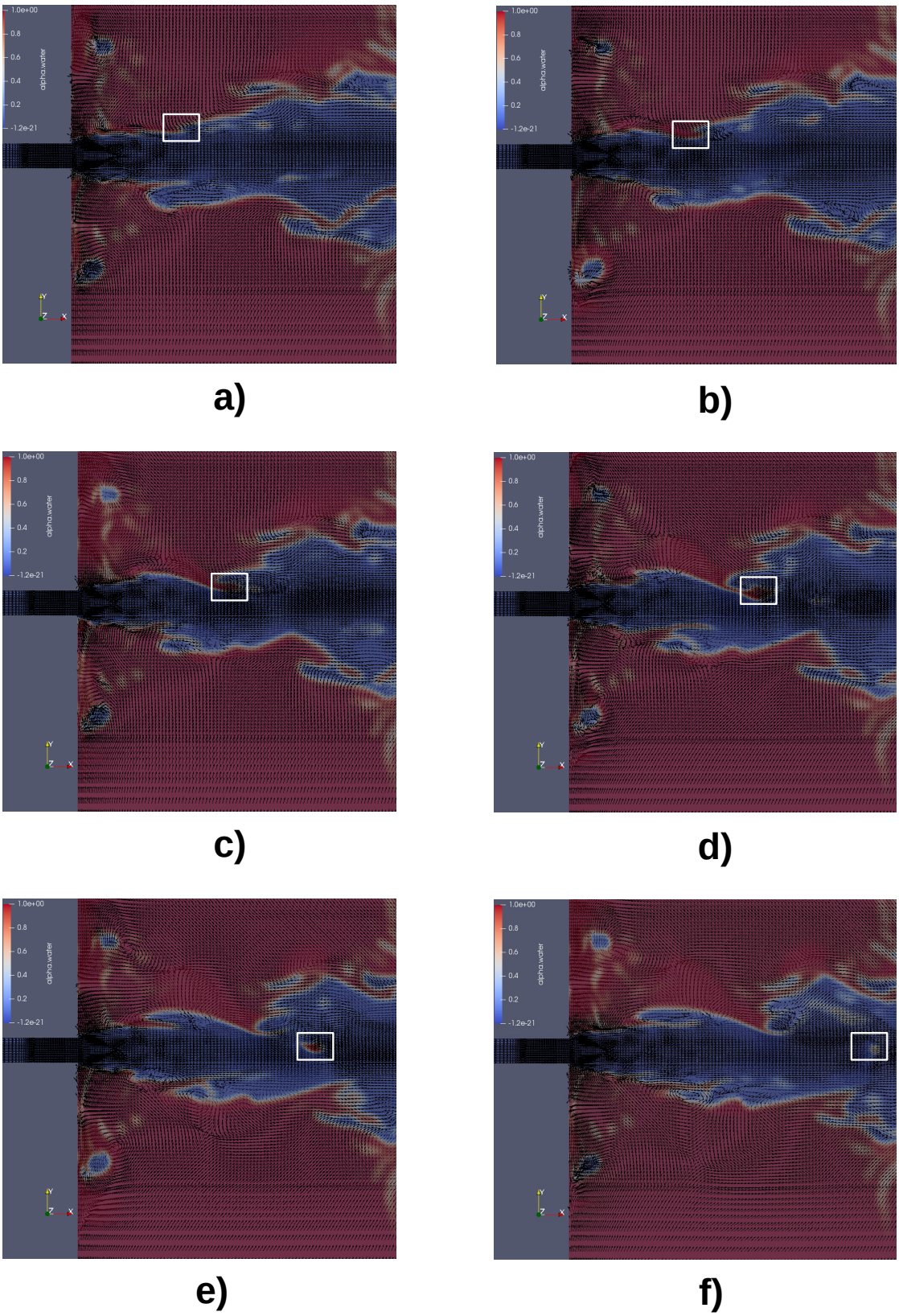

Figure 4.27: VOF and velocity vectors for Case SJ. A white square follows an entrained droplet into the gas jet. This shows the effect of entrainment, related to mixing between liquid and gas phases: a) t^e=3119, b) t^e=3152, c) t^e=3185, d) t^e=3218, e)t^e=3251, f) t^e=3284.

To show an insight of how the entrainment is produced in the submerged jet, Figure 4.27 shows the contours of α and velocity vectors for case SJ. The white square follows a droplet that is entrained towards the center of the gas jet. It is observed that first a deformation of the interface is produced. At a certain location the interface is distorted enough so that the liquid has momentum to break this interface and a small droplet is now entrained in the gas jet, and travels towards the center. The faded contour observed in the last frame (inside the white square) is because the droplet has moved out of the plane. This process repeats during the injection, and away from the injection point, more entrained fluid is found, an the rate of entrainment increases, as shown by the present simulation results. Far away from the inertial range of the submerged jet, near the pinch-off location, air bubbles are present and larger portions of liquid are now entrained (Weiland & Vlachos [57], Harby et al. [26]). This explains the sharp increase in the rate of entrainment observed in experiments, which allows mixing of the gas and liquid phases.

4.4.4. Submerged Jets Spread Rate

The spreading rate is computed, following the analysis of Loth & Faeth [32]. The jet width, w_α, is computed in this study, using the time-averaged air volume fraction (in the spanwise direction, y) as:

$$w_\alpha = y^+_{\alpha,0.5} - y^-_{\alpha,0.5} \tag{4.2}$$

Where $y^-_{\alpha,0.5}$ is defined in the region y <0 where

$$< \alpha(x, y^-_{\alpha,0.5}, 0) >_t = 0.5, \tag{4.3}$$

and $y^+_{\alpha,0.5}$ to the region $y \geq 0$ where

$$< \alpha(x, y^+_{\alpha,0.5}, 0) >_t = 0.5. \tag{4.4}$$

For the twin configurations, the most external boundaries are considered. This definition includes the effects of submerged jets mixing properties. Alternatively, the jet width can be computed, using the dynamic pressure normalized by the dynamic pressure along the tank centerline, $p_{dyn,c}$, so that

$$w_p = y^+_{p,0.5} - y^-_{p,0.5} \tag{4.5}$$

Where the terms $y^\pm_{p,0.5}$, analog to the definition of $y^\pm_{\alpha,0.5}$, are defined where

$$< \frac{p_{dyn}(x, y^{\pm}_{p,0.5}, 0, t)}{p_{dyn,c}} >_t = 0.5. \tag{4.6}$$

For twin jets the most external boundaries are also used for the calculations.

Air volume fraction indicates that the jets spread rate, for cases SJ, Sj-eq and TJ1.15 is between 1.4 to 1.6 times the value of single-phase turbulent jets, as found in the Loth & Faeth [32] experiment. However, it is suspected that the jet width obtained in the present simulations may not be completely representative in the region close to the tuyere, since the generation of small bubbles during the injection is not accounted for. In contrast, for case TJ1.8, the jet has nearly 4 times that of a single phase-jet. This shows that mixing can be enhanced with this configuration. In contrast, for all cases, the jet spread rate based on dynamic pressure is closer to the typical values found in single-phase jets.

The main characteristics of single and twin jets are shown in Table 4.1.

Table 4.1: Summary of core length, L_p/d, the location of converging point, x_{cp}/d, the estimated volume-fraction-based jet spread rate, $\frac{1}{2}\frac{dw_\alpha}{dx}$, and dynamic-pressure-based spread rate, $\frac{1}{2}\frac{dw_p}{dx}$. In addition, the computed half-angle of the jet (measured in sexagesimal degrees) β, is presented. VOF-SR: Volume-fraction-based jet Spread Rate, obtained by others. SR: Spread Rate of turbulent jets, obtained by others. N.A.:Data Not Available in Literature.

Case	L_p/d	x_{cp}/d	$\frac{1}{2}\frac{dw_\alpha}{dx}$	VOF-S.R.	$\frac{1}{2}\frac{dw_p}{dx}$	S.R.	β [deg]
SJ	8	-	0.13	0.18 [32]	0.09	0.094 [43]	7.4
SJ-eq	11.5	-	0.15	0.18 [32]	0.079	0.094 [43]	8.5
TJ1.15	10	1.3	0.15	N.A.	0.07	N.A.	8.5
TJ1.8	6.5	7.8	0.35	N.A.	0.073	0.14 [39]	19.3

4.4.5. Profiles along Centerlines

Figure 4.28 shows time-average and rms profiles for cases SJ and TJ1.8 along respective centerlines; and for case TJ1.15, along a flow-centerline that is inclined at 2 degrees. In Figure 4.28 a) and b) time-average profiles in cases TJ1.15 and TJ1.8 show an overall different cell arrangement. In particular, for cases SJ, TJ1.15 and TJ1.8, each Mach and pressure profiles show little differences for $0< x_c/d <3$. However, for $x_c/d >3$ the cell structure clearly changes in the twin jet configuration. In case TJ1.15 cells are damped and elongated so that the potential core length is L_p/d=10, while in case TJ1.8 the cells are damped in a shorter space, such that the potential core length is reduced to L_p/d=6.5.

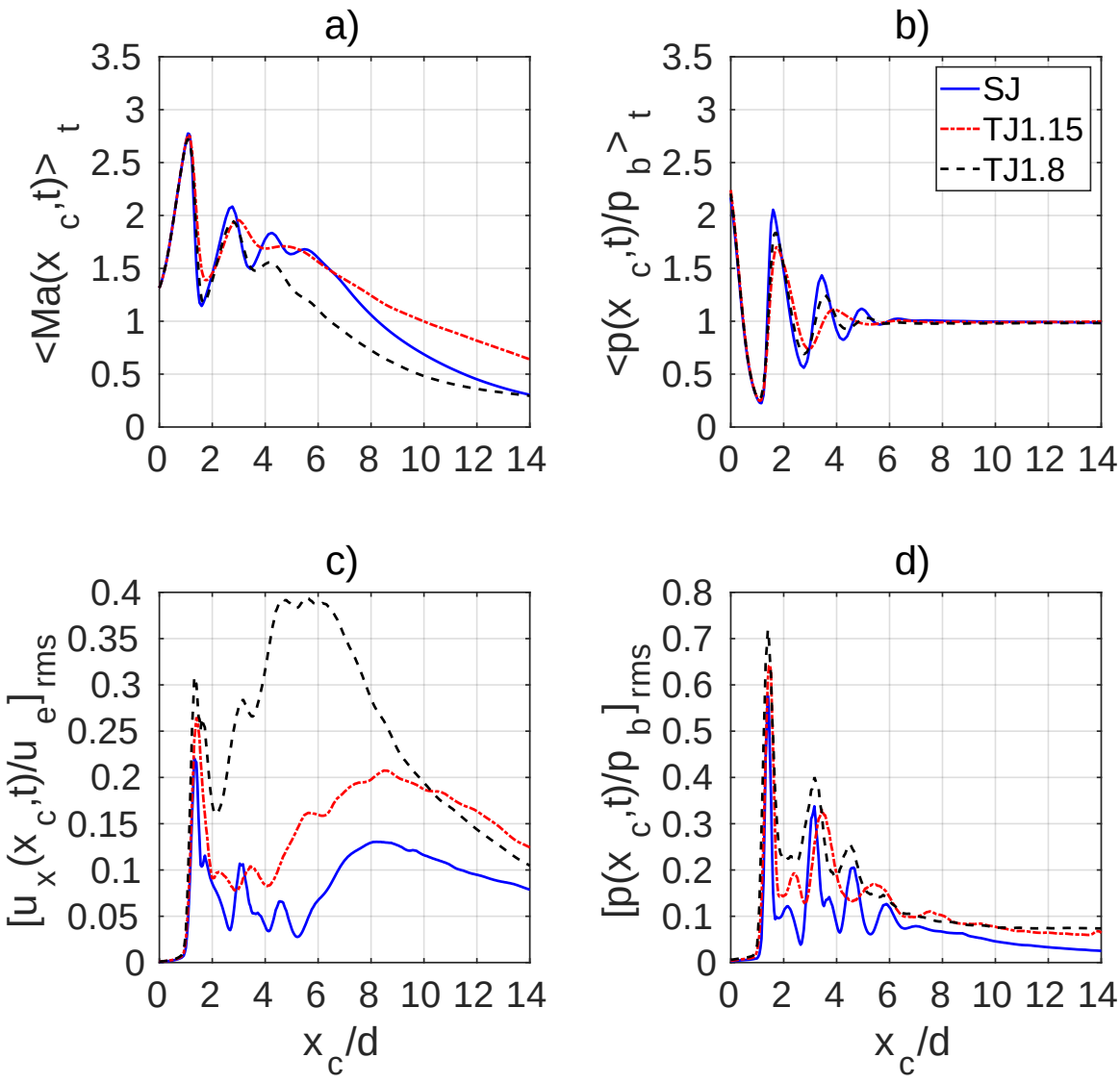

Figure 4.28: Comparison of Cases SJ, TJ1.15 and TJ1.8, along tuyere centerlines and flow-centerlines (for case TJ1.15) coordinate, x_c. Time-averaged profiles of :a) Mach and b) Pressure. Rms profiles of: c) Streamwise velocity, d) Pressure. In the twin tuyeres, the profile along tuyere No.1 is used.

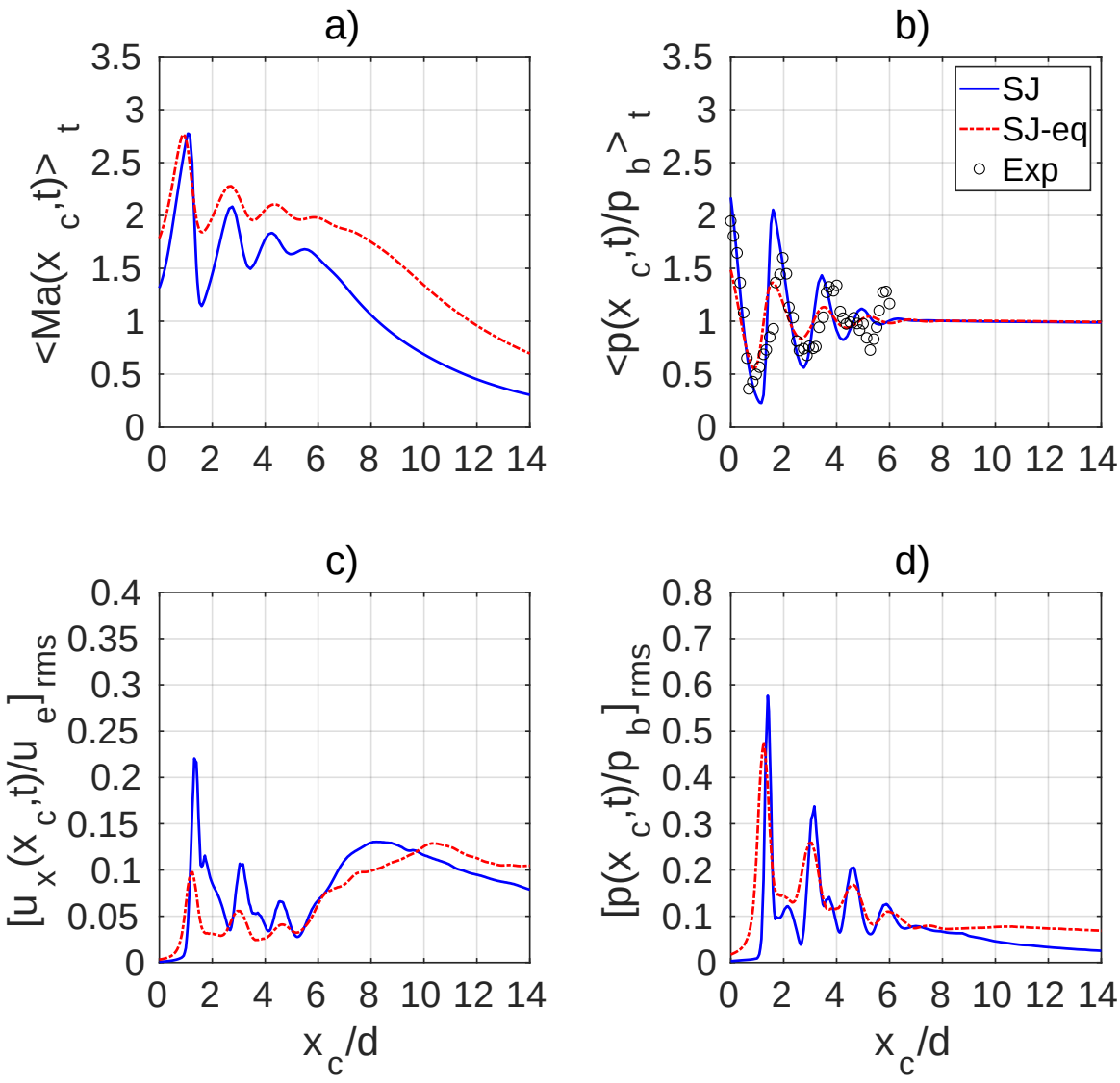

Figure 4.29: Comparison of Cases SJ and SJ-eq, along the tuyere centerline, x_c, measured in units of d (not d_{eq}). Time-averaged profiles of: a) Mach and b) Pressure. Rms profiles of: c) Streamwise velocity, d) Pressure. In the twin tuyeres, the profile along tuyere No.1 is used. Also, normalization of x_c is done with d and not d_{eq}.

The rms profiles of streamwise velocity and pressure (along flow-centerlines) for cases SJ, TJ1.15 and TJ1.8, are shown in Figure 4.28 c) and d), respectively. Profiles are almost the same for $0< x_c/d <1.8$, where fluctuations are small inside and outside the core. For all these cases, maximum value is at x_c/d=1.8 and at this point, fluctuations are higher for cases TJ1.15 and TJ1.8 as compared to SJ. For $1.8< x_c/d <10$ velocity fluctuations are the highest for case TJ1.8, as substantiated by the rms distribution (see Figure 4.21). In this portion of the core, there is a second local maximum value located where the potential core ends. In case SJ, this second maximum value is located at x_c/d=8; in case

TJ1.15, at x_c/d=10 and in case TJ1.8, at x_c/d=6. For x_c/d >10, fluctuations decrease, but cases TJ1.15 and TJ1.8 still show larger levels, compared to case SJ, noticing that they are still comparable to levels found inside the core. Regarding, pressure rms, Figure 4.28 d) shows a similar behavior in the range $0 < x_c/d < 10$. At locations where the potential core ends, pressure fluctuations are decreasingly small. This correlates with the relevance of buoyancy over inertia downstream these locations, as observed earlier in the contours of streamwise velocity rms.

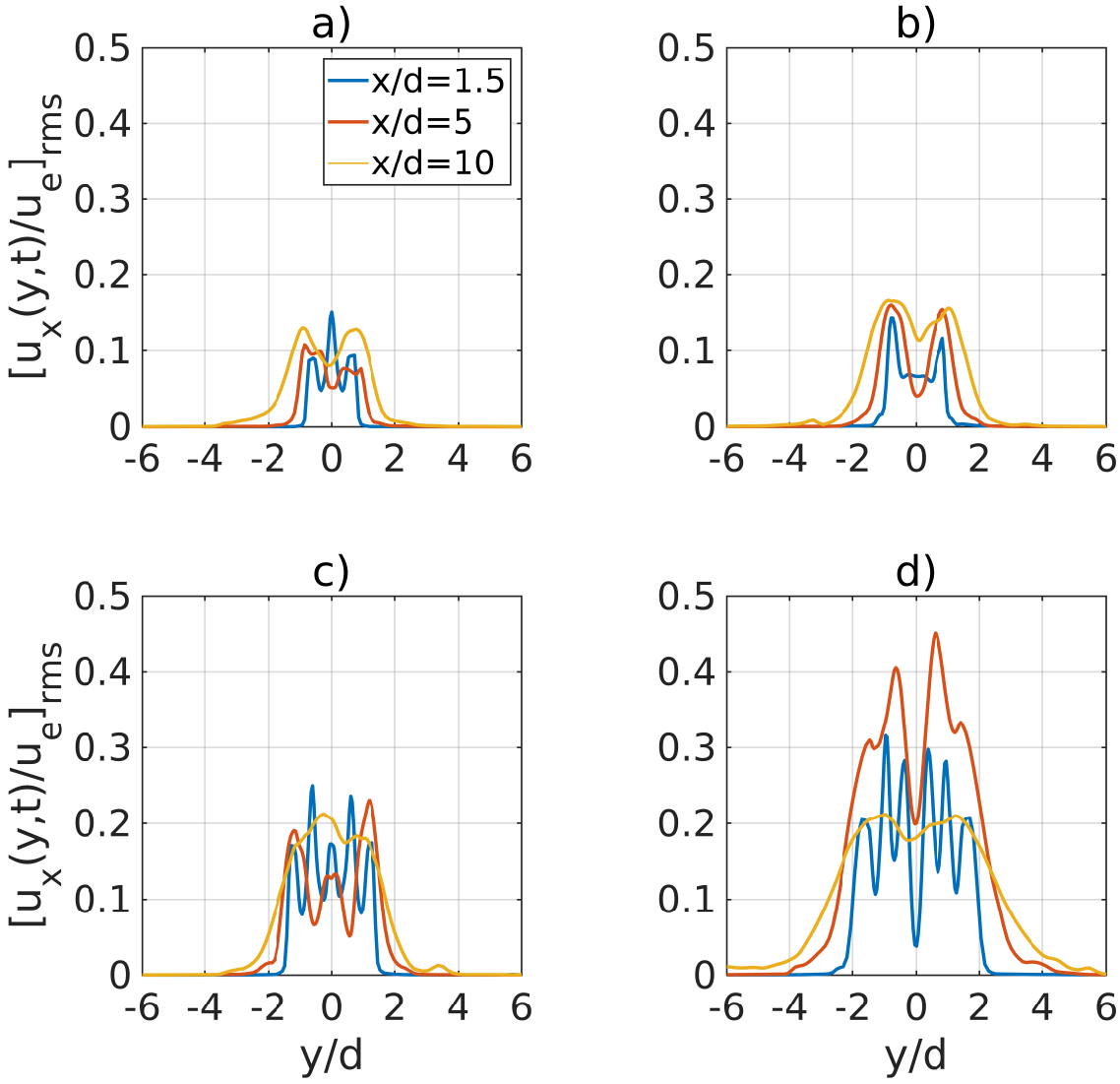

Figure 4.30: Streamwise velocity rms profiles along spanwise direction ,y/d, for different streamwise positions, measured in units of d (not d_{eq}), for cases: a) SJ b) SJ-eq, c) TJ1.15, d) TJ1.8.

For case SJ-eq, shown in Figure 4.29, the same waving pattern is found as in case SJ, but with lower amplitude for case SJ-eq, explained mainly by the lower underexpansion

level. In addition, the core length is L_p/d=11.5 due to larger momentum flux. In terms of rms profiles, case SJ-eq has higher velocity and pressure fluctuations for 0< x_c/d <1.8 while for 1.8< x_c/d <10, they are lower. This is correlated with the larger fluctuations found outside the core. Also, similar to case SJ, there is a second local maximum value in velocity fluctuations where the potential core ends.

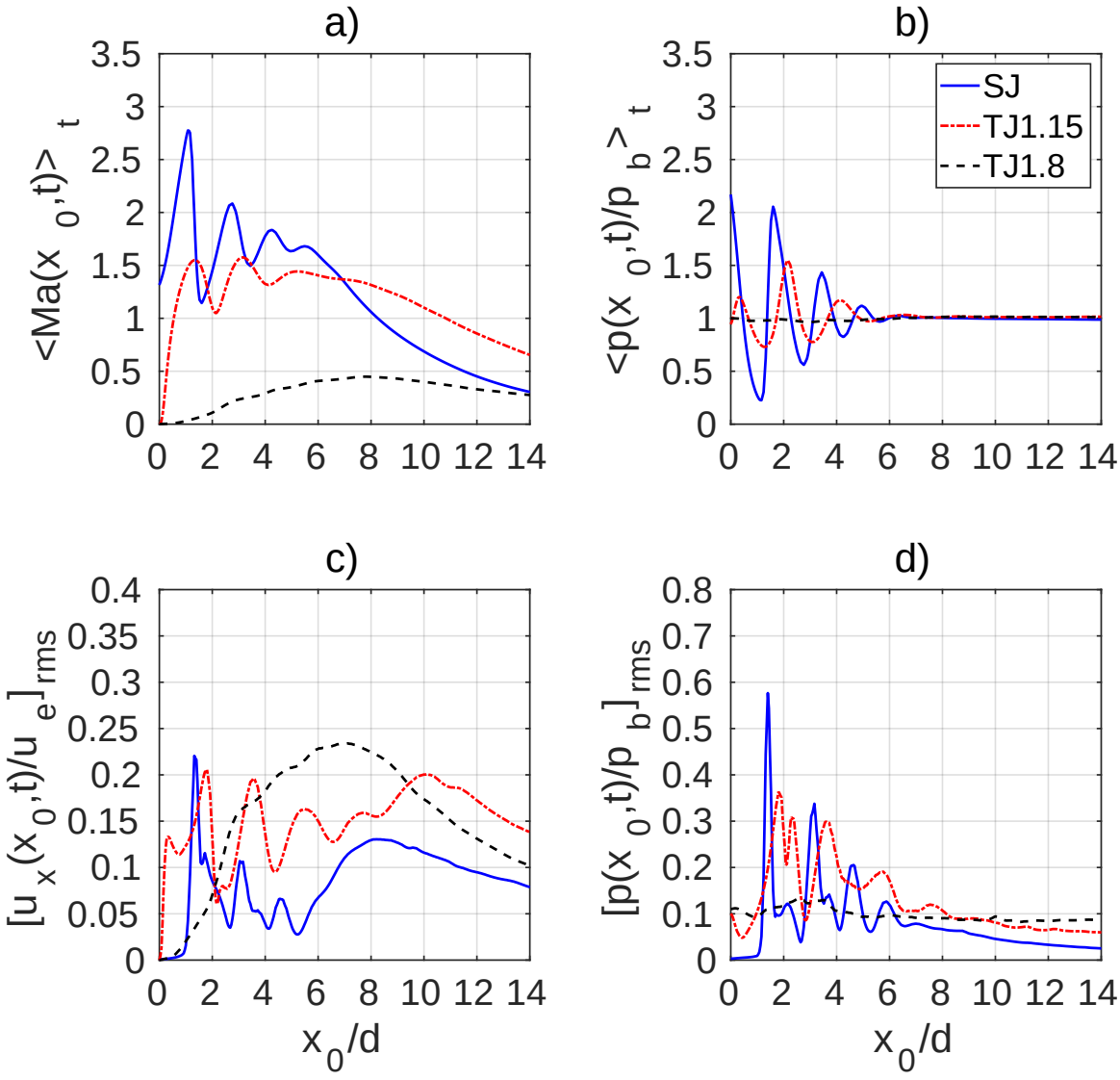

Figure 4.31: Time-averaged profiles, for cases SJ, TJ1.15 and TJ 1.8, along the tank axis coordinate, x_0, of: a) Mach and b) normalized pressure. Rms profiles along the same lines: c) Streamwise velocity, d) Pressure. In case SJ, $x_0 = x_c$.

Figure 4.30 shows, for all cases, streamwise velocity rms profiles along spanwise direction ,y/d, for different streamwise positions. In case SJ, at x/d=1.5, close to the injection point, fluctuations are the highest mainly due to the change in the position where shock-

waves reflect. At the core middle, fluctuation are larger towards the air-water interface. For the position downstream de potential core, the fluctuations are higher due to the interface deformation. Also, the width of the rms profiles are wider for increasing streamwise positions, which is related to the jet pressure based spread rate. For case SJ-eq a similar distribution is obtained, but with overall larger fluctuations. Case TJ1.15 shows a distribution where the peaks at y/d=-1 and y/d=1 are related to the point where shock reflection occurs. In positions further downstream, the fluctuations show that the small interspace yields a similar behavior to that observed in case SJ-eq. With this it can be said that in terms of velocity fluctuations, the smaller interspace twin jet configuration shows to be an equivalent of the injection with a single tuyere but higher diameter (in this case by a factor of $\sqrt{2}$). Case TJ1.8 shows the highest fluctuations in all streamwise locations, in particular in the core middle, towards the interface, fluctuations are the highest. Also, wider profiles are obtained away from the injection point at x/d=1.5;

Figures 4.31 a) and b) show time-average profiles along the tank axis, for cases SJ, TJ1.15 and TJ1.8. In case TJ1.15 supersonic velocities are obtained with a waving pattern typical of case SJ. A "potential core length" of L_p/d=10 is obtained, also found in the profile along the flow-centerline (see Figure 4.28). Therefore, in the average sense, shockwave interaction exists between each submerged jet, an effect substantiated by waving pressure profiles. In contrast, for case TJ1.8, jets separation is enough to eliminate such interaction, as subsonic velocities are found and pressure corresponds mainly to the hydrostatic profile.

The rms profiles along the tank axis are shown in Figures 4.31 c) and d). In case TJ1.15, for $0< x_0/d <1$, the highest velocity fluctuations and decrease in pressure rms are found. This is mainly attributed to the presence of a small portion of air-water interface in the tuyere interspace and local turbulence. For $x_0/d > 1$, the velocity and pressure rms profiles resemble fluctuations found in case SJ and are explained by shockwave interaction, an effect that is predominant over local turbulence and eventual air-water interface interaction (e.g. small bubble entrainment). In case TJ1.8, fluctuations are characterized by interface deformation and turbulence effects. This is made more evident by looking at the pressure rms profile, having approximately constant and lower values. Therefore, as liquid is present between the submerged jets, pressure effects are not relevant to jets interaction.

To characterize submerged jets motion, together with the information related to rms profiles and entrainment analyzed earlier, Figure 4.32 shows frequency spectra of streamwise velocity, obtained with Fast Fourier Transform at different locations near the injection point and spanwise positions in the tuyere axis and just inside the air-water interface (For TJ1.15 and TJ1.8 tuyere No.1 is used). For case SJ-eq at y/d=0, the characteristic frequencies are 12.6, 92 and 304 Hz. In case SJ at y/d=0, these change to 144 and 211 Hz; In case TJ1.15 at y/d=0.45, frequencies are slightly different, with 131 and 219 Hz; for

case TJ1.8 at y/d=0.9, several frequencies are obtained, where the relevant ones are 17.7, 48, 139 and 213 Hz. From instantaneous streamwise velocity distributions, it is observed that the highest frequencies that dominate in the spectra correspond to the "vibration" of the first shock cell. Such change in the cell size are mainly due to sharp variations of velocity at the point of measurement. Moreover, the frequencies found are related mainly to the jets waving pattern as it is the mode that predominates in all cases, particularly in the twin jet cases. However, an approximate measurement of flapping (symmetric) mode is found to be about 45Hz in case TJ1.15 and 30 Hz in case TJ1.18, where the contours distribution images for all recorded times are used. A more detailed analysis can be done by analyzing the spatial correlation between the resulting cell structure for each mode, to identify when they occur. This is left for future work.

The positions just inside the interface show for all cases a small change in frequencies, but in general show greater energy, indicating that fluctuations are stronger near the interface, which relates to the jet entrainment characteristics. In cases SJ-eq the energy is larger at the inner side of the interface as compared to the point at the tuyere axis. For case SJ the energy at the center and near the interface is similar, except for the large peak at 211Hz. In cases TJ1.15 and TJ1.8 a different energy distribution is obtained, where near the interface it is larger by about two order of magnitude, and where case TJ indicates that larger fluctuations are obtained at the point in the axis and the interface inner side.

The energy distribution just outside the air-water interface and away from it is completely different, as shown in the frequency spectra of streamwise velocity in Figure 4.33. Although the main frequencies are still observed, the energy change is more evident, where the cases TJ1.15 and TJ1.8 have larger energy related to stronger fluctuations as compared to cases SJ-eq and SJ. Thus, the twin jet configuration can induce larger fluctuations away from the jet, particularly just outside the interface. This indicates stronger entrainment characteristics of the jets, particularly for case JT1.8. Away from the jet interface the energy falls strongly, meaning that the influence of fluctuations of the interface in the surrounding water is small and produces mostly variations in pressure and velocity.

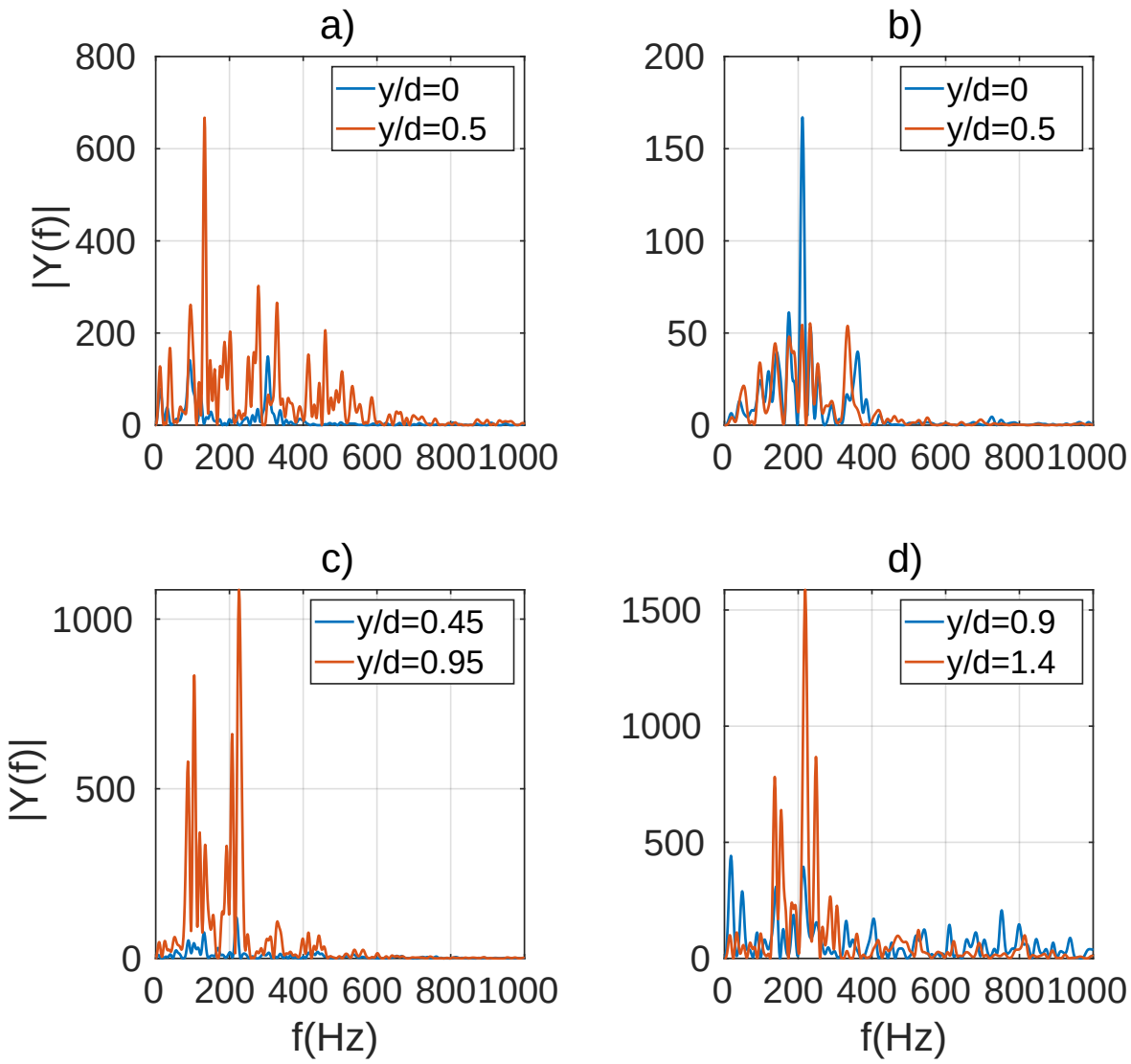

Figure 4.32: Frequency spectra (energy in arbitrary units) obtained at locations near the injection point and in different spanwise positions: a) Case SJ-eq, x/d=2, b) Case SJ, x/d=3, c) Case TJ1.15, x/d=4, d) Case TJ1.8, x/d=4. For the twin jet cases, only tuyere no.1 is considered. The lowest frequencies have no physical correlation.

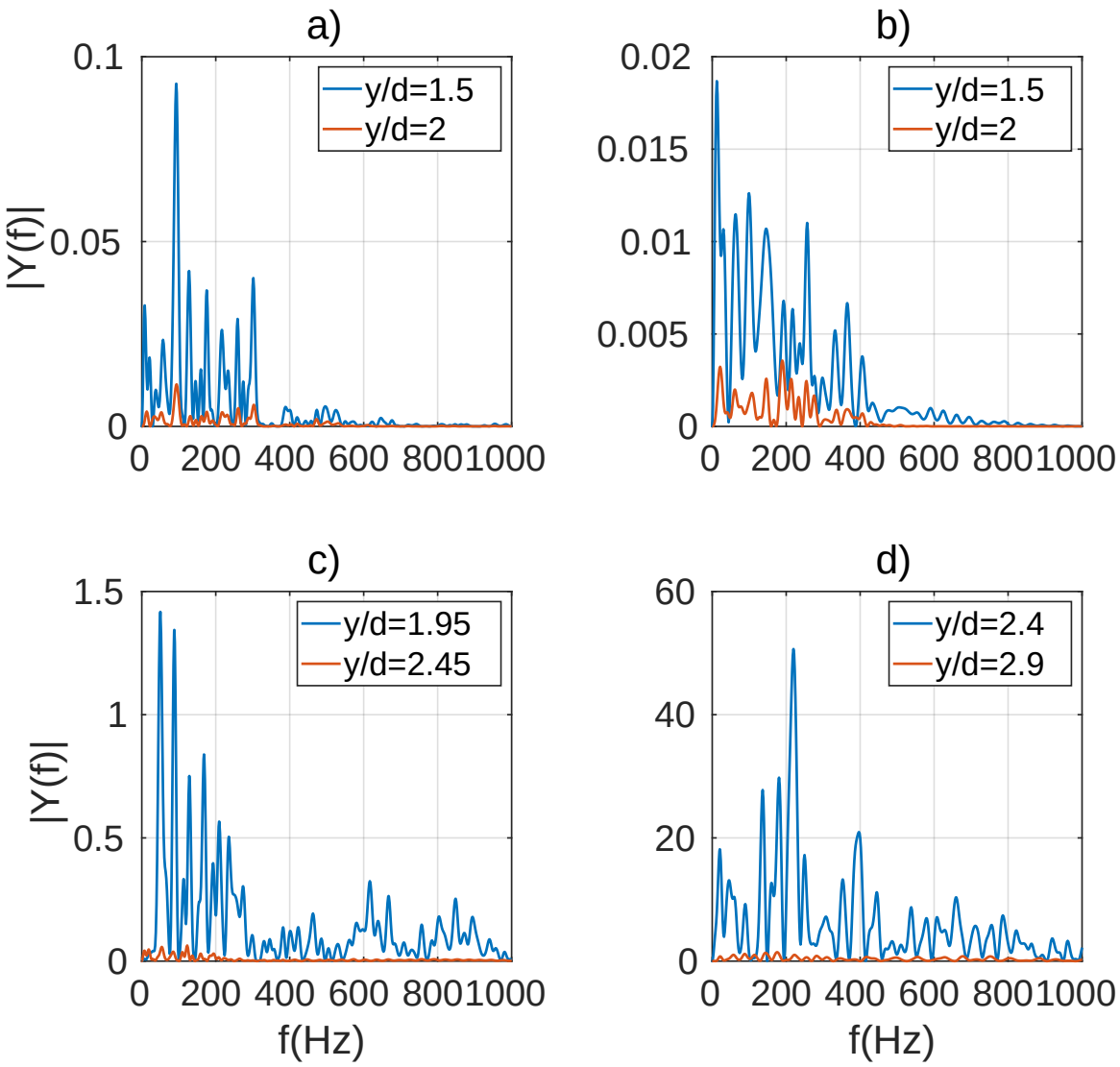

Figure 4.33: Frequency spectra (energy in arbitrary units) obtained at locations near the injection point and in different spanwise positions: a) Case SJ-eq, x/d=2, b) Case SJ, x/d=3, c) Case TJ1.15, x/d=4, d) Case TJ1.8, x/d=4. For the twin jet cases, only tuyere no.1 is considered. The lowest frequencies have no physical correlation.

4.5. General Guideline for Selection

In Table 4.2 a general guideline to select the desired type of injection is shown, keeping in mind that, for this study, there is a fixed pressure capacity (e.g. reservoir or compressor capacity) and able to provide a given mass flow rate.

It is worth noticing that the use of more than two tuyeres to inject the same mass flow is left out of the analysis, since it would be necessary to increase the NPR to keep the jet conditions at the tuyeres exit. With these restrictions, the usage of this general guideline is shown in the following example.

Given a tank (e.g. reactor) dimensions and operating liquid level, choosing a single tuyere of diameter $d_{eq} = \sqrt{2}d$, will lead to a penetration around $11.5d$, with low levels of mixing close to the injection point, but a high Back-Attack Risk (B.A.R). In addition, it can be anticipated that at such diameter, the resulting flow will induce high agitation, particularly splashing and sloshing (Valencia et al. [55]). If twin tuyeres of diameter d are to be used, then spacing between them must be selected, for example, to displace reaction effects away from the wall surrounding the tuyeres (Ito et al. [28]). In this case, the minimum spacing s/d=1.15 should be selected, ensuring a similar penetration, with low B.A.R., and with a lower impact in tank agitation, but at the cost of a higher NPR, and a slight increase in mixing and entrainment rate close to the injection points.

Table 4.2: General selection guideline for submerged injection using single and twin tuyeres. In this table SJ: single tuyere configuration, TJ-small: minimum tuyere separation for twin tuyeres, TJ-mid: medium tuyeres separation, and TJ-large: tuyere separation such that no interaction between submerged jets is observed. The potential core length, reference mixing levels and Back-Attack Risk (B.A.R) are shown, with the latter related to the frequency of "wall-knocking" events (Miaosheng et al. [34]) and used here as general reference.

Config.-spacing	Equivalent Case	s/d	L_p/d	$max(\frac{[u_x]_{rms}}{u_e})$	B.A.R
Single (equivalent)	SJ-Eq	-	11.5	18%	High
Twin-small	TJ1.15	1.15	10	25%	
Twin-mid	TJ1.8	1.8	6.5	46%	Low
Twin-large	SJ	>>1	8	14%	

Chapter 5

Conclusions

Conclusions from the present study are listed in what follows:

1. The simulation of an underexpanded and submerged jet, using a nozzle with diameter, d, with η_e=2 results in a pressure profile showing that a shockwave structure is present in the jet (as in case SJ). It is found that the profile is in good agreement with experimental data for a similar injection setup. Thus, CFD simulation of the single nozzle case is validated.

2. Given the injection pressure conditions (i.e. prescribed NPR) in the single nozzle configuration, the pressure and velocity variations inside and at the nozzle exit are almost null. The variations along the nozzle centerline in flow variables in the outer nearfield, correspond to variations in the location of shockwave reflection which in turn is related to the gas-liquid (air-water) interface deformation.

3. To inject twice the mass flow with a single nozzle, the diameter, d_{eq}, must be increased (so that $d_{eq} > d$), since it has been defined that there is a limit in the pressure capacity (as in case SJ-eq). This definition makes that the underexpansion,η_e <2 and so larger fluctuations are observed in flow variables (e.g. pressure) at the nozzle exit and in the outer nearfield, along the centerline. Furthermore, this configuration poses a condition in which back-attack is not suppressed (according to experimental results found in the literature).

4. Another way to inject twice the mass flow is to use twin nozzles of diameter d, keeping the same total cross section area (then, $d_{eq} = \sqrt{2}d$). Under this configuration, a change in behavior is observed by modifying the nozzles interspace. For closely placed nozzles (as in case T1.15), the gas jets interact by shockwave reflections and an overall waving pattern is found. A combined potential core is generated, which is about 25% larger than a single nozzle of diameter, d, injecting half the mass flow. Furthermore, the average merging point is zero, and the converging point is about $1.3d$ downstream the nozzle exit.

5. By increasing the nozzles separation to about two diameters between centers (as in case TJ1.8), individual jets have potential cores that are 18% shorter than the one

obtained with a single nozzle of diameter d. The merging point is also zero, and the converging point locates at about $7.8d$ downstream the injection point. In addition, this configuration offers the largest pressure fluctuations close to the injection points, where a pressure-driven interaction between the jets is identified.

6. In terms of mixing characteristics, computed as velocity variation outside the average potential cores, and using as base of comparison the nozzle of diameter d (case SJ), a single nozzle of diameter d_{eq} (case SJ-eq) has slightly larger mixing levels, which has a correlation in entrainment. If twin jets are closely placed to each other (case TJ1.15), levels are also increased in the same proportion. In contrast, larger nozzles spacing (case TJ1.8) generates the highest mixing levels, indicated by the largest entrainment levels. The entrainment effects (related to mixing) can be related to interaction of Kelvin Helmholtz type of instabilities of the submerged jets. However this requires a separate investigation.

7. A general selection guideline is given, in order to aid the design process of an agitated reactor tank. In particular, given a required mass flow, design can be improved by displacing reactions, while suppressing the B.A.R., but at the cost of higher pressure demand, without exceeding pressure capacity.

Bibliography

[1] P.E. Anagbo, J.K. Brimacombe, A.E. Wraith, Formation of Ellipsoidal Bubbles at a Free-Standing tuyere, Chem.Eng.Sci. 46-3 (1991) 781-788.

[2] Anderson, J.D., Modern Compressible Flow With Historical Perspective, McGraw-Hill, New York, 2021.

[3] T. Aoki, The Mechanism of the Back-attack Phenomenon on a Bottom Blowing Tuyere Investigated in Model Experiments, Tetsu-to-Hagane, 76-11 (1990) 1996-2003.

[4] N.T. Basse, Turbulence Intensity and the Friction Factor for Smooth- and Rough-Wall Pipe Flow, Fluids 2-30 (2017) 1-13.

[5] G. Bell, J. Soria, D. Honnery, D. Edgington-Mitchell, An Experimental Investigation of Coupled Underexpanded Supersonic Twin-Jets, Exp. Fluids 59-139 (2018) 1-19.

[6] P. Birkby, G.J Page, Numerical predictions of turbulent underexpanded sonic jets using a pressure-based methodology, Proc. Inst. Mech. Eng., Part G 215 (2001) 165-173.

[7] J.U. Brackbill, D.B. Kothe, C. Zemach, A Continuum Method for Modeling Surface Tension, J. Comput. Phys. 100-2 (1992) 335-354.

[8] J.K. Brimacombe, S.E. Meredith, R.G.H. Lee, High-Pressure Injection of Air into a Peirce-Smith Copper Converter, Metall. Mater. Trans. B 15 (1984) 243-250.

[9] A.A. Bustos, G.G. Richards, N.B. Gray, J.K. Brimacombe, Injection Phenomena in Nonferrous Processes, Metall. Mater. Trans. B 15 (1984) 77-89.

[10] L.B. Carasik, H. Wang, Y.A. Hassan, Simulations of Twin Turbulent Planar-Like Jets Injected Into a Large Volume Using RANS, J. Fluids Eng. 140 (2018) 1-12.

[11] J.L. Carreau, L. Loukarfi, L. Gbakoue, P. Hobbes, F. Roger, Hydrodynamics of an axisymmetric submerged non-reactive gas jet measurement of entrainment contribution to the wastage modelling, in: Proc. 19th IECEC American Nuclear Society Vol. 859176, 1985, pp. 1688-1695.

[12] I.B. Celik, U. Ghia, P.J. Roache, C.J. Freitas, H. Coleman P.E. Raad, Procedure for Estimation and Reporting of Uncertainty Due to Discretization in CFD Applications, J. Fluids Eng. 130 (2008) 1-4.

[13] T.C. Chawla, The Kelvin-Helmholtz Instability of the Gas-Liquid Interface of a Sonic Gas Jet Submerged in a Liquid, J. Fluid Mech. 67-3 (1975) 513-537.

[14] L. Davidson, E.H. Amick, Formation of Gas Bubbles at Horizontal Orifices, A.I.Ch.E. Journal 2-3 (1956) 337-342.

[15] J.F. Davidson, A.M.I. Mech, B.O.G. Schuler. Bubble Formation at an Orifice in a Viscous Liquid, Trans. I. Chem. E. 38 (1960) 105-115.

[16] S.S. Desphande, L. Anumolu, M.F. Trujillo, Evaluating the Performance of the Two-phase Flow Solver interFoam, Comput Sci Discov 5 (2012) 014016.
Evaluating the Performance of the Two-phase Flow Solver interFoam
Suraj S Deshpande, Lakshman Anumolu and Mario F Trujillo

[17] C.D. Donaldson, R.S. Snedeker, A Study of Free Jet Impingement. Part 1. Mean Properties of Free and Impinging Jets, J.Fluid Mech. 45 (1971) 281-319.

[18] B. Drew, J. Charonko, P. Vlachos, Liquid Entrainment by Round Turbulent Gas Jets Submerged in Water, in: Proceedings of ASME-JSME-KSME Joint Fluids Engineering Conference, Hamamatsu, Shizuoka, Jul 24-29, 2011, pp. 1-9.

[19] M. Epstein, H.K. Fauske, S. Kubo, T. Nakamura, K. Koyama, Liquid Entrainment by an Expanding Core Disruptive Accident Bubble — a Kelvin/Helmholtz Phenomenon, Nucl. Eng. Des. 210 (2001) 53-77.

[20] E.E. Essel, A. Laban, S. Mali, M.F. Tachie, Turbulent Characteristics of Submerged Twin Jets, in: 46th AIAA Fluid Dynamics Conference, Washington, Jun. 13-17, No. 2016-4251, 2016, pp. 1-10.

[21] J.E. Field, L. Poldevart, A.P.J. Wijnands, Photographic Study of the Interaction of Two High-Velocity Gas Jets, in: Int. Congr. on High Speed Photogr. (Photonics), 12th, Vol. 97, 1977, pp. 452.

[22] E. Franquet, P. Perrier, S. Gibout, P. Bruel, Free Underexpanded Jets in a Quiescent Medium: A Review, Prog. Aero. Sci. 77 (2015) 1-29.

[23] M. Fronzeo, M. Kinzel, An Investigation of Gas Jets Submerged in Water, in: 46th AIAA Fluid Dynamics Conference, Washington, Jun. 13-17, No. 2016-4253, 2016, pp. 1-16.

[24] Z. Gong, L. Chuan-jin, J. Li, C. Jia-yi, The Gas Jet Behavior in Submerged Laval tuyere Flow, J. Hydrodyn. 29-6 (2017) 1035-1043.

[25] S.S. Gulawani, S.S. Deshpande, J.B. Joshi, M.S. Shah, C.S.R. Prasad, D.S. Shukla, Submerged Gas Jet into a Liquid Bath: A Review, Ind. Eng. Chem. Res. 46 (2007) 3188-3218.

[26] K. Harby, S. Chiva, J.L. Munoz-Cobo, An Experimental Investigation on the Characteristics of Submerged Horizontal Gas Jets in Liquid Ambient, Exp. Therm. Fluid Sci. 53 (2014) 26-39.

[27] M.Iguchi, T. Nakatani, H. Ueda, Water Model Study of Turbulence Structure in a Bottom Blown Bath with Top Slag Using Conditional Sampling, Metall. Mater. Trans. B 28 (1998) 755-761.

[28] K. Ito, S- Kobayashi, M. Tokuda, Mixing Characteristics of a Submerged Jet Measured Using an Isokinetic Sampling Probe, Metall. Mater. Trans. B 22 (1991) 439-445.

[29] T. Knast, G. Bell, M. Wong, M.C. Leb, J. Soria, D.R. Honnery, D. Edgington-Mitchell, Coupling Modes of an Underexpanded Twin Axisymmetric Jet, AIAA Journal 56-9 (2018) 1-12.

[30] N.K. Kyriakides, E.G. Kastmnaki, S.G. Nychas, Bubbling from tuyeres Submerged in Water: Transitions Between Bubbling Regimes, Can. J. Chem. Eng. 75 (1997) 684-691.

[31] V. Lijo, H.D. Kim, T. Setoguchi, Analysis of Choked Viscous Flows Through a Constant Area Duct, in: Proc. IMechE Part G: J. Aero. Eng. Vol. 224, 2010, pp. 1151-1162.

[32] E. Loth, G.M. Faeth, Structure of Underexpanded Round Air Jets Submerged in Water, Int. J. Multiph. Flow, 15-4 (1989) 589-603.

[33] T. Miao, T., J. Liu, S. Qin, N. Chu, D. Wu, L. Wang, The Flow and Acoustic Characteristics of Underwater Gas Jets from Large Vertical Exhaust tuyeres, J. Low Freq. Noise, Vib. and Act. Cont. 37-1 (2018) 74-89.

[34] H. Miaosheng, Q. Lizi,Q., L. Yu, Oscillation Flow Induced by Underwater Supersonic Gas Jets from a Rectangular Laval tuyere, Procedia Eng. 99 (2015) 1531-1542.

[35] H. Moon, S. Han, Y. You, M. Kwon, Hybrid Rocket Underwater Propulsion: A Preliminary Assessment, Aerospace 6-3 (2019) 1-19.

[36] K. Mori, Y. Ozawa, M. Sano, Characterization of Gas Jet Behavior at a Submerged Orifice in Liquid Metal, Trans. ISIJ 22 (1982) 377-384.

[37] F. Municchia, P.P. Nagranib, I. Christova, A Two-Fluid Model for Numerical Simulation of Shear-dominated Suspension Flows, Int. J. Multiph. Flow 120 (2019) 103079.

[38] The OpenFOAM Foundation (2019). *https://openfoam.org*

[39] R.N. Oskouie, M.F. Tachie, B.C. Wang, Effect of Nozzle Spacing on Turbulent Interaction of Low-Aspect-Ratio Twin Rectangular Jets, Flow Turbul. Combust. 103 (2019) 323–344.

[40] Y. Ozawa, K. Mori, Characteristics of Jetting into Liquid Observed in Gas Injection, Trans. ISIJ 23 (1983) 764-768.

[41] Y. Ozawa, K. Mori, Effect of Physical Properties of Gas Bubbling-Jetting Phenomena in Gas and Liquid on Injection into Liquid, Trans. ISIJ 26 (1986) 291-297.

[42] K.A. Phalnikar, R. Kumar, F.S. Alvi, Experiments on Free and Impinging Supersonic

Microjets, Exp. Fluids 44-5 (2008) 819-830.

[43] Pope, S.B., Turbulent Flows, Cambridge University Press, Cambridge, 2000.

[44] G. Raman, R. Taghavi, Coupling of Twin Rectangular Supersonic Jets, J.Fluid Mech. 354 (1998) 123-145.

[45] F.P. Ricou, D.B. Spalding, Measurements of entrainment by axisymmetrical turbulent jets, J.Fluid Mech. 11-1 (1961) 21–32.

[46] F. Roger, J.L. Carreau, L. Gbahoue, P. Hobbes, A. Allou, F.Beauchamp, Structure of strongly underexpanded gas jets submerged in liquids-Application to the wastage of tubes by aggressive jets, Nucl. Eng. Des. 273 (2014), 119-130.

[47] M. Rosales Vera, A. Valencia, R. Fuentes, Ramón, A Methodology for Controlling Slopping in Copper Converters by Using Lateral and Bottom Gas Injection, Int. J. Chem React Eng. 7 (2009), 1-17.

[48] M. Rosales Vera, O. Saavedra, D. Jaques, A. Hinojosa, Exact and Asymptotic Solutions to the Trajectory of Injected Gas Jet in a Stagnant Liquid, Adv. Differ. Equ. Control Process. 16-2 (2015), 85-107.

[49] H.H. Shi, Q. Guo, C. Wang, R.L. Dong, L.T. Zhang, H.X. Jia, X.G. Wang, B.Y. Wang, Oscillation Flow Induced by Underwater Supersonic Gas Jets, Shock-Waves 20-4 (2010) 347-352.

[50] H.H. Shi, B.Y.Wang, Z.Q. Dai, Research on the Mechanics of Underwater Supersonic Gas Jets, Sci. China Phys. Mech. Astron. 53-3 (2010) 527-535.

[51] V. Suponitsky, A. Froese, S. Barsky, Richtmyer–Meshkov Instability of a Liquid–gas Interface Driven by a Cylindrical Imploding Pressure Wave, Comput. Fluids 89 (2014) 1-19.

[52] J. Tang, L. Shipeng, W. Ningfei, Y. Wei, W. Shyy, Flow Structures of Gaseous Jet Injected into Liquid for Underwater Propulsion, in: 46th AIAA/ASME/SAE/ASEE Joint Propulsion Conference & Exhibit, Nashville, Tennessee, Jul. 25-28, No. 2010-6911, 2010, pp. 1-14.

[53] I.F. Taylor, J.K. Wright, D.K. Philp, Transient Pressure and Vibration Events Resulting from High Speed Gas Injection into Liquids, Can. Met Quat 27-4 (1988) 293-301.

[54] N.J. Themelis, P. Tarassoff, J. Szekely, Gas-Liquid Momentum Transfer in a Copper Converter, Trans. Met. Soc. AIME 245 (1969) 2425-2433.

[55] A. Valencia, M. Rosales, C. Orellana, Fluid Dynamics in a Teniente Type Copper Converter Model with One and Two Tuyeres, AIME Article ID 902874 (2013) 1-8.

[56] V. Vuorinen, J. Yu, S. Tirunagari, O. Kaario, M. Larmi, C. Duwig, B.J. Boersma, Large-Eddy Simulation of Highly Underexpanded Transient Gas Jets, Phys. Fluids 25-016101 (2013) 1-22.

[57] C. Weiland, P.P. Vlachos, Round Gas Jets Submerged in Water, Int J. Mult. Flow 48 (2013) 46-57.

[58] D., Wilcox, Formulation of the k-ω Turbulence Model Revisited, in: 45th AIAA Aerospace Sciences Meeting and Exhibit, Reno, Nevada, Jan. 8-11, No. 2007-1408, 2007, pp. 1-14.

[59] X. ZHang, S. Li, D. Yu, B. Yang, N. Wang, The Evolution of Interfaces for Underwater Supersonic Gas Jets, Water 12-488 (2020), p. 1-18.